

INFORMATION TO USERS

This reproduction was made from a copy of a document sent to us for microfilming. While the most advanced technology has been used to photograph and reproduce this document, the quality of the reproduction is heavily dependent upon the quality of the material submitted.

The following explanation of techniques is provided to help clarify markings or notations which may appear on this reproduction.

1. The sign or "target" for pages apparently lacking from the document photographed is "Missing Page(s)". If it was possible to obtain the missing page(s) or section, they are spliced into the film along with adjacent pages. This may have necessitated cutting through an image and duplicating adjacent pages to assure complete continuity.
2. When an image on the film is obliterated with a round black mark, it is an indication of either blurred copy because of movement during exposure, duplicate copy, or copyrighted materials that should not have been filmed. For blurred pages, a good image of the page can be found in the adjacent frame. If copyrighted materials were deleted, a target note will appear listing the pages in the adjacent frame.
3. When a map, drawing or chart, etc., is part of the material being photographed, a definite method of "sectioning" the material has been followed. It is customary to begin filming at the upper left hand corner of a large sheet and to continue from left to right in equal sections with small overlaps. If necessary, sectioning is continued again—beginning below the first row and continuing on until complete.
4. For illustrations that cannot be satisfactorily reproduced by xerographic means, photographic prints can be purchased at additional cost and inserted into your xerographic copy. These prints are available upon request from the Dissertations Customer Services Department.
5. Some pages in any document may have indistinct print. In all cases the best available copy has been filmed.

**University
Microfilms
International**

300 N. Zeeb Road
Ann Arbor, MI 48106

Order Number 1333603

**Electromagnetic coupling by a wire penetrating a circular
aperture in an infinite planar conducting screen**

Lee, Robert, M.S.

The University of Arizona, 1988

U·M·I

**300 N. Zeeb Rd.
Ann Arbor, MI 48106**

PLEASE NOTE:

In all cases this material has been filmed in the best possible way from the available copy.
Problems encountered with this document have been identified here with a check mark ☒.

1. Glossy photographs or pages _____
2. Colored illustrations, paper or print _____
3. Photographs with dark background _____
4. Illustrations are poor copy _____
5. Pages with black marks, not original copy ☒
6. Print shows through as there is text on both sides of page _____
7. Indistinct, broken or small print on several pages ☒
8. Print exceeds margin requirements _____
9. Tightly bound copy with print lost in spine _____
10. Computer printout pages with indistinct print _____
11. Page(s) _____ lacking when material received, and not available from school or author.
12. Page(s) _____ seem to be missing in numbering only as text follows.
13. Two pages numbered _____. Text follows.
14. Curling and wrinkled pages _____
15. Dissertation contains pages with print at a slant, filmed as received ☒
16. Other _____

U·M·I

**ELECTROMAGNETIC COUPLING
BY A WIRE
PENETRATING A CIRCULAR APERTURE
IN AN INFINITE PLANAR CONDUCTING SCREEN**

by
Robert Lee

**A Thesis Submitted to the Faculty of the
DEPARTMENT OF ELECTRICAL AND COMPUTER ENGINEERING
In Partial Fulfillment of the Requirements
For the Degree of
MASTER OF SCIENCE
WITH A MAJOR IN ELECTRICAL ENGINEERING
In the Graduate College
THE UNIVERSITY OF ARIZONA**

1 9 8 8

STATEMENT BY AUTHOR

This thesis has been submitted in partial fulfillment of requirements for an advanced degree at The University of Arizona and is deposited in the University Library to be made available to borrowers under rules of the Library.

Brief quotations from this dissertation are allowable without special permission, provided that accurate acknowledgment of source is made. Requests for permission for extended quotation from or reproduction of this manuscript in whole or in part may be granted by the head of the major department or the Dean of the Graduate College when in his or her judgement the proposed use of the material is in the interests of scholarship. In all other instances, however, permission must be obtained from the author.

SIGNED: _____

Robert Lee

APPROVAL BY THESIS DIRECTOR

This thesis has been approved on the date shown below:

3/2/88

D.G. Dudley

Professor of Electrical Engineering

ACKNOWLEDGMENTS

I would like to foremost thank Professor Donald G. Dudley for his unfailing guidance and support. His clear thinking has many times kept me from going astray. Furthermore, I want to thank Professor James R. Wait for his help in working through several technical difficulties and both him and Professor Andreas Cangellaris for reviewing the thesis and providing many useful suggestions. Their comments were greatly appreciated. Special thanks goes to Dr. Kendall Casey who began the work which eventually developed into my thesis. I would also like to thank him for providing several insightful ideas while reviewing this thesis. I would like to acknowledge the following people for their help in finishing my research: Jack Anderson, Brian Baertlein, Tom Bartone, Dr. Tom Gruszka, Wendy Valentine, Dr. Jeff Williams, Diana Wright, and Jeff Young.

This research was made possible because of the financial support provided by Sandia National Laboratory. I would especially like to thank Dr. Jeff Quintenz for his part in helping me to obtain this support and for his comments on my thesis. Finally, I wish to thank my parents for their love and encouragement during my pursuit of a graduate degree.

TABLE OF CONTENTS

	Page
LIST OF ILLUSTRATIONS	5
ABSTRACT	8
1 INTRODUCTION	9
2 FORMULATION OF THE INTEGRAL EQUATION	13
2.1 Field Equations	13
2.2 Green's Function Solutions	18
2.3 Source Analysis	22
2.4 Integral Equation	31
3 EQUIVALENT CIRCUIT MODEL	37
3.1 Formulation of Circuit Parameter Expressions	37
3.2 Zeroth Order(ZO) Approximation	41
3.3 Method of Moments(MOM) Approximation	47
3.4 Numerical Results	52
3.5 Transient Analysis	76
3.5.1 Transient Pulse	76
3.5.2 Transient Current Response	81
4 ELECTRIC FIELD	91
4.1 Formulation of Electric Field Equations	91
4.2 Far-Field Approximation	94
4.3 Results and Analysis	99
5 CONCLUSIONS AND RECOMMENDATIONS	109
APPENDIX A	113
APPENDIX B	117
REFERENCES	121

LIST OF ILLUSTRATIONS

Figure	Page
1-1 Side view of a wire with radius a passing through an aperture of radius b	11
2-1 Geometries which describe the Green's functions, g_1 and g_2	17
2-2 Coaxial line joined to a half-space with the inner conductor extending into the half-space.	23
2-3 Normalized E_ρ due to an approximate source with $z = 100$ m and $b/a = 2$	28
2-4 Normalized E_ρ due to an approximate source with $z = 10$ m and $b/a = 2$	29
2-5 Normalized E_ρ due to an approximate source with $z = 100$ m and $b/a = 25$	30
2-6 Normalized E_z due to an approximate source with $z/a = 100$ m and $b/a = 2$	32
2-7 Normalized E_z due to an approximate source with $z = 10$ m and $b/a = 2$	33
2-8 Normalized E_z due to an approximate source with $z = 100$ m and $b/a = 25$	34
3-1 Equivalent circuit model for the wire penetrating the aperture.	40
3-2 Equivalent circuit model referenced to the aperture plane.	42
3-3 Diagram comparing the quasi-static solution for the magnitude of the normalized aperture electric field to the MOM solution with $N = 10$ and $\chi = 1$	54
3-4 Diagram comparing the quasi-static solution for the magnitude of the normalized aperture electric field to the MOM solution with $N = 20$ and $\chi = 1$	55
3-5 Diagram comparing the quasi-static solution for the magnitude of the normalized aperture electric field to the MOM solution with $N = 40$ and $\chi = 1$	56

LIST OF ILLUSTRATIONS – continued

Figure	Page
3-6 Diagram comparing the quasi-static solution for the magnitude of the normalized aperture electric field to the MOM solution with $N = 8$ and $\chi = 0.6$	57
3-7 Diagram comparing the ZO solution to the MOM solution for the normalized conductance as a function of ka	59
3-8 Diagram comparing the ZO solution to the MOM solution for the normalized susceptance as a function of ka	60
3-9 Diagram comparing the ZO solution to the MOM solution for the magnitude of the normalized current at $z/a = 0$	61
3-10 Diagram comparing the ZO solution to the MOM solution for the magnitude of the normalized current at $z/a = 1$	62
3-11 Diagram comparing the ZO solution to the MOM solution for the magnitude of the normalized current at $z/a = 100$	63
3-12 The MOM solution of the normalized conductance for five aperture sizes.	65
3-13 The MOM solution of the normalized susceptance for five aperture sizes.	66
3-14 The MOM solution of the magnitude of the normalized current at $z/a = 1$ as a function of ka for five aperture sizes.	69
3-15 The MOM solution of the magnitude of the normalized current at $z/a = 5$ as a function of ka for five aperture sizes.	70
3-16 the MOM solution of the magnitude of the normalized current at $z/a = 100$ as a function of ka for five aperture sizes.	71
3-17 The MOM solution of the magnitude of the normalized current as a function of z/a for $b/a = 1.05$ at four values of ka	73
3-18 The MOM solution of the magnitude of the normalized current as a function of z/a for $b/a = 2$ at four values of ka	74
3-19 The MOM solution of the magnitude of the normalized current as a function of z/a for $b/a = 5$ at four values of ka	75
3-20 Plot of the low frequency, double exponential pulse ($\alpha = 1 \times 10^7$, $\beta = 1 \times 10^8$) in both the time and frequency domain.	78
3-21 Plot of the high frequency, double exponential pulse ($\alpha = 2 \times 10^9$, $\beta = 3 \times 10^9$) plotted in both the time and frequency domain.	79

LIST OF ILLUSTRATIONS - continued

Figure	Page
3-22 Plot of the time domain solution for the low and high frequency pulse with their frequency spectrums truncated at 255 MHz and 8 GHz, respectively.	80
3-23 Time domain results due to the low frequency pulse with $b/a = 1.01$	82
3-24 Time domain results due to the low frequency pulse with $b/a = 2$	83
3-25 Time domain results due to the low frequency pulse with $b/a = 5$	84
3-26 Time domain results due to the high frequency pulse with $b/a = 1.01$	86
3-27 Time domain results due to the high frequency pulse with $b/a = 2$	87
3-28 Time domain results due to the high frequency pulse with $b/a = 5$	88
4-1 Complex integration path in the θ plane for the far field approximation.	96
4-2 Redefined coordinate system used in the far field approximation ($\rho, z \rightarrow R, \psi$).	97
4-3 Contour plot of $ E_\rho/I_0 $ near the aperture with $b/a = 2$, $f = 10$ and 100 MHz.	100
4-4 Contour plot of $ E_z/I_0 $ near the aperture with $b/a = 2$, $f = 10$ and 100 MHz.	101
4-5 Diagram of the geometry localized to the screen edge where the coordinate system is redefined from $\rho, z \rightarrow r, \tau$	102
4-6 Contour plot of $ E_\rho/I_0 $ far from the aperture with $b/a = 2$, $f = 10$ MHz.	105
4-7 Contour plot of $ E_\rho/I_0 $ far from the aperture with $b/a = 2$, $f = 100$ MHz.	106
4-8 Contour plot of $ E_z/I_0 $ far from the aperture with $b/a = 2$, $f = 10$ MHz.	107
4-9 Contour plot of $ E_z/I_0 $ far from the aperture with $b/a = 2$, $f = 100$ MHz.	108
A-1 Contour used in the evaluation of the spectral expansion which is needed to solve the Green's functions.	114

ABSTRACT

We consider the problem of electromagnetic propagation along a wire which passes through an aperture. We begin by formulating an integral equation in terms of the electric field at the aperture. The solution of the integral equation allows us to determine parameters of interest such as the equivalent admittance, the current on the wire, and the electric field. We solve the integral equation using both a zeroth order and method of moments approximation for the aperture field. From this we are able to compute the admittance and current in the frequency domain. We next calculate the current response to a transient pulse excitation. The results show that the screen provides little shielding from pulse penetration along the wire. Finally, we calculate solutions for the electric field. The results are given in several contour plots.

CHAPTER 1

INTRODUCTION

An important consideration in electromagnetic shielding problems is establishing the degree of exterior to interior coupling that occurs at shield imperfections. One type of imperfection that sometimes occurs is a hole in the shield. There have been numerous studies done on the coupling of electromagnetic energy through an aperture or multiple apertures. The problem was first considered by Rayleigh (1897). He simplified the problem by assuming static fields and then solving it by using potential theory. Bethe (1944) formulated the problem by means of a quasi-static approach. His method was further extended by Chen (1970) and Taylor (1973) to include such things as a cavity-backed aperture. Rahmat-Samii and Mittra (1977) considered the problem of electromagnetic coupling through an infinite conducting screen. They obtained a solution by use of an integral equation. They then joined with Butler (1978) to extend this work to provide a comprehensive study of the aperture coupling problem. The results showed that in many cases the coupling is very weak.

In many practical situations, however, the aperture itself does not properly model the physical geometry. In order for a system or subsystem to communicate with other systems or subsystems, it is necessary to pass information through such things as pipes and cables. These connections must enter the system through an aperture. Such situations tend to be very complex and not easily modelled. It is possible to treat a simpler model where we retain many of the characteristics of the

more complex problem. Such models can give insight into the behavior of the fields for the more complicated case. Unlike the unobstructed aperture problem, there has been surprisingly little work done on the case where there is a line penetration through the aperture. Some initial work has been done by Casey (1987) for low frequencies. The line penetration drastically changes the behavior of the fields around the aperture. The primary effect is to substantially increase the energy coupled into the partially shielded system.

The simplified model that we consider is the problem of a wire penetrating an aperture in an infinite planar screen (Figure 1-1). The wire is infinitely long and centered in the aperture; the screen extends to infinity in the radial direction. Both the wire and the screen are assumed to be perfectly conducting. We specify the radius of the wire to be a and the radius of the aperture to be b . We choose a cylindrical coordinate system centered such that $(\rho, z) = (0, 0)$ corresponds to the center of the wire in the plane of the aperture. This choice divides the problem into two regions. Region 1 consists of the half-space $z < 0$; Region 2 consists of the half-space $z > 0$. We have assumed free space ($\mu = \mu_0, \epsilon = \epsilon_0$) in both regions. The resulting geometry is ϕ -symmetric. To further simplify the problem we assume that the source is also ϕ -symmetric. The result is a two dimensional problem with variations of the fields in ρ and z . Because we are mainly interested in the TM modes with respect to z , we specify the source to be a ϕ directed magnetic current source which we call M_ϕ . This allows us to decouple the equations and consider the TM modes separately. We specify the source to be in Region 1 at a distance d from the aperture.

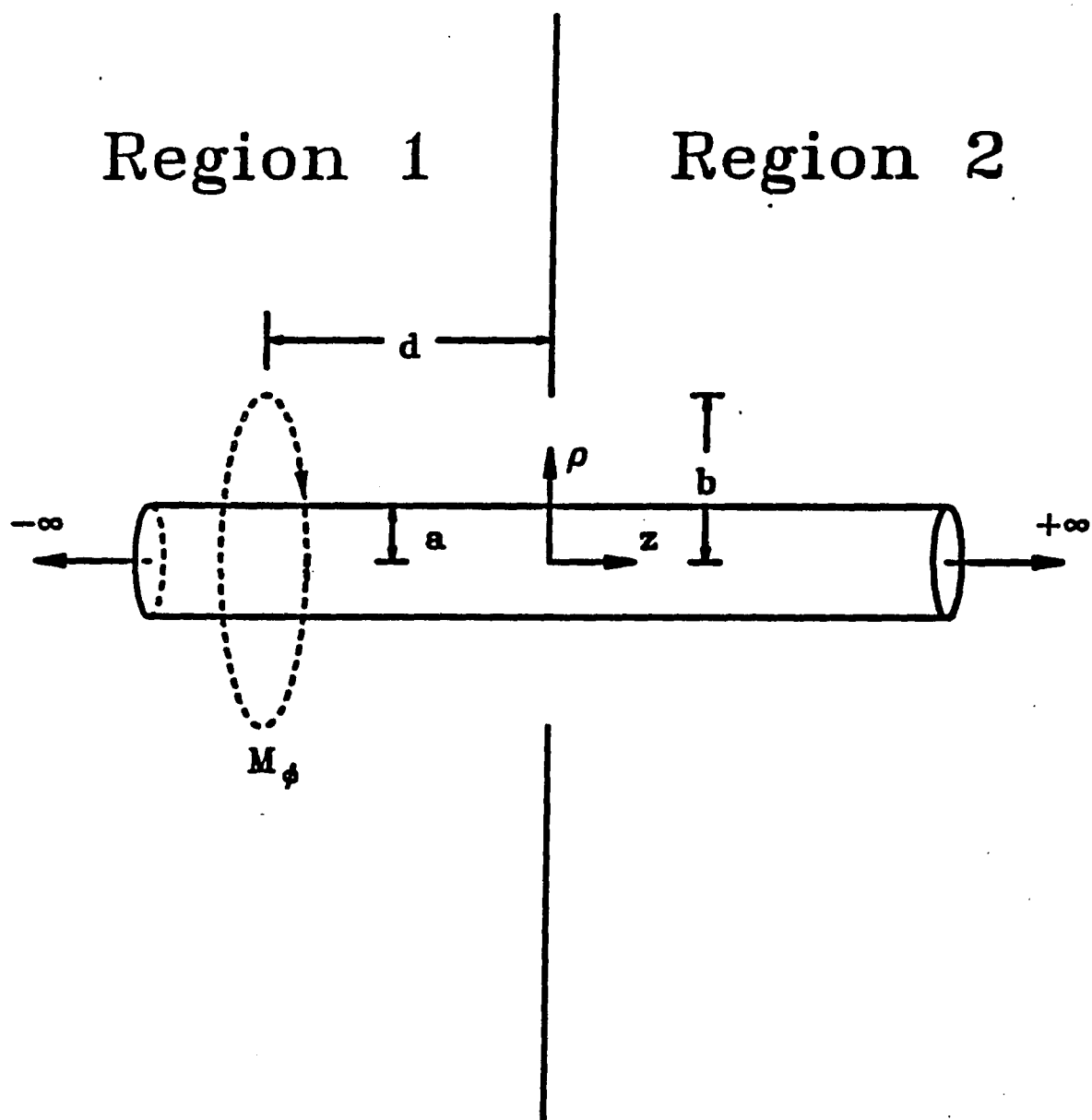


Figure 1-1 Side view of a wire with radius a passing through an aperture of radius b .

Here, we will cover both the frequency and time domain analyses. In chapter 2, we formulate the expressions for the fields. The solutions for these field expressions are dependent upon the solution of an integral equation which we derive with the help of two Green's functions and several known boundary conditions. We also discuss the behavior of the source in our problem. In chapter 3, we consider the integral equation. Because of the complexity of our problem, an exact analytical solution which is valid over all frequencies is not possible. We therefore solve the integral equation using approximate numerical methods. Both a zeroth order approximation and a method of moments approximation for the electric aperture field are considered, and the advantages and disadvantages of each approximation are discussed. Next, we formulate equations for the admittance and the current and obtain solutions using both approximations. We then proceed with a time domain analysis of our problem, where the input is a double exponential transient pulse. In chapter 4 we compute solutions for the fields in Region 2 and present several contour plots of the electric field. Solutions are first obtained from the general expressions for the fields. We then make a far field approximation on the field expressions to get a closed form solution. The results are compared to the general case to determine the accuracy of the far field approximation. Finally, we present conclusions and recommendations for future work in chapter 5.

CHAPTER 2

FORMULATION OF THE INTEGRAL EQUATION

In this chapter, we obtain an expression for the integral equation across the aperture. We begin by considering the *TM* mode field equations along with the boundary conditions. By using Green's theorem, we solve for the magnetic field H_ϕ in terms of the electric field at the aperture and the appropriate Green's functions for both Region 1 and Region 2. Two forms of the solution for the Green's functions are presented and compared. From these, we decide on which form to use in the integral equation. We then choose a source for our problem and determine a physical representation for it. By enforcing the continuity of the tangential fields in the aperture, we obtain an integral equation for the aperture field. Finally, we analyze the Green's function to determine its singularities and their possible effect on the integral equation.

2.1 Field Equations

Because we have specified azimuthal symmetry in both the geometry and the source, the electromagnetic field equations do not depend on ϕ ($\partial/\partial\phi = 0$). Therefore the field equations decouple and simplify. A description of the source will not be presented here, but rather will be discussed in section 2.3. Let us consider the time dependent Maxwell's equations without the electric current source,

$$\nabla \times \vec{E} = -i\omega\mu\vec{H} - \vec{M} \quad (2-1)$$

$$\nabla \times \vec{H} = i\omega\epsilon\vec{E} \quad (2-2)$$

where the $e^{i\omega t}$ time variation is suppressed. Separating (2-1) and (2-2) into its field components, we obtain the TM_z mode field equations:

$$E_\rho = \frac{-1}{i\omega\epsilon_0} \frac{\partial H_\phi(\rho, z)}{\partial z} \quad (2-3)$$

$$E_z = \frac{1}{i\omega\epsilon_0} \frac{\partial(\rho H_\phi(\rho, z))}{\partial \rho} \quad (2-4)$$

$$\frac{\partial E_z(\rho, z)}{\partial \rho} - \frac{\partial E_\rho(\rho, z)}{\partial z} = M_\phi + i\omega\mu_0 H_\phi \quad (2-5)$$

Since we previously specified the source to be ϕ -symmetric, it does not excite the TE_z modes, and therefore, E_ϕ , H_ρ , and H_z are zero. By substituting (2-3) and (2-4) into (2-5), we can obtain a second order partial differential equation for H_ϕ ,

$$(\nabla_{\rho z}^2 + k^2 - \frac{1}{\rho^2})H_\phi(\rho, z) = i\omega\epsilon_0 M_\phi \quad (2-6)$$

where the Laplacian $\nabla_{\rho z}^2$ is given by

$$\nabla_{\rho z}^2 = \frac{1}{\rho} \frac{\partial}{\partial \rho} \rho \frac{\partial}{\partial \rho} + \frac{\partial^2}{\partial z^2}$$

and $k = \omega\sqrt{\mu_0\epsilon_0}$ is the wave number. The source M_ϕ is assumed to be finite in extent. The field components E_ρ and E_z are then easily obtained from (2-3) and (2-4).

To solve for H_ϕ , we need to prescribe the behavior of the fields at the boundaries of the two regions. Let us assume an infinitesimally small amount of loss in both regions so that we can specify the following boundary conditions on H_ϕ :

$$\lim_{\rho \rightarrow \infty} H_\phi(\rho, z) = 0 \quad (2-7)$$

$$\lim_{|z| \rightarrow \infty} H_\phi(\rho, z) = 0 \quad (2-8)$$

Also, the tangential electric fields must vanish on the surface of the wire and the screen, i.e.

$$\lim_{\rho \rightarrow a} E_z(\rho, z) = \lim_{\rho \rightarrow a} \frac{\partial(\rho H_\phi(\rho, z))}{\partial \rho} = 0 \quad (2-9)$$

$$\lim_{|z| \rightarrow 0} E_\rho(\rho, z) = \lim_{|z| \rightarrow 0} \frac{\partial H_\phi(\rho, z)}{\partial z} = 0 \quad (\rho > b) \quad (2-10)$$

The next step is the conversion of (2-6) into an integral form. This can be accomplished by applying Green's theorem to both regions. Green's theorem requires that the volume under consideration be bounded. Unfortunately, both Region 1 and Region 2 are unbounded. We therefore use the radiation condition in the methods shown by Stratton (1941) to allow Green's theorem to handle volumes of infinite extent. Because there are no field variations in ϕ , we are able to use a degenerate form of Green's theorem:

$$\langle g, (\nabla_{\rho x}^2 + k^2 - \frac{1}{\rho^2}) H_\phi \rangle - \langle H_\phi, (\nabla_{\rho x}^2 + k^2 - \frac{1}{\rho^2}) g \rangle = \int (g \frac{\partial H_\phi}{\partial n} - H_\phi \frac{\partial g}{\partial n}) d\ell \quad (2-11)$$

where $d\ell$ is the variable of integration over the degenerate surfaces which enclose the volume and n is the outgoing normal from those surfaces. The inner product $\langle x, y \rangle$ is defined by

$$\langle x, y \rangle = \int_{V_i} xy \rho d\rho dz \quad (2-12)$$

where V_i denotes the volume of the region under consideration. It should be noted that for n in the direction of ρ ,

$$\frac{\partial H_\phi}{\partial n} = \frac{1}{\rho} \frac{\partial(\rho H_\phi)}{\partial \rho} \quad (2-13)$$

The variable g represents the Green's function which we choose to simplify (2-11).

The best choice for our case is described by the following:

$$-(\nabla_{\rho z}^2 + k^2 - \frac{1}{\rho^2})g_j = \frac{\delta(\rho - \rho')\delta(z - z')}{\rho} \quad (2-14)$$

$$\lim_{\rho \rightarrow a} \frac{\partial(\rho g_j(\rho, z))}{\partial \rho} = 0, \quad \lim_{\rho \rightarrow \infty} g_j(\rho, z) = 0,$$

$$\lim_{z \rightarrow -\infty} g_1(\rho, z) = 0, \quad \lim_{z \rightarrow \infty} g_2(\rho, z) = 0,$$

$$\lim_{|z| \rightarrow 0} \frac{\partial g_j(\rho, z)}{\partial z} = 0$$

where $j = 1$ or 2 depending upon the region of interest and $\delta(\bullet)$ is the Dirac delta function. Physically, the Green's function problem can be described by an infinitely long wire joined to an infinite planar screen. The corresponding geometries for g_1 and g_2 are shown in Figure 2-1.

Substituting (2-6) and (2-14) into (2-11) and applying the boundary conditions for our geometry, we obtain

$$\begin{aligned} H_{\phi 1}(\rho, z) = & -i\omega\epsilon_0 \int_{-\infty}^0 \int_a^\infty g_1(\rho, z | \rho', z') M_\phi(\rho', z') \rho' d\rho' dz' \\ & - i\omega\epsilon_0 \int_a^b g_1(\rho, z | \rho', 0) E_{\rho 1}(\rho', 0) \rho' d\rho' \end{aligned} \quad (2-15)$$

$$H_{\phi 2}(\rho, z) = i\omega\epsilon_0 \int_a^b g_2(\rho, z | \rho', 0) E_{\rho 2}(\rho', 0) \rho' d\rho' \quad (2-16)$$

where the subscripts on the fields indicate the region of interest. Note that in going from (2-11) to (2-15) and (2-16), we have switched the prime and unprimed variables. To complete the formulation of (2-15) and (2-16) we must obtain expressions for the Green's functions in both regions and also provide a mathematical description for the source M_ϕ .

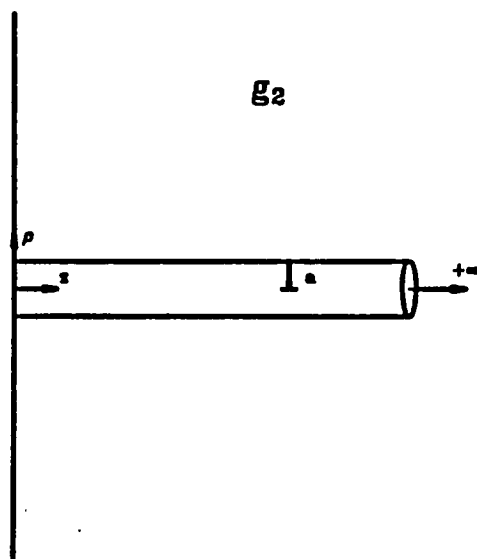
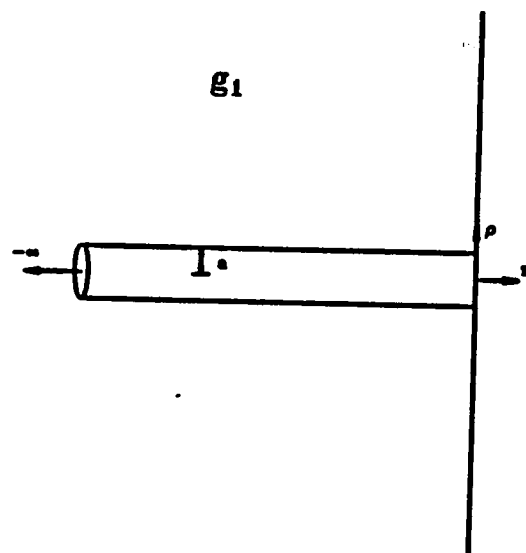


Figure 2-1 Geometries which describe the Green's functions, g_1 and g_2 .

2.2 Green's Function Solutions

In order to solve (2-14), let us first consider a simple ordinary differential equation which we write as

$$-\left(\frac{1}{\rho} \frac{d}{d\rho} \rho \frac{d}{d\rho} - \frac{1}{\rho^2} + \lambda\right)g = \frac{\delta(\rho - \rho')}{\rho} \quad (2-17)$$

$$\lim_{\rho \rightarrow \infty} g(\rho, \rho') = 0$$

$$\lim_{\rho \rightarrow a} \frac{1}{\rho} \frac{\partial(\rho g(\rho, \rho'))}{\partial \rho} = 0$$

A general solution to the differential equation in (2-17) is given by

$$g(\rho, \rho') = \begin{cases} AJ_1(\sqrt{\lambda}\rho) + BH_1^{(2)}(\sqrt{\lambda}\rho) & \rho < \rho' \\ CJ_1(\sqrt{\lambda}\rho) + DH_1^{(2)}(\sqrt{\lambda}\rho) & \rho > \rho' \end{cases} \quad (2-18)$$

where A, B, C, and D are constants to be determined and the symbols J_1 and H_1 represent the Bessel and Hankel functions, respectively. We can eliminate two of the constants by applying the given boundary conditions and by specifying the imaginary part of $\sqrt{\lambda}$ to be negative so that $H_1^{(2)}(\sqrt{\lambda}\rho) \rightarrow 0$ as $\rho \rightarrow \infty$. The resulting equation is

$$g(\rho, \rho') = \begin{cases} A'[J_1(\sqrt{\lambda}\rho)H_0^{(2)}(\sqrt{\lambda}a) - J_0(\sqrt{\lambda}a)H_1^{(2)}(\sqrt{\lambda}\rho)] & \rho < \rho' \\ DH_1^{(2)}(\sqrt{\lambda}\rho) & \rho > \rho' \end{cases} \quad (2-19)$$

We now enforce the boundary conditions for the continuity of g and the jump discontinuity of $\partial g / \partial \rho$ at $\rho = \rho'$. This gives

$$g(\rho, \rho') = \begin{cases} -\frac{\pi i}{2} \frac{H_1^{(2)}(\sqrt{\lambda}\rho')}{H_0^{(2)}(\sqrt{\lambda}a)} [J_1(\sqrt{\lambda}\rho)H_0^{(2)}(\sqrt{\lambda}a) - J_0(\sqrt{\lambda}a)H_1^{(2)}(\sqrt{\lambda}\rho)] & \rho < \rho' \\ -\frac{\pi i}{2} \frac{H_1^{(2)}(\sqrt{\lambda}\rho)}{H_0^{(2)}(\sqrt{\lambda}a)} [J_1(\sqrt{\lambda}\rho')H_0^{(2)}(\sqrt{\lambda}a) - J_0(\sqrt{\lambda}a)H_1^{(2)}(\sqrt{\lambda}\rho')] & \rho > \rho' \end{cases} \quad (2-20)$$

We next integrate the Green's function in (2-20) over the circle at infinity in the complex λ -plane to obtain a spectral expansion in ρ . The details are presented in Appendix A. The resulting expression for the spectral expansion is given by

$$\frac{\delta(\rho - \rho')}{\rho} = \int_0^\infty \frac{B(\xi\rho)B(\xi\rho')}{H_0^{(1)}(\xi a)H_0^{(2)}(\xi a)} \xi d\xi \quad (2-21)$$

where $B(\xi\rho)$ is defined by

$$B(\xi\rho) = J_1(\xi\rho)Y_0(\xi a) - J_0(\xi a)Y_1(\xi\rho)$$

The spectral expansion in (2-21) allows us to formulate a special transform pair which is very similar to the Weber transform (Stakgold, 1979). From Appendix A we get the following modified transform pair:

$$g(\rho) = \int_0^\infty \frac{G(\xi)B(\xi\rho)}{H_0^{(1)}(\xi a)H_0^{(2)}(\xi a)} \xi d\xi \quad (2-22)$$

and

$$G(\xi) = \int_a^\infty g(\rho')B(\xi\rho')\rho' d\rho' \quad (2-23)$$

Consider g_1 in (2-14). We perform the modified Weber transform to give

$$-\left(\frac{\partial^2}{\partial z^2} + k^2 - \xi^2\right) G_1 = \delta(z - z')B(\xi\rho') \quad (2-24)$$

where G_1 is the transform of g_1 and where we have used the fact that

$$-\left(\frac{1}{\rho}\frac{\partial}{\partial\rho}\rho\frac{\partial}{\partial\rho} - \frac{1}{\rho^2}\right) g_1(\rho) = \xi^2 g_1(\rho) \quad (2-25)$$

Our Green's function problem has now been reduced to a one dimensional problem, namely,

$$-\left(\frac{\partial^2}{\partial z^2} + k_z^2\right) \hat{G}_1 = \delta(z - z') \quad (2-26)$$

$$\lim_{z \rightarrow -\infty} \hat{G}_1(z, z') = 0$$

$$\lim_{z \rightarrow 0} \frac{\partial \hat{G}_1(z, z')}{\partial z} = 0$$

where $\hat{G}_1 = G_1/B(\xi\rho')$, $k_z^2 = k^2 - \xi^2$, and the imaginary part of k_z is assumed to be negative. The solution for \hat{G}_1 is easily determined by applying the given boundary conditions along with the continuity and jump conditions at $z = z'$. The result is

$$\hat{G}_1(z, z') = \begin{cases} -\frac{ie^{ik_z z}}{k_z} \cos k_z z' & z < z' \\ -\frac{ie^{ik_z z'}}{k_z} \cos k_z z & z > z' \end{cases} \quad (2-27)$$

To transform (2-27) back to ρ space, we use (2-22) to obtain

$$g_1(\rho, \rho' | z, z') = \begin{cases} -i \int_0^\infty \frac{B(\xi\rho)B(\xi\rho')}{k_z H_0^{(1)}(\xi a) H_0^{(2)}(\xi a)} e^{ik_z z} \cos k_z z' \xi d\xi & z < z' \\ -i \int_0^\infty \frac{B(\xi\rho)B(\xi\rho')}{k_z H_0^{(1)}(\xi a) H_0^{(2)}(\xi a)} e^{ik_z z'} \cos k_z z \xi d\xi & z > z' \end{cases} \quad (2-28)$$

Because of the symmetry between g_1 and g_2 , we need only replace z by $-z$ and z' by $-z'$ in g_1 to obtain g_2 . The result is

$$g_2(\rho, \rho' | z, z') = \begin{cases} -i \int_0^\infty \frac{B(\xi\rho)B(\xi\rho')}{k_z H_0^{(1)}(\xi a) H_0^{(2)}(\xi a)} e^{-ik_z z'} \cos k_z z \xi d\xi & z < z' \\ -i \int_0^\infty \frac{B(\xi\rho)B(\xi\rho')}{k_z H_0^{(1)}(\xi a) H_0^{(2)}(\xi a)} e^{-ik_z z} \cos k_z z' \xi d\xi & z > z' \end{cases} \quad (2-29)$$

In (2-28), we formulated the Green's function by using a spectral expansion in ρ and obtaining a closed form Green's function in z . Another form of the same

Green's function can be determined by using a spectral expansion in z and the closed form Green's function in (2-20). The spectral expansion in this case is well known and leads to the following cosine transform pair:

$$g(z) = \int_0^\infty G(\beta) \cos \beta z d\beta \quad (2-30)$$

$$G(\beta) = \frac{2}{\pi} \int_0^\infty g(z') \cos \beta z' dz' \quad (2-31)$$

With the help of the cosine transform pair and (2-20), we can get an alternate expression for the Green's function in both regions using the same methods that which we used to derive (2-28). The final Green's function expression in Region 1 is

$$g_1(\rho, z | \rho', z') = \begin{cases} - \int_0^\infty \frac{H_1^{(2)}(k_\beta \rho')}{H_0^{(2)}(k_\beta a)} B(k_\beta \rho) \cos \beta z \cos \beta z' d\beta & \rho < \rho' \\ - \int_0^\infty \frac{H_1^{(2)}(k_\beta \rho)}{H_0^{(2)}(k_\beta a)} B(k_\beta \rho') \cos \beta z \cos \beta z' d\beta & \rho > \rho' \end{cases} \quad (2-32)$$

where $k_\beta^2 = k^2 - \beta^2$ and the imaginary part of k_β negative. Because of the symmetry between the two regions, we realize that

$$g_1(\rho, z | \rho', z') = g_2(\rho, z | \rho', z') \quad (2-33)$$

The choice of which Green's function form to use is dependent upon numerical considerations. The integral in (2-32) is not easily evaluated because of the singularity in the integrand at $k_\beta = 0$. On the other hand, the singularities in the integrand in (2-28) are much easier to handle. Indeed, they can be extracted by analytical means. We therefore use (2-28) and (2-29) for our Green's functions.

2.3 Source Analysis

Now that the solutions for the Green's functions have been obtained, it becomes necessary to specify the source M_ϕ in (2-15). We seek a source which produces a *TEM*-like wave in the region around the aperture. Let us consider the following source:

$$M_\phi(\rho, z) = \begin{cases} \frac{M_0 \delta(z)}{\rho} & \rho \in (a, c) \\ 0 & \text{otherwise} \end{cases} \quad (2-34)$$

where M_0 is a constant and d is the distance from the aperture to the source in Region 1. The variable c has a finite value and is greater than a . The source can be realized by considering a coaxial line joined to a half-space with the inner conductor extending into the half-space. A diagram of this is shown in Figure 2-2. By substituting (2-28) and (2-34) into the first term on the right hand side of (2-15) (which we will call Ψ) and evaluating the ρ' and z' integrals, we get the following expression for Ψ :

$$\begin{aligned} \Psi &= -i\omega\epsilon_0 \int_{-\infty}^0 \int_a^c g_1(\rho, z | \rho', z') \frac{M_0 \delta(z' + d)}{\rho'} \rho' d\rho' dz' \\ &= \frac{kM_0}{\eta} \int_0^\infty \frac{B(\xi\rho)A(\xi c)}{k_z H_0^{(1)}(\xi a) H_0^{(2)}(\xi a)} e^{-ik_z d} \cos k_z z d\xi \end{aligned} \quad (2-35)$$

where η is the free space impedance given by $\eta = \sqrt{\mu_0/\epsilon_0}$ and

$$A(\xi c) = J_0(\xi c)Y_0(\xi a) - J_0(\xi a)Y_0(\xi c)$$

We may obtain a solution in which all radiated fields are transverse to the direction of propagation (in this case, the z -direction) by taking the limit as $c \rightarrow \infty$. We shall call this solution the *TEM* solution. We write (2-34) as

$$M_\phi(\rho, z) = \frac{M_0 \delta(z + d)}{\rho} \quad \rho \in (a, \infty) \quad (2-36)$$

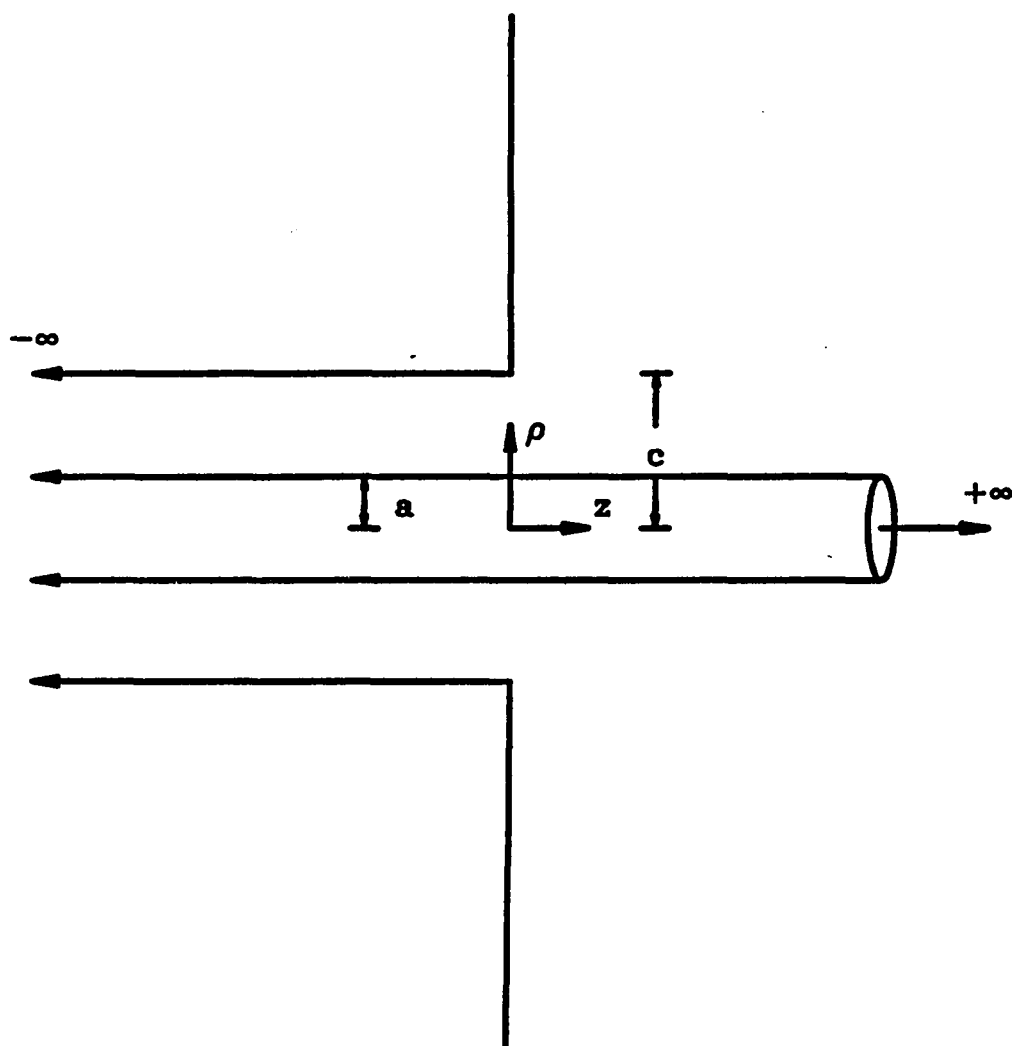


Figure 2-2 Coaxial line joined to a half-space with the inner conductor extending into the half-space.

This allows us to evaluate Ψ analytically. Starting with the first equality in (2-35), we evaluate the z' integral to obtain

$$\Psi = -\frac{kM_0}{\eta} \int_a^\infty \int_0^\infty \frac{B(\xi\rho)B(\xi\rho')}{k_z H_0^{(1)}(\xi a) H_0^{(2)}(\xi a)} e^{-ik_z d} \cos k_z z \xi d\xi d\rho' \quad (2-37)$$

Appendix A provides a useful identity for evaluating (2-37) analytically, viz:

$$\delta(\xi) = \frac{2}{\pi H_0^{(1)}(\xi a) H_0^{(2)}(\xi a)} \int_a^\infty B(\xi\rho) d\rho \quad (2-38)$$

Substituting (2-38) into (2-37) and evaluating the double integral, we get

$$\Psi = -\frac{M_0 e^{-ikd}}{\eta\rho} \cos k_z z \quad (2-39)$$

where we have used the fact that $\xi B(\xi\rho) \rightarrow 2/(\pi\rho)$ as $\xi \rightarrow 0$. Physically, we can think of Ψ as the fields in the Green's function geometry g_1 (Fig. 2-1) due to the source. For the case where $c \rightarrow \infty$, the source launches a TEM wave which is totally reflected by the shorting plate at $z = 0$. This can be plainly seen by rewriting (2-39) into the following form:

$$\Psi = -\frac{M_0 e^{-ikd}}{2\eta\rho} [e^{-ikz} + e^{ikz}] \quad (2-40)$$

where the e^{-ikz} term represents the forward going wave and e^{ikz} represents the reflected wave.

In taking the limit as $c \rightarrow \infty$, we have violated our initial assumption that the source is finite in extent. However, H_ϕ still satisfies the boundary conditions which we have specified in (2-7) through (2-11). Unfortunately, because the source

has infinite energy, the power propagating in the z direction is unbounded. To better understand this problem, let us consider the simple case of an infinitely long wire in free space with the source (2-36) located at the origin ($d = 0$). Since there is no shorting plate, only the forward-going wave is present; therefore, we write the field components as

$$H_{\phi TEM} = -\frac{M_0 e^{-ikz}}{2\eta\rho} \quad (2-41)$$

$$E_{\rho TEM} = -\frac{M_0 e^{-ikz}}{2\rho} \quad (2-42)$$

$$E_z TEM = 0 \quad (2-43)$$

where the TEM subscript indicates that the fields are excited by the source in (2-36). The power P_z which is propagating in the z direction is given by

$$P_z = \pi \text{Re} \int_a^\infty E_\rho H_\phi^* \rho d\rho \quad (2-44)$$

Evaluation of (2-44) shows that the power diverges as $\log \rho$. This is analogous to a plane wave in cartesian coordinates where the power is also infinite in an unbounded region. In the case of the plane wave, we assume that it is an idealized approximation of a physical source which does not produce infinite and is thus valid as an approximation. We therefore can use the same argument to justify the use of the source in (2-36). Although the idealized source is not realizable, there are several advantages to using it here. It allows us to simplify the incident field expression analytically rather than having to determine it numerically. Another very important advantage is that it allows us to obtain a better understanding of the problem. By considering only the TEM mode, we can easily see how the screen

affects such parameters as the current on the wire. If we use a physical source such as the one shown in Figure 2-2, the results are harder to analyze since both the incident field and scattered field contain all the modes. In addition, we shall next show that our idealized source is a close approximation to sources of physical interest.

The physical source which our idealized source approximates is given in (2-34). Because we will show that this physical source produces a set of fields close to *TEM* over our region of interest, we shall refer to the result as quasi-*TEM*. To show that this is true, let us again consider the simple case of a wire in free space using the source in (2-34). The resulting expressions for the electric field are

$$E_{\rho}(\rho, z) = \frac{M_0}{2} \int_0^{\infty} \frac{B(\xi\rho)A(\xi c)}{H_0^{(1)}(\xi a)H_0^{(2)}(\xi a)} e^{-ik_z z} d\xi \quad (2-45)$$

$$E_z(\rho, z) = -\frac{iM_0}{2\rho} \int_0^{\infty} \frac{A(\xi\rho)A(\xi c)}{k_z H_0^{(1)}(\xi a)H_0^{(2)}(\xi a)} e^{-ik_z z} \xi d\xi \quad (2-46)$$

The numerical techniques used to evaluate the integrals in (2-45) and (2-46) will not be presented here. Instead, a thorough discussion on this subject will be presented in subsequent chapters. For now we will assume that these integrals can be evaluated and proceed with the numerical results.

In order to verify our claim that (2-45) and (2-46) closely approximate the fields which are produced by the *TEM* mode, we will compare them to (2-42) and (2-43). We begin by examining the ratios $E_{\rho}/E_{\rho TEM}$ and E_z/E_{ρ} for values of ρ at a fixed z . It is hoped that for large values of z the ratio $E_{\rho}/E_{\rho TEM}$ is constant and the ratio E_z/E_{ρ} is small for any frequency and any value of ρ . In Figure 2-3, the ratio $|E_{\rho}/E_{\rho TEM}|$ is plotted for ρ going from 0.01 meters to 10 meters for three frequencies. The electric field at $z = 100$ m is considered with $a = 1$ cm and

$c = 2$ cm. The plots in Figures 2-4 and 2-5 have the same parameters as the plot in Figure 2-3 except that z is set to 10 m in Figure 2-4 and c is set to 25 cm in Figure 2-5. By comparing Figure 2-3 to Figure 2-5, we notice that the only effect of a change in source size is to shift the magnitude of the curves without changing the position of any curve with respect to the other curves. As c increases the magnitude of the ratio increases; therefore, it is preferable to have as large a source as possible in order to launch a wave of significant strength. The size of the source is limited by the fact that higher order modes are generated in the coaxial line if the value of c gets too large.

Let us now consider the problem of the variation of the ratio $|E_\rho/E_{\rho TEM}|$ with respect to frequency. Consulting Figure 2-4, we see that the ratio increases only 25% as the frequency increases two orders of magnitude from 1 MHz to 100 MHz. This small change can be taken into account if any experimental work is done under steady state conditions. For example, by plotting the variation of the ratio $|E_\rho/E_{\rho TEM}|$, we can correct for the change in magnitude by either increasing or decreasing the input power appropriately for different frequencies. We also observe (Figure 2-3) that this ratio remains fairly constant for $\rho < 0.1 z$ for the frequencies considered. In general, as frequency increases, the region in which the ratio remains constant decreases. This indicates that the quasi-*TEM* result behaves more like the *TEM* mode at lower frequencies and in regions where $\rho \ll z$. Since the fields near the wire are more important in our calculations for the aperture penetration problem, E_ρ is a good approximation for $E_{\rho TEM}$ as long as the source is far enough away from the aperture.

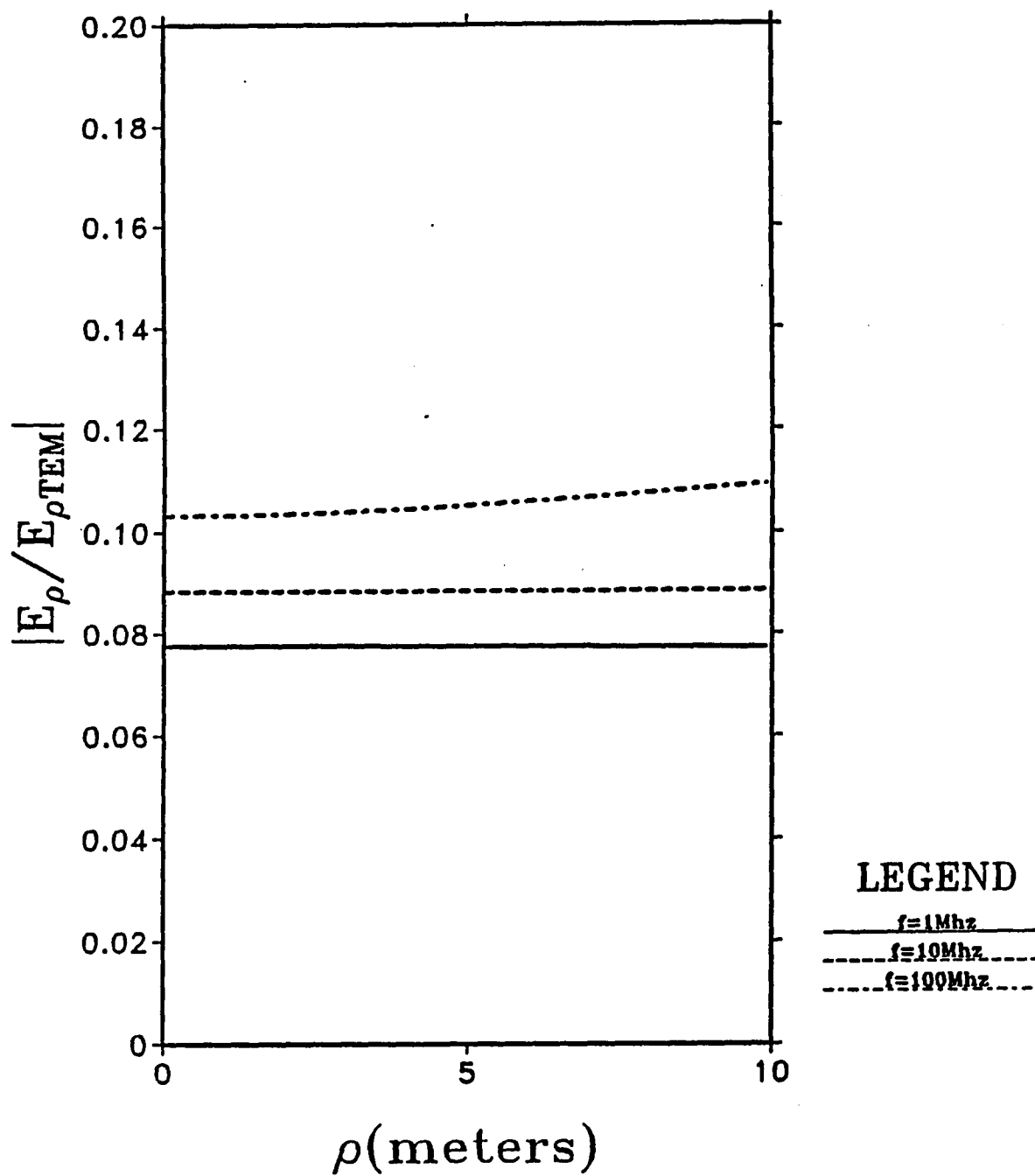


Figure 2-3 Normalized E_ρ due to an approximate source with $z = 100$ m and $b/a = 2$.

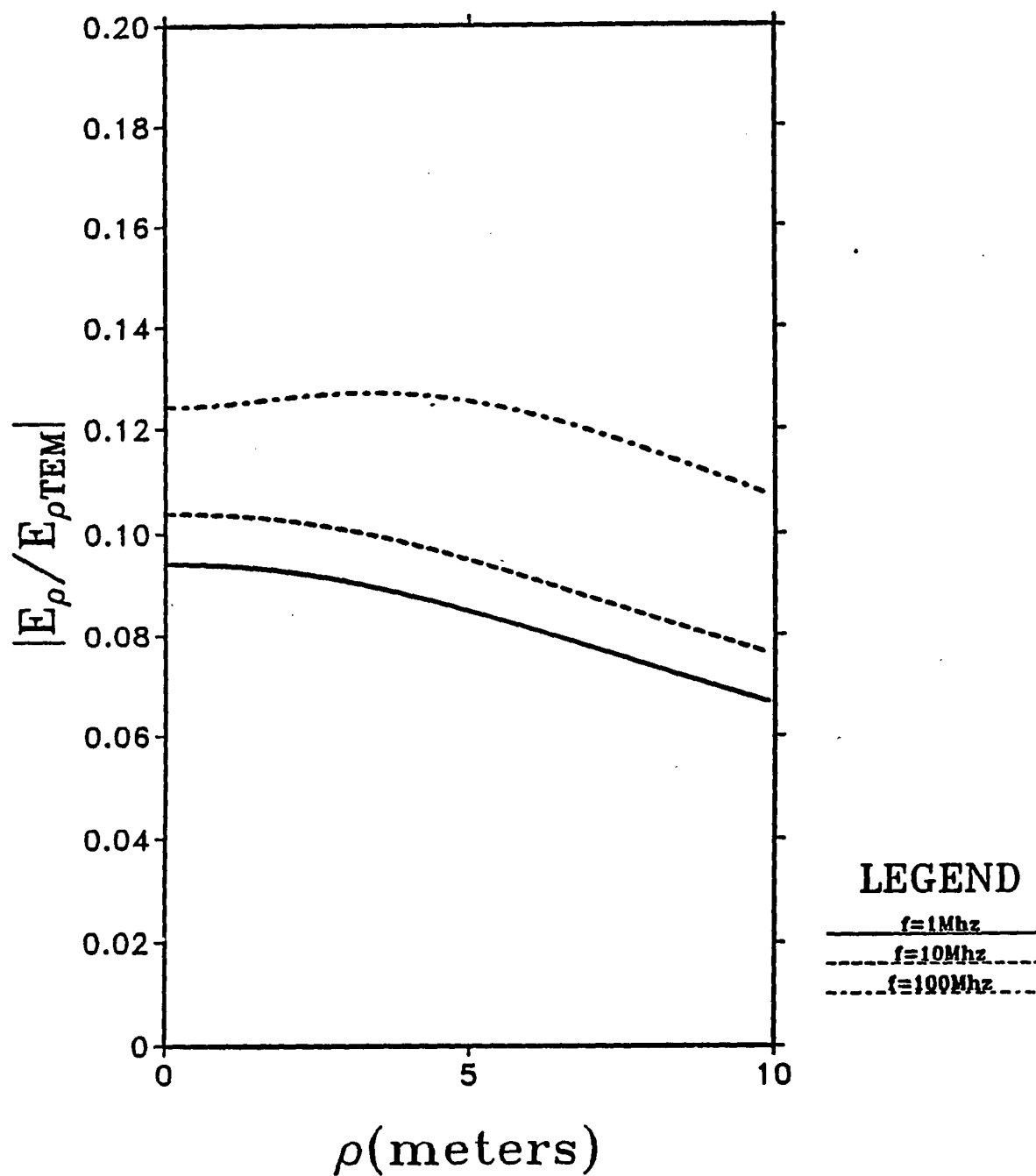


Figure 2-4 Normalized E_ρ due to an approximate source with $z = 10$ m and $b/a = 2$.

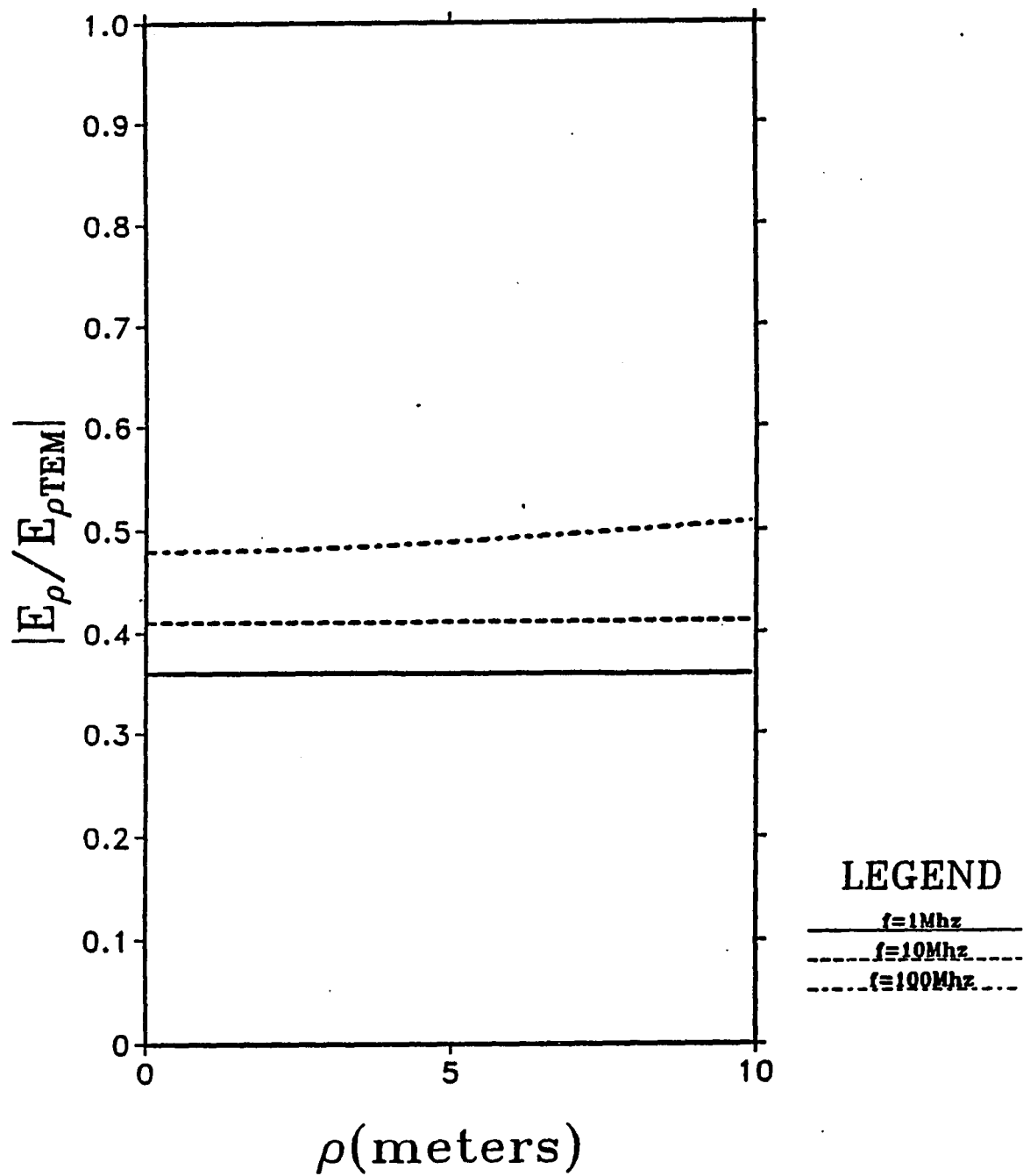


Figure 2-5 Normalized E_ρ due to an approximate source with $z = 100 \text{ m}$ and $b/a = 25$.

In Figures 2-6 through 2-8, ratios of $|E_z/E_\rho|$ are plotted using the same parameters as those used in the figures for $|E_\rho/E_{\rho TEM}|$. For $\rho < 0.1 z$, we observe that $|E_z| \leq 0.01|E_\rho|$. This indicates that for large z , E_z closely approximates $E_{z TEM}$ for a large region around the wire. We also notice that the source size has almost no effect on the ratio $|E_z/E_\rho|$.

An alternate method is to show that the current behaves like a *TEM* mode current. An analytical solution was obtained by Wait and Hill (1979) for the infinite wire with our physical source. They showed the behavior of the current for large values of z to be approximately,

$$I(z) \sim \frac{e^{-ikz}}{\ln z} \quad (2-47)$$

Since the natural logarithm is very slowly varying, this behavior is close to *TEM*.

From the numerical results shown here, we can conclude that although the approximate source does not give perfect results, it is close enough if considered within its region of validity (i.e., far from the source). For the numerical computations throughout this paper, we will use the idealized source to obtain our results.

2.4 Integral Equation

The terms in (2-15) and (2-16) that are as yet unknown are the aperture electric fields, $E_{\rho 1}(\rho', 0)$ and $E_{\rho 2}(\rho', 0)$. To determine these we invoke the continuity of the tangential electric and magnetic fields across the aperture, viz:

$$E_{\rho 1}(\rho', 0) = E_{\rho 2}(\rho', 0) \equiv E_A(\rho') \quad \rho' \in (a, b) \quad (2-48)$$

$$H_{\phi 1}(\rho, 0) = H_{\phi 2}(\rho, 0) \quad \rho \in (a, b) \quad (2-49)$$

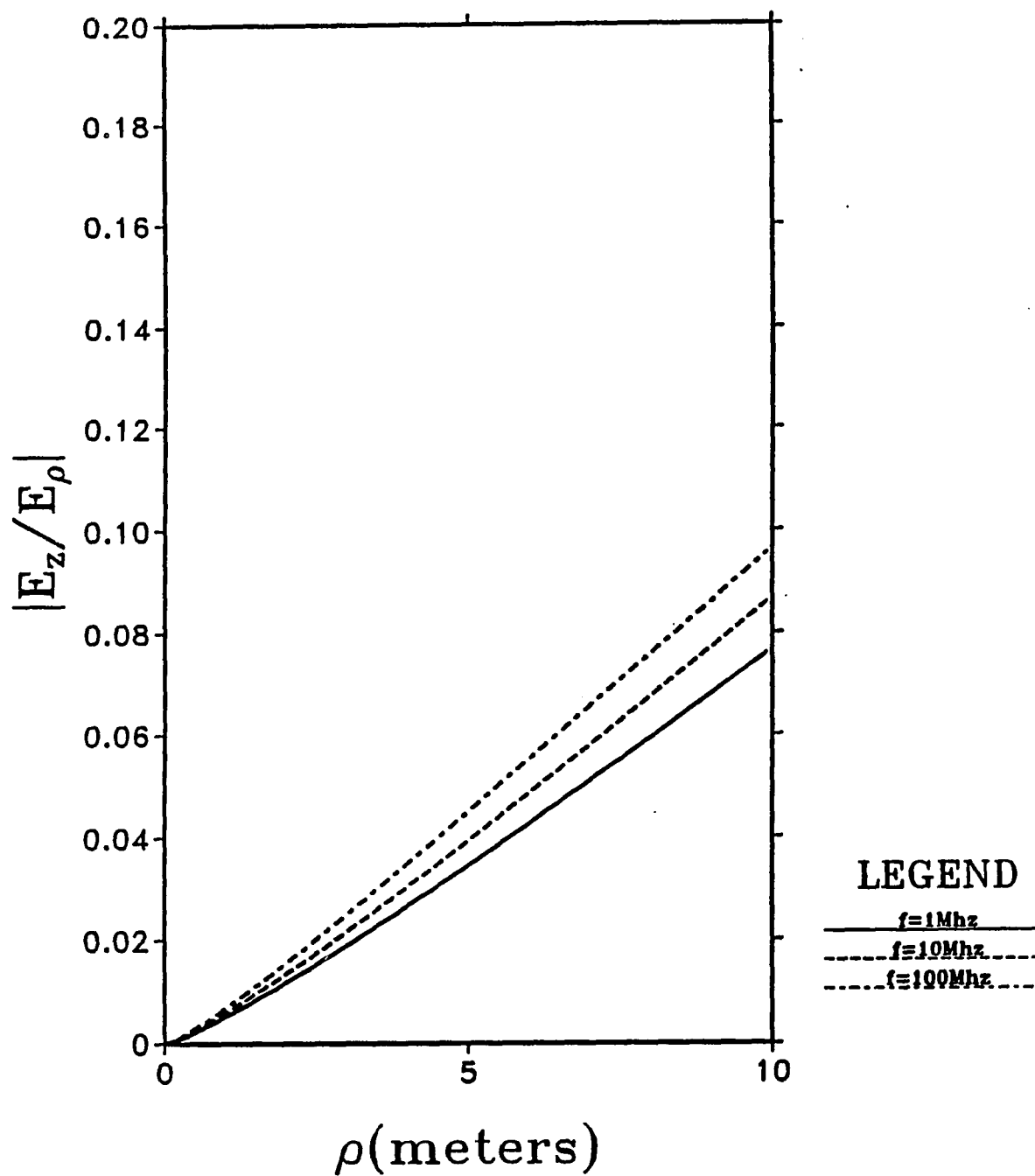


Figure 2-6 Normalized E_z due to an approximate source with $z/a = 100$ m and $b/a = 2$.

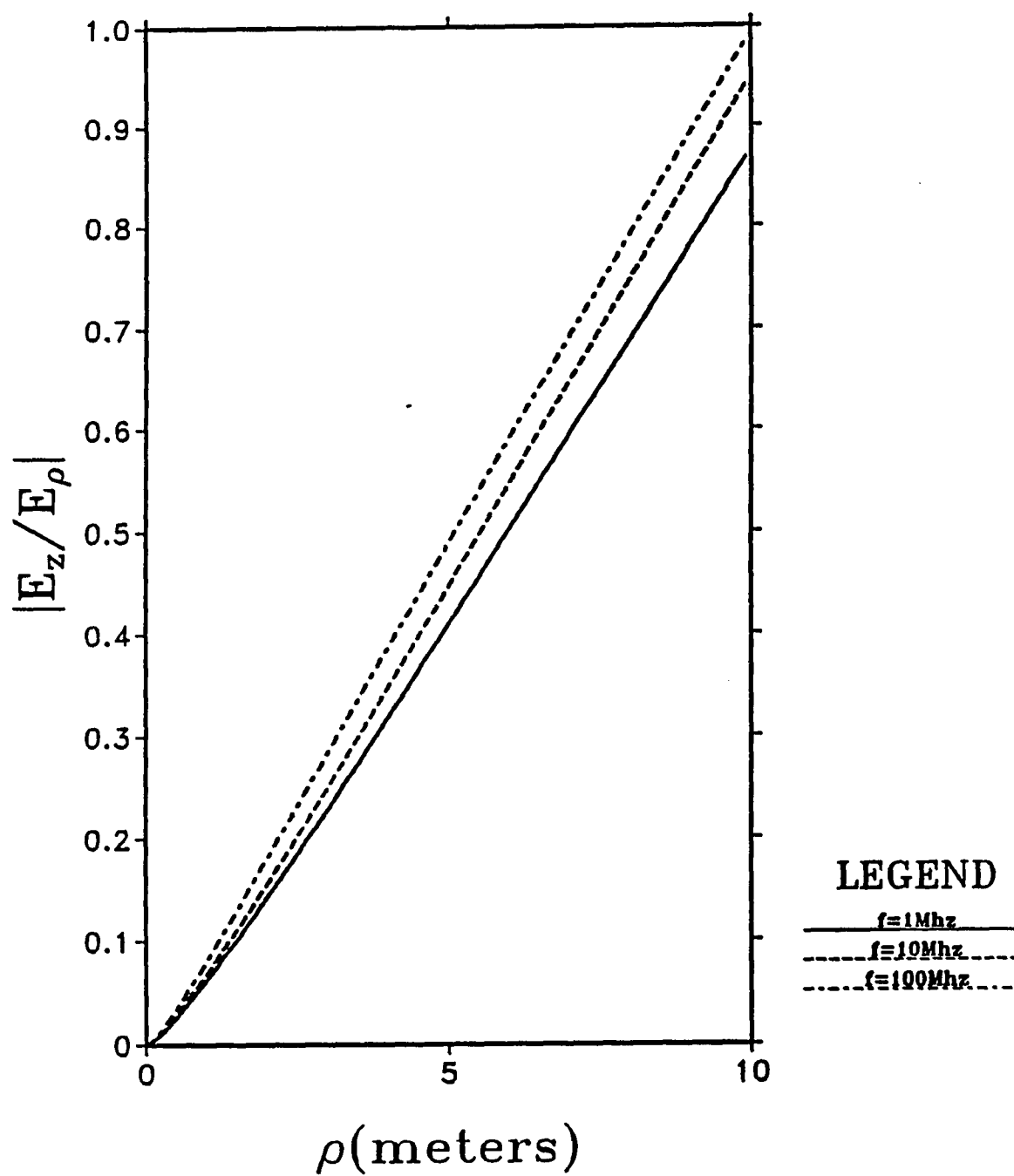


Figure 2-7 Normalized E_z due to an approximate source with $z = 10$ m and $b/a = 2$.

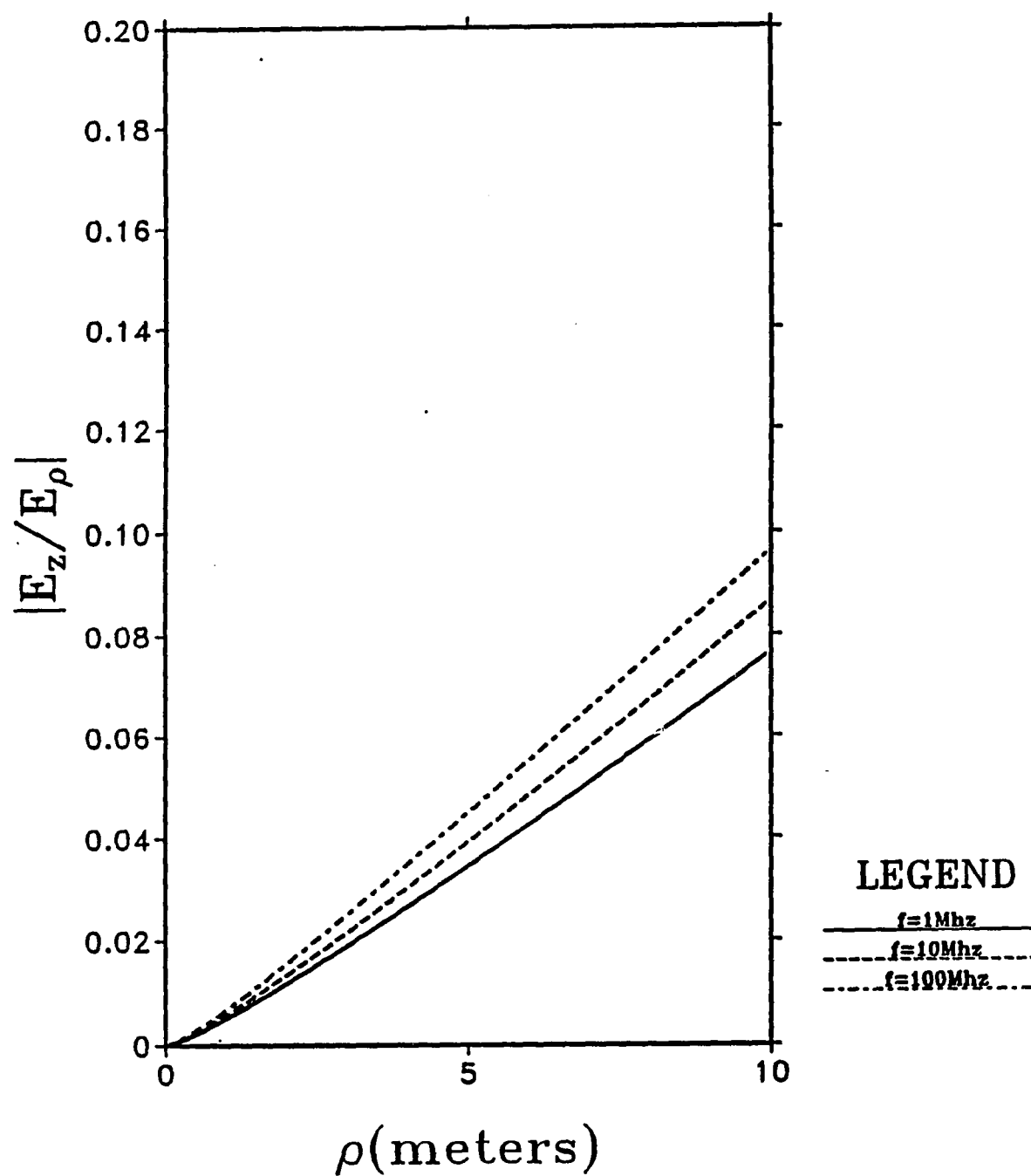


Figure 2-8 Normalized E_z due to an approximate source with $z = 100$ m and $b/a = 25$.

Substituting (2-39) into (2-15) and using the above boundary conditions to equate (2-15) and (2-16) at the aperture, we obtain the following Fredholm integral equation of the first kind:

$$-\frac{M_0 e^{-ikd}}{2\eta\rho} = i\omega\epsilon_0 \int_a^b g_1(\rho, 0 | \rho', 0) E_A(\rho') \rho' d\rho' \quad \rho \in (a, b) \quad (2-50)$$

where we have used the fact that $g_1(\rho, 0 | \rho', 0) = g_2(\rho, 0 | \rho', 0)$. Once we have solved the integral equation for $E_A(\rho')$, all the necessary ingredients are present to evaluate (2-15) and (2-16) for the magnetic fields. Unfortunately, the integral equation is not solvable by analytical means, and approximate methods of solution must be considered.

Before we proceed further, we need to investigate the behavior of the singularity in the kernel of our integral equation. The singularity must be weak enough for there to be a solution. The kernel in this case is the Green's function $g_1(\rho, 0 | \rho', 0)$ with the singularity located at $\rho = \rho'$. To evaluate the singularity, it is convenient to consider the following separation of the integral in the Green's function:

$$g_1(\rho, 0 | \rho', 0) = -i \left\{ \int_0^{2k} \Omega d\xi + \int_{2k}^{\infty} \Omega d\xi \right\} \quad (2-51)$$

where

$$\Omega = \frac{B(\xi\rho)B(\xi\rho')\xi}{k_z H_0^{(1)}(\xi a) H_0^{(2)}(\xi a)}$$

Although there are singularities in the integrand on the interval $(0, 2k)$, the singularities are weak enough that the integral on this interval is well-behaved; therefore, the first integral in (2-22) produces no singular behavior in g_1 . The singularity in

g_1 occurs in the second integral. We can extract the singularity from the second integral by subtracting the asymptotic form of Ω and adding its integral back into the expression. Let Φ represent the asymptotic form of Ω . We obtain

$$\int_{2k}^{\infty} \Omega d\xi = \int_{2k}^{\infty} (\Omega - \Phi) d\xi + S \quad (2-52)$$

where

$$\Phi = \frac{2 \cos \xi(\rho - a) \cos \xi(\rho' - a)}{\pi \xi \sqrt{\rho \rho'}}$$

and

$$\begin{aligned} S &= \int_{2k}^{\infty} \Phi d\xi \\ &= \frac{-1}{\pi \sqrt{\rho \rho'}} [Ci(2k(\rho - \rho')) + Ci(2k(\rho + \rho' - 2a))] \end{aligned}$$

The symbol Ci represents the cosine integral. Since the cosine integral behaves as a natural log function for small arguments, S , and therefore g_1 , has a logarithmic singularity at $\rho = \rho'$.

CHAPTER 3

EQUIVALENT CIRCUIT MODEL

In this chapter we formulate expressions for the admittance and the current. This requires the solution of the integral equation in (2-50). We first solve the integral equation by means of a zeroth order approximation of the aperture field. Next, we solve the integral equation by using a method of moments approximation. This allows us to solve for the admittance and the current using both approximations. We then obtain numerical results for both approximations and compare them. Next, an analysis is performed on the circuit parameters. Finally, we consider the time domain response to a transient pulse.

3.1 Formulation of Circuit Parameter Expressions

An important parameter in the equivalent circuit is the current on the wire. To obtain the incident current, let us consider the problem of an infinitely long wire in free space with the source given by (2-34). An expression for the incident current can be formulated by using the equation relating the surface current density \vec{J}_s to the tangential magnetic field at the wire, viz:

$$\vec{J}_s = \hat{n} \times \vec{H} |_{\rho=a} \quad (3-1)$$

where \hat{n} is the unit vector pointing outward from the wire. The magnetic field in this case is equivalent to the magnetic field in (2-39). The current on the wire is

given by

$$I(z) = \int_0^{2\pi} J_s|_{\rho=a} a d\phi \quad (3-2)$$

Substitution of (2-39) into (3-1) and (3-1) into (3-2) gives

$$I(z) = I_0 e^{-ikz} \quad (3-3)$$

where

$$I_0 = -\frac{M_0 \pi e^{-ikd}}{\eta}$$

Since I_0 represents the magnitude of the incident current, results in this work will be normalized to this value rather than the strength of the magnetic current source M_0 .

Returning to the case where the screen is present, we recognize the fact that a general expression for the current can be written by using the magnetic field expressions from (2-15) and (2-16) in (3-2). This yields the following expression for the current on both sides of the screen:

$$I(z) = \begin{cases} \frac{4k}{\eta} \int_a^b \int_0^\infty \frac{B(\xi\rho')e^{-ik_z z}}{H_0^{(1)}(\xi a)H_0^{(2)}(\xi a)} d\xi E_A(\rho')\rho' d\rho' & z > 0 \\ 2I_0 \cos kz - \frac{4k}{\eta} \int_a^b \int_0^\infty \frac{B(\xi\rho')e^{ik_z z}}{H_0^{(1)}(\xi a)H_0^{(2)}(\xi a)} d\xi E_A(\rho')\rho' d\rho' & z < 0 \end{cases} \quad (3-4)$$

Since we are interested in the current coupled through the aperture, only the equation for $z > 0$ in (3-4) is pertinent to our problem.

Again, as in the case of the magnetic field, it is necessary to find $E_A(\rho')$ to solve for $I(z)$. The only exception occurs at the point $z = 0$. Because of the symmetry of the geometry about $z = 0$, we can obtain an analytical solution for the

current at that point. By substituting (2-50) into (2-16) and inserting the result into (3-2), we get

$$I(z) |_{z=0} = I_0 \quad (3-5)$$

At first this may seem unusual since this means that the screen has no effect upon the incident current at the aperture, but because H_ϕ is the same value on both sides of the screen at $z = 0$, the surface currents induced on one side of the screen by the magnetic field are the negative of the surface currents induced on the other side. Consequently, the screen has no net effect upon the incident current at the aperture.

It is convenient in many cases to consider our electromagnetic model in terms of an equivalent circuit model. Much of modern electromagnetic equivalent circuit theory is due to Schelkunoff (1943) and Marcuvitz (1951). An equivalent circuit model for the present problem has been deduced by Casey (1987) (Figure 3-1). Since I_0 is the incident current, the short-circuit current is represented by $2I_0$. The admittance Y_A is composed of a conductance G_A and a susceptance B_A . The voltage V_0 is the voltage across the aperture and is defined by

$$V_0 \equiv \int_a^b E_A(\rho) d\rho \quad (3-6)$$

where the aperture electric field $E_A(\rho)$ is a quantity to be determined from the integral equation in (2-50). From the equivalent circuit model, we conclude that

$$Y_A = \frac{2I_0}{V_0} \quad (3-7)$$

The validity of the circuit model is supported by our result for the current at the aperture. We have previously shown in (3-5) that the current in the aperture is

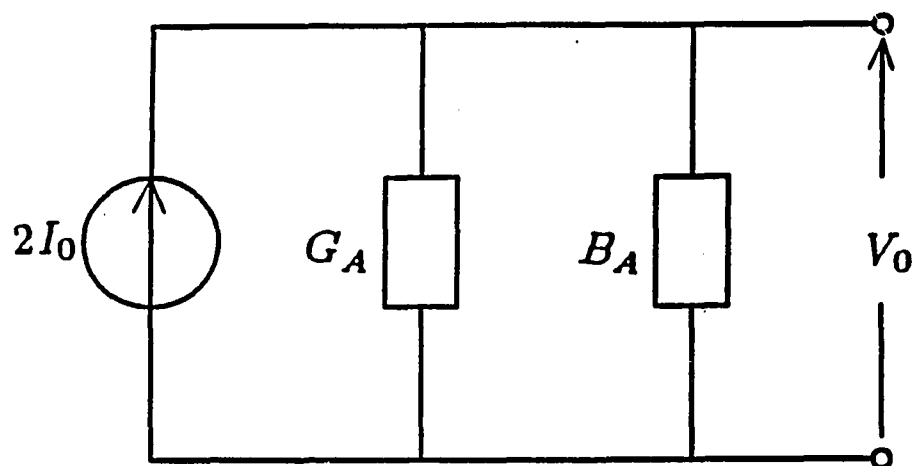


Figure 3-1 Equivalent circuit model for the wire penetrating the aperture.

equal to I_0 . Let us attempt to deduce this result from our circuit model. The admittance can be divided into a part for $z < 0$ and a part for $z > 0$ (Figure 3-2). Since the geometry is symmetric around the point $z = 0$, the admittances for the two parts are equal. Thus, the current at the aperture must be equal to I_0 which agrees with our mathematical result.

3.2 Zeroth Order(ZO) Approximation

Both the admittance and the current are dependent upon the solution of (2-50), but this integral equation is not solvable analytically. We can, however, render the integral equation degenerate by making an approximation on the aperture field $E_A(\rho')$. A very good low frequency approximation would be the quasi-static solution (Meixner, 1972),

$$E_A(\rho') = \frac{C}{\rho'(\rho'^2 - b^2)^{\frac{1}{2}}} \quad \rho' \in (a, b) \quad (3-8)$$

where C is a constant. This approximation accounts for both the edge singularity at $\rho' = b$ and the $1/\rho'$ variation of the field away from the wire. Unfortunately, the resulting ρ' integral must still be evaluated numerically; therefore, let us instead look for an approximation whereby the ρ' integral can be evaluated analytically. In this vein, a much more analytically appealing idea would be to approximate the aperture field by

$$E_A(\rho') = \frac{C}{\rho'} \quad \rho' \in (a, b) \quad (3-9)$$

where, again, C is a constant. Although this is not a very good approximation for the aperture field, it is an adequate low frequency approximation when used to calculate equivalent circuit parameters. Indeed, Williamson (1985) has shown

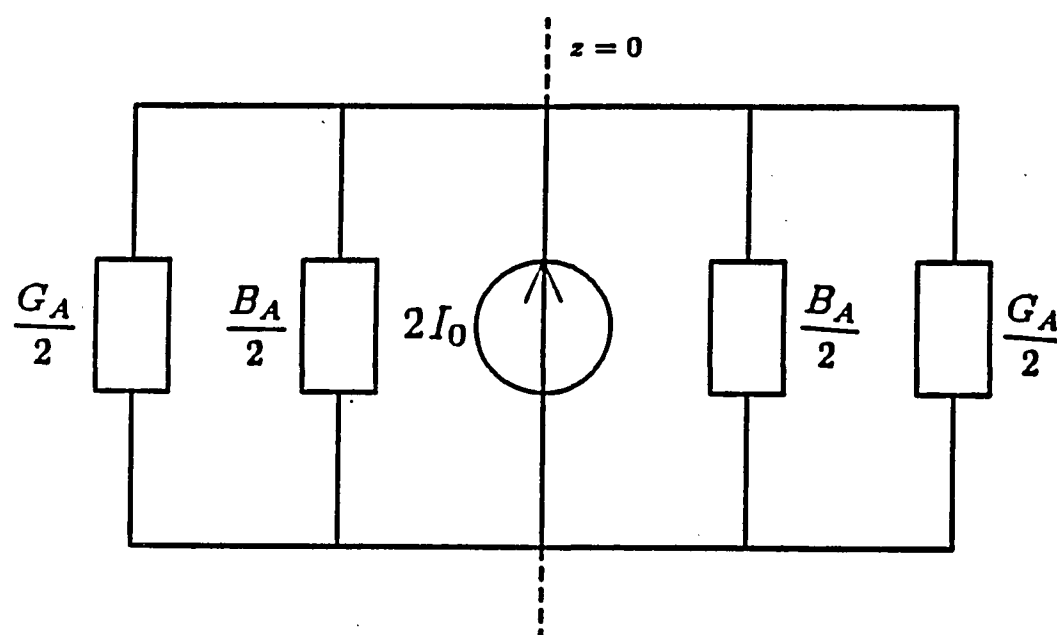


Figure 3-2 Equivalent circuit model referenced to the aperture plane.

that circuit parameters such as admittances are largely insensitive to the localized behavior of the aperture field at low frequencies.

We need now only solve for the constant C . By substituting (3-9) into (2-50) and evaluating the integral with respect to ρ' , we obtain

$$\frac{I_0}{2\pi\rho} = -\frac{kC}{\eta} \int_0^\infty \frac{B(\xi\rho)A(\xi b)}{k_x H_0^{(1)}(\xi a) H_0^{(2)}(\xi a)} d\xi \quad \rho \in (a, b) \quad (3-10)$$

We next integrate both sides of (3-10) with respect to ρ from a to b and solve for C . This yields

$$C = \frac{I_0 \eta \ln(\frac{b}{a})}{2\pi F} \quad (3-11)$$

where

$$F = k \int_0^\infty \frac{A^2(\xi b)}{\xi k_x H_0^{(1)}(\xi a) H_0^{(2)}(\xi a)} d\xi \quad (3-12)$$

We normalize distances by making the change of variable $\xi = k\gamma$ in F . The result is

$$F = \int_0^\infty \frac{A^2(kb\gamma)}{(1-\gamma^2)^{\frac{1}{2}} \gamma H_0^{(1)}(ka\gamma) H_0^{(2)}(ka\gamma)} d\gamma \quad (3-13)$$

From (3-13), we can now obtain expressions for both the admittance and current in terms of F . Substituting (3-11) into (3-9) and then (3-9) into (3-7) yields

$$Y_A = \frac{4\pi}{\eta \ln^2(\frac{b}{a})} F \quad (3-14)$$

Since the integral F can easily be separated into a real and imaginary term, we can separate the admittance Y_A into its conductance and susceptance terms, viz:

$$\begin{aligned} Y_A &= G_A + iB_A \\ &= \frac{4\pi}{\eta \ln^2(\frac{b}{a})} \text{Re}(F) + i \frac{4\pi}{\eta \ln^2(\frac{b}{a})} \text{Im}(F) \end{aligned} \quad (3-15)$$

where

$$\begin{aligned} \text{Re}(F) &= \int_0^1 \frac{A^2(kb\gamma)}{(1-\gamma^2)^{\frac{1}{2}} \gamma H_0^{(1)}(ka\gamma) H_0^{(2)}(ka\gamma)} d\gamma \\ \text{Im}(F) &= \int_1^\infty \frac{A^2(kb\gamma)}{(\gamma^2-1)^{\frac{1}{2}} \gamma H_0^{(1)}(ka\gamma) H_0^{(2)}(ka\gamma)} d\gamma \end{aligned}$$

Since F cannot be evaluated analytically, we must use numerical means. In attempting to evaluate (3-13) by using standard integration techniques, complications arise due to the singularities in the integrand at $\gamma = 0$ and $\gamma = 1$. These singularities must be extracted from the integral and handled analytically. Also, because the upper limit of the integral is infinite, we must find a way to truncate the integral in such a way that we limit the computation time required to evaluate the integral while at the same time maintaining our accuracy. The numerical integration techniques which are used here are presented in Appendix B. The final form for F is

$$\begin{aligned} F &= \int_0^\delta \left[\frac{A^2(kb\gamma)}{\gamma(1-\gamma^2)^{\frac{1}{2}} H_0^{(1)}(ka\gamma) H_0^{(2)}(ka\gamma)} - \frac{\ln^2(\frac{b}{a})}{\gamma[\frac{\pi^2}{4}(\ln(\frac{ka}{2}) + \Gamma)^2]} \right] d\gamma \\ &+ R_1 + \int_{\arcsin(\delta)}^{\frac{\pi}{2}} \frac{A^2(kb \sin \theta)}{\sin \theta H_0^{(1)}(ka \sin \theta) H_0^{(2)}(ka \sin \theta)} d\theta \\ &+ i \int_2^\infty \left\{ \frac{A^2(kb\gamma)}{(\gamma^2-1)^{\frac{1}{2}} \gamma H_0^{(1)}(ka\gamma) H_0^{(2)}(ka\gamma)} - \frac{2 \sin^2 k(b-a)\gamma}{\pi kb\gamma^3} \right\} d\gamma \end{aligned}$$

$$+ R_2 + i \int_0^{\frac{\pi}{3}} \frac{A^2(kb \sec \theta)}{H_0^{(1)}(ka \sec \theta) H_0^{(2)}(ka \sec \theta)} d\theta \quad (3-16)$$

where

$$R_1 = \ln^2\left(\frac{b}{a}\right) \left\{ 1 + \frac{2}{\pi} \arctan \left[\frac{2}{\pi} \left(\ln\left(\frac{ka\delta}{2}\right) + \Gamma \right) \right] \right\}$$

$$R_2 = \frac{i(k(b-a))^2}{\pi kb} \left[\frac{\sin^2 2k(b-a)}{(2k(b-a))^2} + \frac{\sin 4k(b-a)}{2k(b-a)} - 2Ci(4k(b-a)) \right]$$

We next consider the current on the wire. Substituting our aperture field approximation (3-9) into the integral equation for the current (3-4), we find that the integral equation degenerates into a double integral in ρ' and ξ . By making the same change of variable as that made in (3-13) and evaluating the ρ' integral, we obtain

$$I(z) = -\frac{8I_0}{\pi\eta Y_A \ln(\frac{b}{a})} \int_0^\infty \frac{A(kb\gamma)e^{-ikz(1-\gamma^2)^{\frac{1}{2}}}}{(1-\gamma^2)^{\frac{1}{2}}\gamma H_0^{(1)}(ka\gamma)H_0^{(2)}(ka\gamma)} d\gamma \quad (z > 0) \quad (3-17)$$

Note that the current is a function of Y_A ; therefore, we must solve for F to obtain a solution for the current. The numerical integration techniques given in Appendix B are also used to evaluate the integral in (3-16). The result is

$$I(z) = -\frac{8I_0}{\pi\eta Y_A \ln(\frac{b}{a})} \left\{ \int_0^\delta \left[\frac{A(kb\gamma)e^{-ikz(1-\gamma^2)^{\frac{1}{2}}}}{\gamma(1-\gamma^2)^{\frac{1}{2}}H_0^{(1)}(ka\gamma)H_0^{(2)}(ka\gamma)} + \frac{\pi \ln(\frac{b}{a})e^{-ikz}}{2\gamma[\frac{\pi^2}{4}(\ln(\frac{ka}{2}) + \Gamma)^2]} \right] d\gamma \right.$$

$$- R_3 + \int_{\arcsin(\delta)}^{\frac{\pi}{2}} \frac{A(kb \sin \theta)e^{-ikz \cos \theta}}{\sin \theta H_0^{(1)}(ka \sin \theta) H_0^{(2)}(ka \sin \theta)} d\theta$$

$$\left. + i \int_2^\infty \left\{ \frac{A(kb\gamma)e^{-kz(\gamma^2-1)^{\frac{1}{2}}}}{(\gamma^2-1)^{\frac{1}{2}}\gamma H_0^{(1)}(ka\gamma)H_0^{(2)}(ka\gamma)} + \frac{e^{-kz\gamma} \sin k(b-a)\gamma}{\sqrt{\frac{b}{a}\gamma^2}} \right\} d\gamma \right.$$

$$- R_4 + i \int_0^{\frac{\pi}{3}} \frac{A(kb \sec \theta) e^{-kz \tan \theta}}{H_0^{(1)}(ka \sec \theta) H_0^{(2)}(ka \sec \theta)} d\theta \} \quad (3-18)$$

where

$$R_3 = \frac{\pi}{2} \ln\left(\frac{b}{a}\right) e^{-ikz} \left\{ 1 + \frac{2}{\pi} \arctan \left[\frac{2}{\pi} \left(\ln\left(\frac{ka\delta}{2}\right) + \Gamma \right) \right] \right\}$$

and

$$R_4 = \frac{i}{2\sqrt{b/a}} \left[e^{-2kz} \sin 2k(b-a) - (k(b-a) + ikz) E_1(2kz - i2k(b-a)) \right. \\ \left. + (k(b-a) - ikz) E_1(2kz + i2k(b-a)) \right]$$

The exponential integral E_1 must be specially treated since its argument is complex. For small arguments, a series expansion is used to evaluate E_1 while for large arguments we use Laguerre Quadrature (Todd, 1954). One problem which is not taken into consideration in Appendix B is the oscillatory nature of the exponential term $e^{-ikz(1-\gamma^2)^{\frac{1}{2}}}$. For large values of kz , the number of oscillations for γ between 0 and 1 is considerable. This behavior is the limiting factor in calculating the current. As kz gets larger, the amount of computation time must increase to maintain the accuracy of the result until a point is reached at which the amount of time required becomes prohibitive. For this reason we can only compute numerical results up to a certain value of kz . This exact value is considered in the numerical results section. Another problem associated with the exponential term is that the zero crossings tend to congregate around the point $\gamma = 1$. Fortunately, the change of variable ($\gamma = \sin \theta$) in Appendix B results in a more even distribution of the zero crossings over the interval of integration.

3.3 Method of Moments(MOM) Approximation

In the previous section we obtained solutions for the admittance and current by making a zeroth order (ZO) approximation for the aperture field. However, this approximation is only valid at low frequencies. It would be useful if we could verify our approximation using a more general method. One well-known technique is the method of moments (MOM) (Harrington, 1968). In this section we repeat the analysis done in the previous section except that a MOM approximation is made for the aperture field rather than the ZO approximation.

In the MOM approximation, we choose a set of expansion functions to represent the aperture field,

$$E_A(\rho') = \frac{\hat{E}_A(\rho')}{\rho'} \quad (3-19)$$

where

$$\hat{E}_A(\rho') = \sum_{j=1}^N \alpha_j P_j(\rho') \quad (3-20)$$

The α_j 's are coefficients to be determined; the value N is the number of expansion functions used to approximate $E_A(\rho')$. The *pulse* functions $P_j(\rho')$ are defined by

$$P_j(\rho') = \begin{cases} 1 & V_j < \rho' < U_j \\ 0 & \text{otherwise} \end{cases} \quad (3-21)$$

where $V_j = U_{j-1}$ and $U_j = V_j + \Delta x_j$. V_1 is the wire radius a , The pulse step Δx_j is defined to be

$$\Delta x_j = \Delta x_1 \chi^{j-1} \quad (3-22)$$

where we need to specify a value for χ between 0 and 1. Since we also specify N , we can determine Δx_1 by recognizing the fact that

$$\Delta x_1 = \frac{1 - \chi}{1 - \chi^N} (b - a) \quad (3 - 23)$$

A similar algorithm for the pulse function spacing is used by Butler (1984). Note that as χ increases, the degree of nonuniformity in the pulse spacing decreases. For $\chi = 1$, the pulse functions become equally spaced. For the weighting functions we choose delta functions located at the center of the pulse expansion functions. They are defined by

$$w_\ell(\rho) = \frac{\delta(\rho - R_\ell)}{k\rho} \quad (3 - 24)$$

where $R_\ell = (U_\ell + V_\ell)/2$.

The choice of pulses for the expansion functions simplifies the calculation of the matrix elements since it allows us to analytically evaluate one of the integrals in each of the matrix elements. The choice of the weighting functions is mainly determined by the singular behavior of the aperture field at $\rho = b$. By choosing the delta functions to be located at the center of the pulse functions, we avoid numerical instabilities which would result if the weighting function is located at an edge singularity. Furthermore, the integration involving the weighting function becomes trivial. By substituting (3-19) into (2-50) and taking the inner product of both sides of the integral equation with our weighting functions, we obtain

$$\left\langle -\frac{I_0 \eta}{2\pi\rho}, w_\ell \right\rangle = -ik \left\langle \sum_{j=1}^N \alpha_j \int_{V_j}^{U_j} g_1(\rho, 0 | \rho', 0) d\rho', w_\ell \right\rangle \quad (3 - 25)$$

for $\ell = 1, \dots, N$. In matrix form, we have

$$\begin{pmatrix} S_{11} & S_{12} & \dots & S_{1j} \\ S_{21} & S_{22} & \dots & S_{2j} \\ \vdots & \vdots & \ddots & \vdots \\ S_{\ell 1} & S_{\ell 2} & \dots & S_{\ell j} \end{pmatrix} \begin{pmatrix} \alpha_1 \\ \alpha_2 \\ \vdots \\ \alpha_j \end{pmatrix} = \begin{pmatrix} T_1 \\ T_2 \\ \vdots \\ T_\ell \end{pmatrix} \quad (3-26)$$

where the elements $S_{\ell j}$ and T_ℓ are given by

$$S_{\ell j} = -i \int_{V_j}^{U_j} g_1(R_\ell, 0 \mid \rho', 0) d\rho'$$

$$T_\ell = \frac{I_0 \eta}{2\pi k R_\ell}$$

The evaluation of the elements $S_{\ell j}$ requires the evaluation of the following double integral:

$$S_{\ell j} = - \int_{V_j}^{U_j} \int_0^\infty \frac{B(kR_\ell \gamma) B(k\rho' \gamma)}{(1 - \gamma^2)^{\frac{1}{2}} H_0^{(1)}(ka\gamma) H_0^{(2)}(ka\gamma)} \gamma d\gamma d\rho' \quad (3-27)$$

By switching the order of integration, we can evaluate the ρ' integral analytically to obtain

$$S_{\ell j} = \int_0^\infty \frac{B(kR_\ell \gamma) [A(kU_j \gamma) - A(kV_j \gamma)]}{(1 - \gamma^2)^{\frac{1}{2}} H_0^{(1)}(ka\gamma) H_0^{(2)}(ka\gamma)} d\gamma \quad (3-28)$$

We next write the integral in a form which will allow us to evaluate it numerically. The evaluation of this integral utilizes the same numerical techniques that we have used before for the integral in (3-15). An example of these techniques is given in

Appendix B. The resulting expression for $S_{\ell j}$ can now be written as follows:

$$\begin{aligned}
S_{\ell j} = & \int_0^\delta \left\{ \frac{B(kR_\ell \gamma)[A(kU_j \gamma) - A(kV_j \gamma)]}{(1 - \gamma^2)^{\frac{1}{2}} H_0^{(1)}(ka\gamma) H_0^{(2)}(ka\gamma)} + \frac{\ln(\frac{U_j}{V_j})}{\gamma k R_\ell [\frac{\pi^2}{4} + (\ln(\frac{ka\gamma}{2}) + \Gamma)^2]} \right\} d\gamma \\
& - \frac{\ln(\frac{U_j}{V_j})}{k R_\ell} \left\{ 1 + \frac{2}{\pi} \arctan \left[\frac{2}{\pi} (\ln(\frac{ka\delta}{2}) + \Gamma) \right] \right\} \\
& + \int_{\arcsin(\delta)}^{\frac{\pi}{2}} \frac{B(kR_\ell \sin \theta)[A(kU_j \sin \theta) - A(kV_j \sin \theta)]}{H_0^{(1)}(ka \sin \theta) H_0^{(2)}(ka \sin \theta)} d\theta \\
& + i \int_0^{\frac{\pi}{2}} \frac{B(kR_\ell \sec \theta)[A(kU_j \sec \theta) - A(kV_j \sec \theta)]}{\cos \theta H_0^{(1)}(ka \sec \theta) H_0^{(2)}(ka \sec \theta)} d\theta \\
& + i \int_2^\infty \left\{ \frac{B(kR_\ell \gamma)[A(kU_j \gamma) - A(kV_j \gamma)]}{(\gamma^2 - 1)^{\frac{1}{2}} H_0^{(1)}(ka\gamma) H_0^{(2)}(ka\gamma)} \right. \\
& \left. + \frac{2 \cos k\gamma(R_\ell - a)}{\pi \gamma^2 \sqrt{kR_\ell}} \left[\frac{\sin k(U_j - a)\gamma}{\sqrt{kU_j}} - \frac{\sin k(V_j - a)\gamma}{\sqrt{kV_j}} \right] \right\} d\gamma - \frac{2i}{\pi} \Phi_1 \quad (3-29)
\end{aligned}$$

where

$$\begin{aligned}
\Phi_1 = & \frac{1}{2\sqrt{kR_\ell}} \left\{ \frac{\sin 2k(U_j - R_\ell) + \sin 2k(U_j + R_\ell - 2a)}{2\sqrt{kU_j}} \right. \\
& - \frac{\sin 2k(V_j - R_\ell) + \sin 2k(V_j + R_\ell - 2a)}{2\sqrt{kV_j}} \\
& + \frac{k(V_j - R_\ell)}{\sqrt{kV_j}} Ci(2k(V_j - R_\ell)) + \frac{k(V_j + R_\ell - 2a)}{\sqrt{kV_j}} Ci(2k(V_j + R_\ell - 2a)) \\
& \left. - \frac{k(U_j - R_\ell)}{\sqrt{kU_j}} Ci(2k(U_j - R_\ell)) - \frac{k(U_j + R_\ell - 2a)}{\sqrt{kU_j}} Ci(2k(U_j + R_\ell - 2a)) \right\}
\end{aligned}$$

Knowing both $S_{\ell j}$ and T_{ℓ} , we then solve for the α_j 's and obtain the aperture field in terms of these coefficients.

We next substitute the MOM aperture field into the expressions for admittance and current. The resultant expression for the admittance is

$$Y_A = 2I_0 \left(\sum_{j=1}^N \alpha_j \ln\left(\frac{U_j}{V_j}\right) \right)^{-1} \quad (3-30)$$

This also leads to the following expression from (3-4) for the current on the wire in Region 2:

$$I(z) = -\frac{4}{\eta} \sum_{j=1}^N \alpha_j \int_0^\infty \frac{[A(kU_j\gamma) - A(kV_j\gamma)]}{\gamma(1-\gamma^2)^{\frac{1}{2}} H_0^{(1)}(ka\gamma) H_0^{(2)}(ka\gamma)} e^{-ikz(1-\gamma^2)^{\frac{1}{2}}} d\gamma \quad (3-31)$$

Following the methods used in Appendix B, we rewrite the current as

$$\begin{aligned} I(z) = & -\frac{4}{\eta} \sum_{j=1}^N \alpha_j \left\{ \int_{\arcsin(\delta)}^{\frac{\pi}{2}} \frac{[A(kU_j \sin \theta) - A(kV_j \sin \theta)] e^{-ikz \cos \theta}}{\sin \theta H_0^{(1)}(ka \sin \theta) H_0^{(2)}(ka \sin \theta)} d\theta \right. \\ & + \int_0^\delta \left[\frac{[A(kU_j\gamma) - A(kV_j\gamma)] e^{-ikz(1-\gamma^2)^{\frac{1}{2}}}}{\gamma(1-\gamma^2)^{\frac{1}{2}} H_0^{(1)}(ka\gamma) H_0^{(2)}(ka\gamma)} + \frac{\pi \ln(\frac{U_j}{V_j}) e^{-ikz}}{2\gamma[\frac{\pi^2}{4}(\ln(\frac{ka}{2}) + \Gamma)^2]} \right] d\gamma \\ & - \frac{\pi}{2} \ln\left(\frac{U_j}{V_j}\right) e^{-ikz} \left\{ 1 + \frac{2}{\pi} \arctan \left[\frac{2}{\pi(\ln(\frac{ka\delta}{2}) + \Gamma)} \right] \right\} \\ & + i \int_0^{\frac{\pi}{2}} \frac{[A(kU_j \sec \theta) - A(kV_j \sec \theta)] e^{-kz \tan \theta}}{H_0^{(1)}(ka \sec \theta) H_0^{(2)}(ka \sec \theta)} d\theta \\ & + i \int_2^\infty \left\{ \frac{[A(kU_j\gamma) - A(kV_j\gamma)] e^{-kz(\gamma^2-1)^{\frac{1}{2}}}}{(\gamma^2-1)^{\frac{1}{2}} \gamma H_0^{(1)}(ka\gamma) H_0^{(2)}(ka\gamma)} \right. \\ & \left. + \left[\frac{\sin k(U_j - a)\gamma}{\sqrt{\frac{U_j}{a}} \gamma^2} - \frac{\sin k(V_j - a)\gamma}{\sqrt{\frac{V_j}{a}} \gamma^2} \right] e^{-kz\gamma} \right\} d\gamma - \Phi_2 \left. \right\} \quad (3-32) \end{aligned}$$

where

$$\begin{aligned}\Phi_2 = & \frac{i}{2\sqrt{\frac{U_j}{a}}} \left[e^{-2kz} \sin 2k(U_j - a) - (k(U_j - a) + ikz) E_1(2kz - i2k(U_j - a)) \right. \\ & + (k(U_j - a) - ikz) E_1(2kz + i2k(U_j - a)) \Big] \\ & - \frac{i}{2\sqrt{\frac{V_j}{a}}} \left[e^{-2kz} \sin 2k(V_j - a) - (k(V_j - a) + ikz) E_1(2kz - i2k(V_j - a)) \right. \\ & \left. + (k(V_j - a) - ikz) E_1(2kz + i2k(V_j - a)) \right]\end{aligned}$$

The same problems associated with (3-18) are also present here. We refer the reader to the paragraph below (3-18) for a description of that problem.

3.4 Numerical Results

The ZO approximation does not provide an accurate representation for the aperture electric field. We therefore rely upon the MOM approximation to obtain a solution which accurately models the aperture field. Since our problem is non-selfadjoint, we cannot obtain a solution which is mathematically convergent by any norm minimization method (Dudley, 1985). Instead, numerical results are presented in this section to show the validity of our solution. Results are also presented for the admittance and current where the solutions from the two approximations are compared.

Let us begin by examining the MOM approximation for the aperture field. As an example, consider the case where $ka = 0.1$ and $b/a = 2$. The aperture field is calculated using N equally spaced pulse functions ($\chi = 1$) with $N = 10, 20$, and 40 . Since the aperture size here is much smaller than a wavelength, the solution should

be very close to the quasi-static solution. Figures 3-3 through 3-5 illustrates the magnitude of the calculated aperture fields from the wire ($k\rho = 0.1$) to the screen ($k\rho = 0.2$). The solid lines represent the MOM approximation for various values of N while the dotted line represents the quasi-static solution given by (3-8). The value for C is appropriately chosen to fit the MOM curves at $k\rho = ka$, and the aperture fields are normalized by the factor ρ/I_0 . As the number of pulses increases, our solution behaves more and more like the quasi-static solution, which is indicative of the fact that the MOM solution converges as $z \rightarrow \infty$. Also the edge singularity at $\rho = b$ becomes more apparent as N increases. After careful examination of the plots for the aperture field, we notice that even for the case where N is large (such as $N = 40$) there are still differences between the solution obtained by MOM and the quasi-static solution. This is due to errors in the quasi-static solution. Although our quasi-static solution accounts for the edge singularity, it is too inflexible to accurately model the aperture field solution.

Extensive work in electromagnetics has been done using the same expansion and weighting functions which we have chosen, but almost all of it has been done with equally spaced pulse functions. Because of the presence of an edge singularity in our problem, aperture field calculations utilizing nonuniform pulse expansion functions are preferable. Let us compare the nonuniform case (Figure 3-6) of $\chi = 0.6$ and $N = 8$ to the uniform cases (Figures 3-3 through 3-5). It is apparent from these plots that even with five times the number of pulse function, the curve obtained from uniform spacing is less accurate than that from nonuniform spacing in this example. This is true for aperture sizes less than a wavelength. As the aperture size approaches or exceeds a wavelength, a more nearly uniform pulse spacing becomes

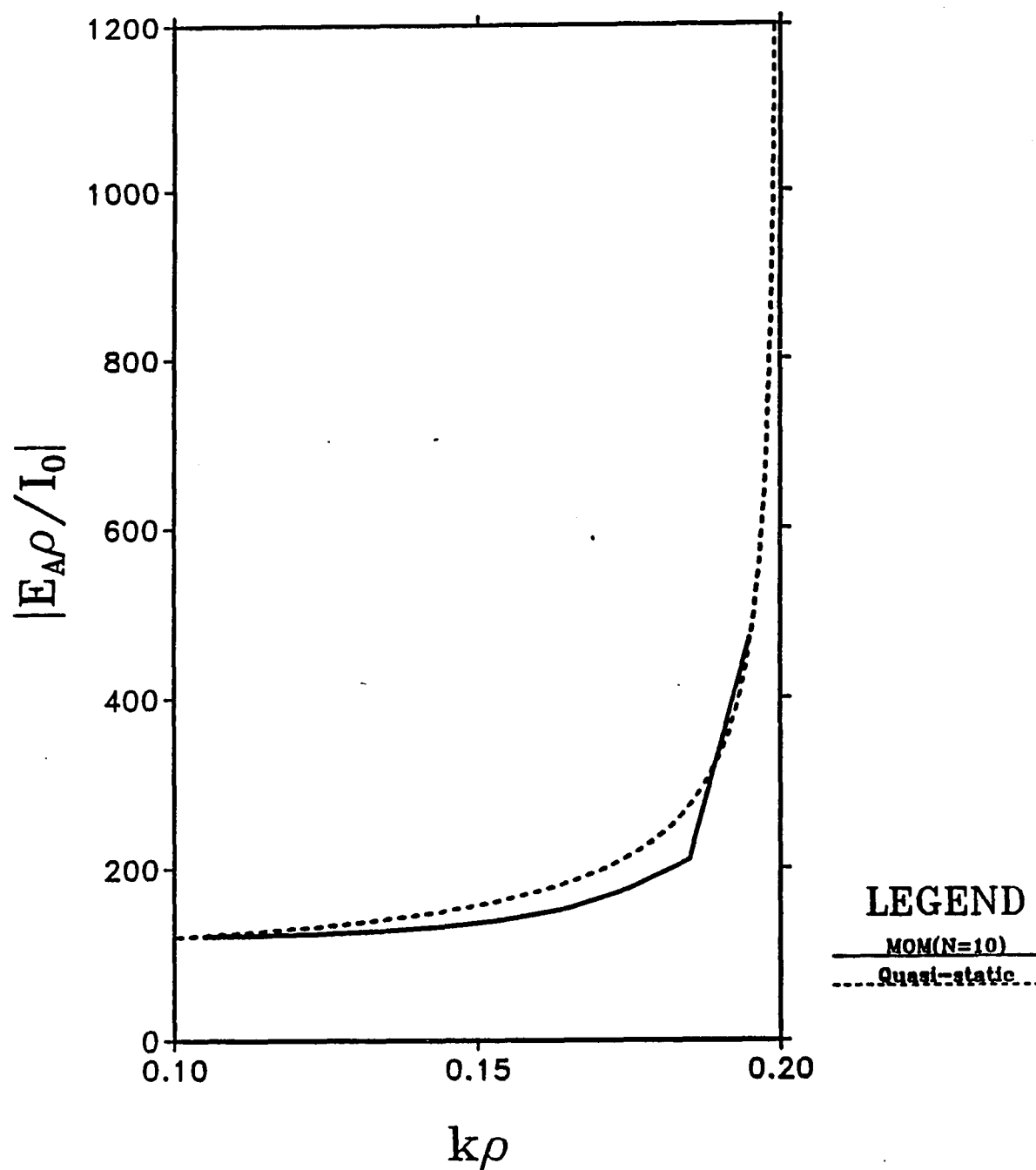


Figure 3-3 Diagram comparing the quasi-static solution for the magnitude of the normalized aperture electric field to the MOM solution with $N = 10$ and $\chi = 1$.

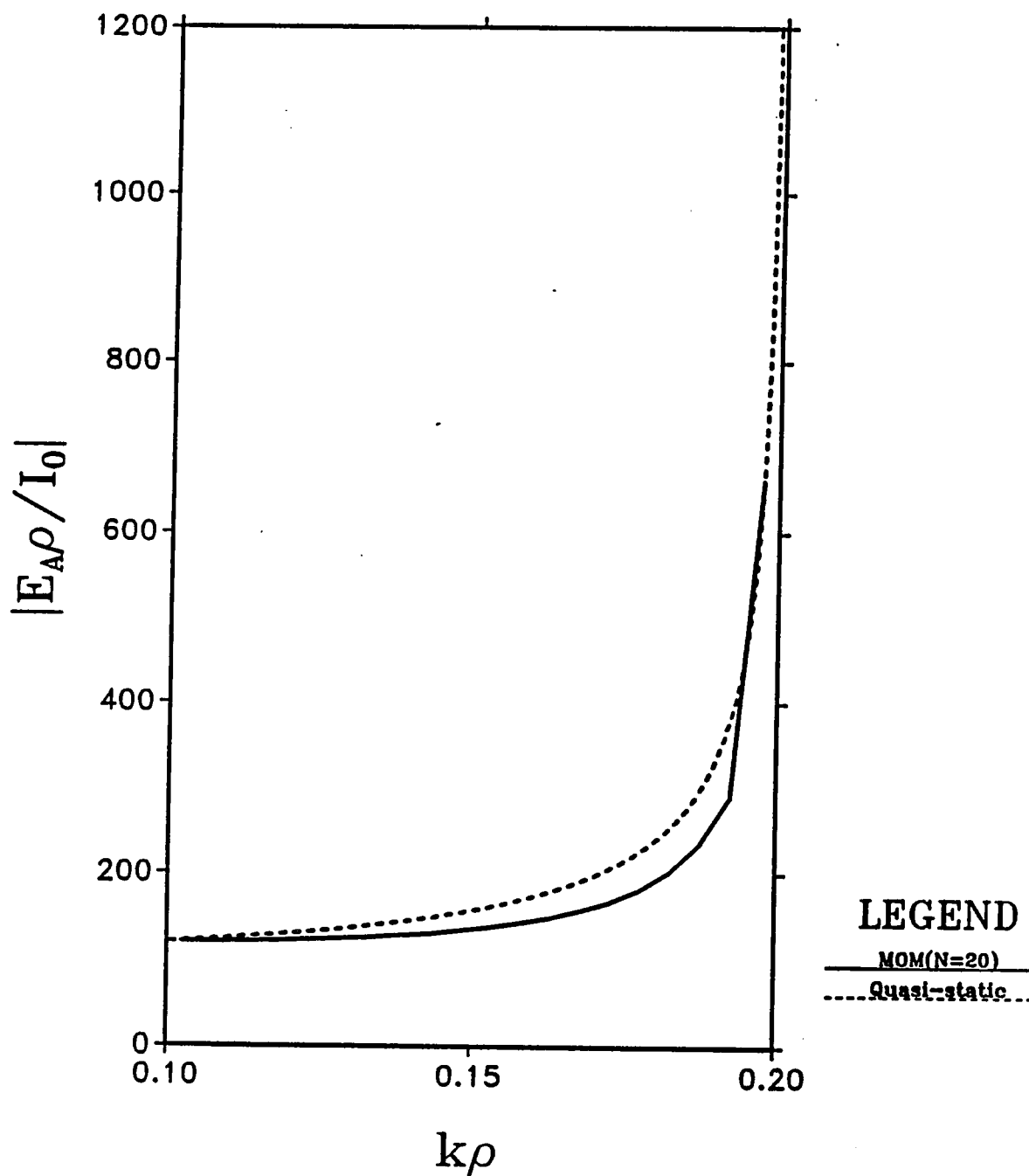


Figure 3-4 Diagram comparing the quasi-static solution for the magnitude of the normalized aperture electric field to the MOM solution with $N = 20$ and $\chi = 1$.

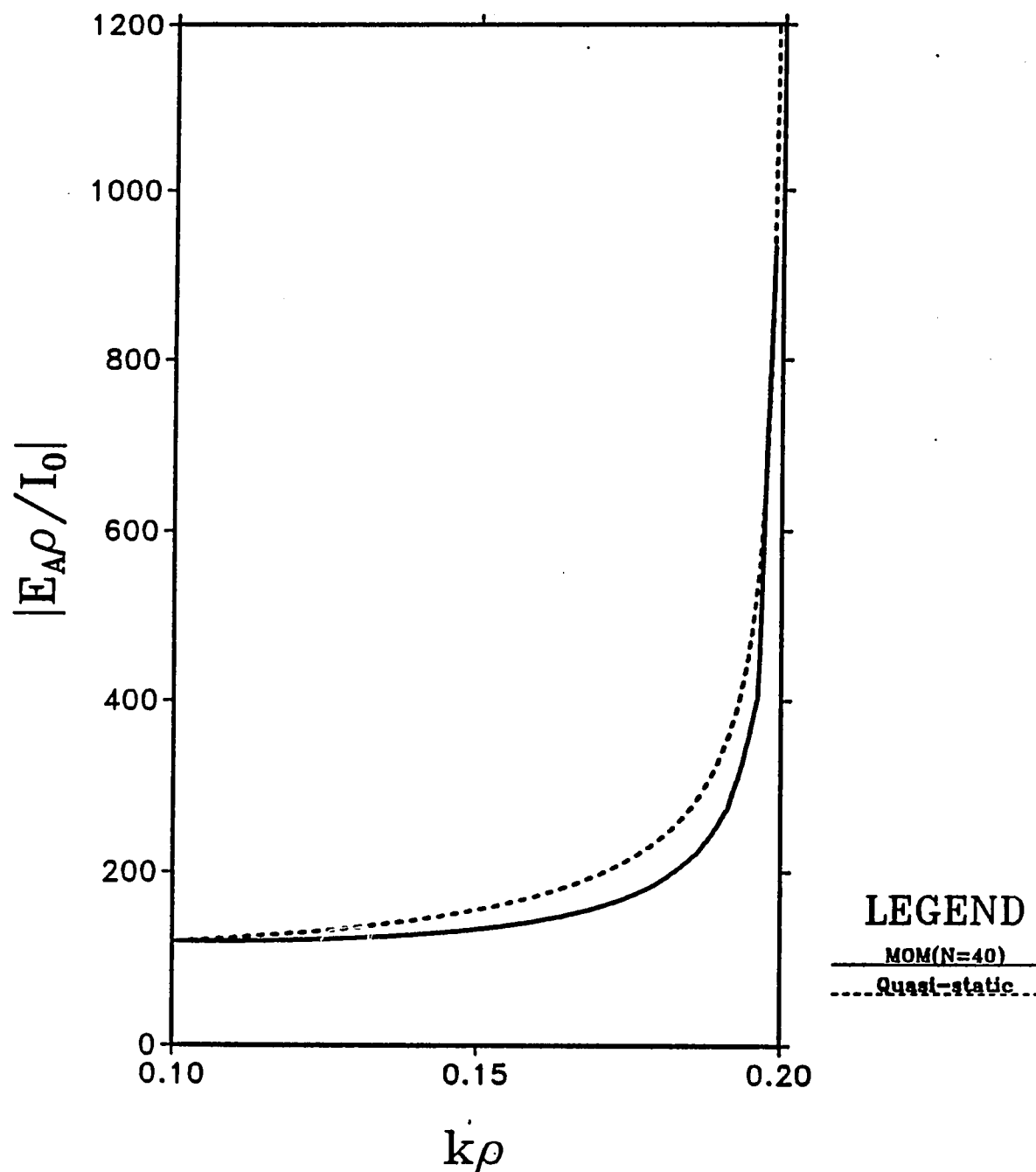


Figure 3-5 Diagram comparing the quasi-static solution for the magnitude of the normalized aperture electric field to the MOM solution with $N = 40$ and $\chi = 1$.

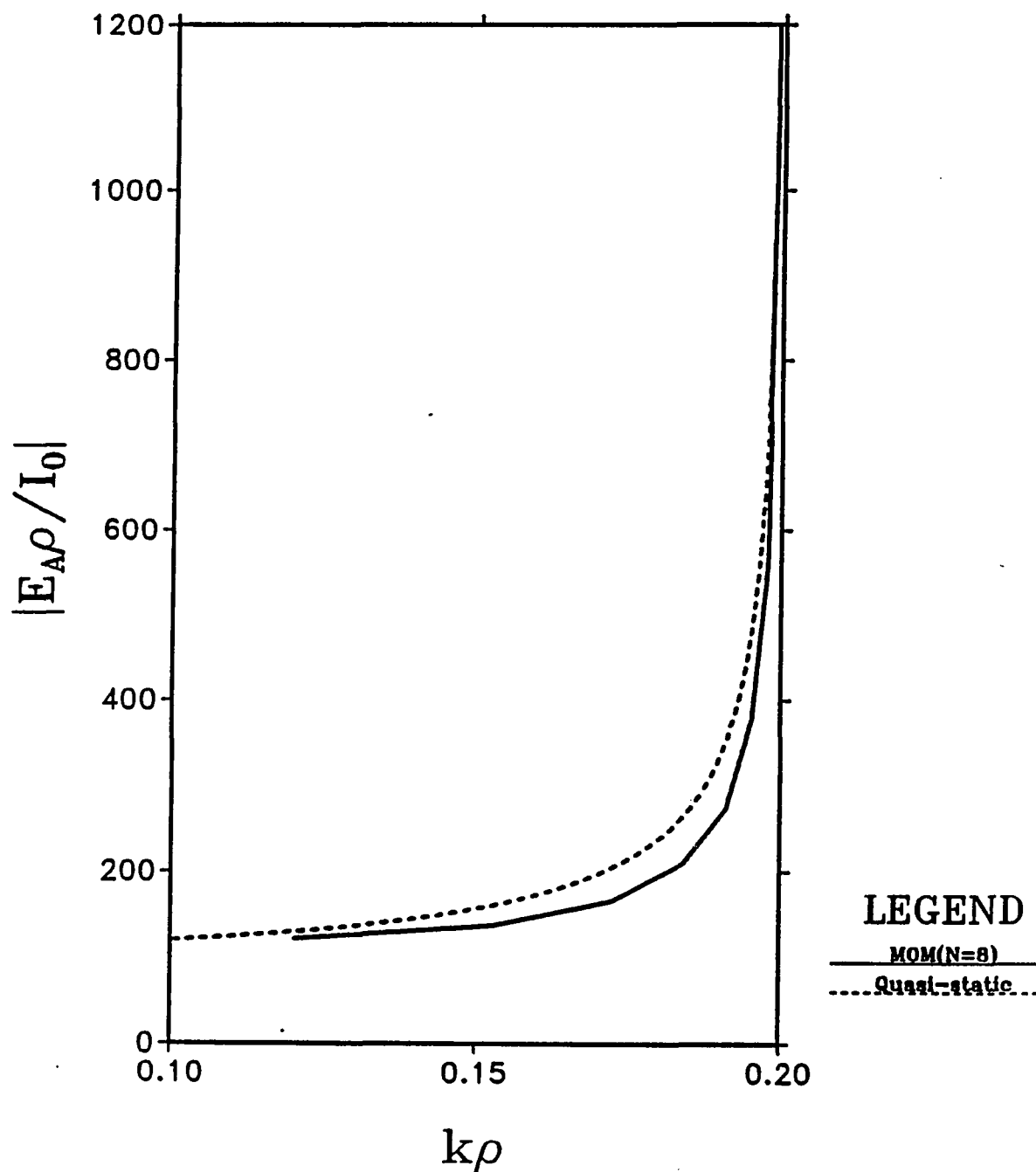


Figure 3-6 Diagram comparing the quasi-static solution for the magnitude of the normalized aperture electric field to the MOM solution with $N = 8$ and $\chi = 0.6$.

desirable. This is due to the fact that the fluctuation in the aperture field away from the edge singularity increases as $k(b - a)$ increases; therefore, the value of χ approached unity for large apertures, and N must increase accordingly to maintain accuracy.

Although we need the MOM approximation to obtain an accurate solution for the aperture field, the ZO order approximation may be useful in calculating a solution for the admittance and current on the wire. It would be advantageous to use this approximation since its solution takes only a fraction of the computational time that the MOM solution requires. Unfortunately, the ZO approximation is not valid at all frequencies; therefore, we must determine the frequency below which this approximation is valid. In calculating the admittances and current using MOM, eight pulse expansion functions with $\chi = 0.6$ were used to represent the aperture field for all cases except $b/a = 5.0$. Because of the large aperture size in that case, twelve pulse expansion functions were used with χ increasing from 0.7 to 0.9 as frequency increases.

Figures 3-7 and 3-8 compares the conductance and susceptance, respectively, resulting from the two approximations. The values are normalized by the constant $\eta/4\pi$ and plotted versus ka with ka ranging from 0.01 to 1.0. Three aperture sizes are considered, namely, $b/a = 1.05$, 2.0, and 5.0. In studying the plots of the admittance, we see that the difference between the two solutions increases as the electrical size of the aperture increases. Similarly, we can compare the current on the wire arising from the two approximations. Figures 3-9 through 3-11 show results for the magnitude of the current at observation points on the wire located at $z = 0$, a , and $100a$. Observation locations greater than $z/a = 100$ are not considered

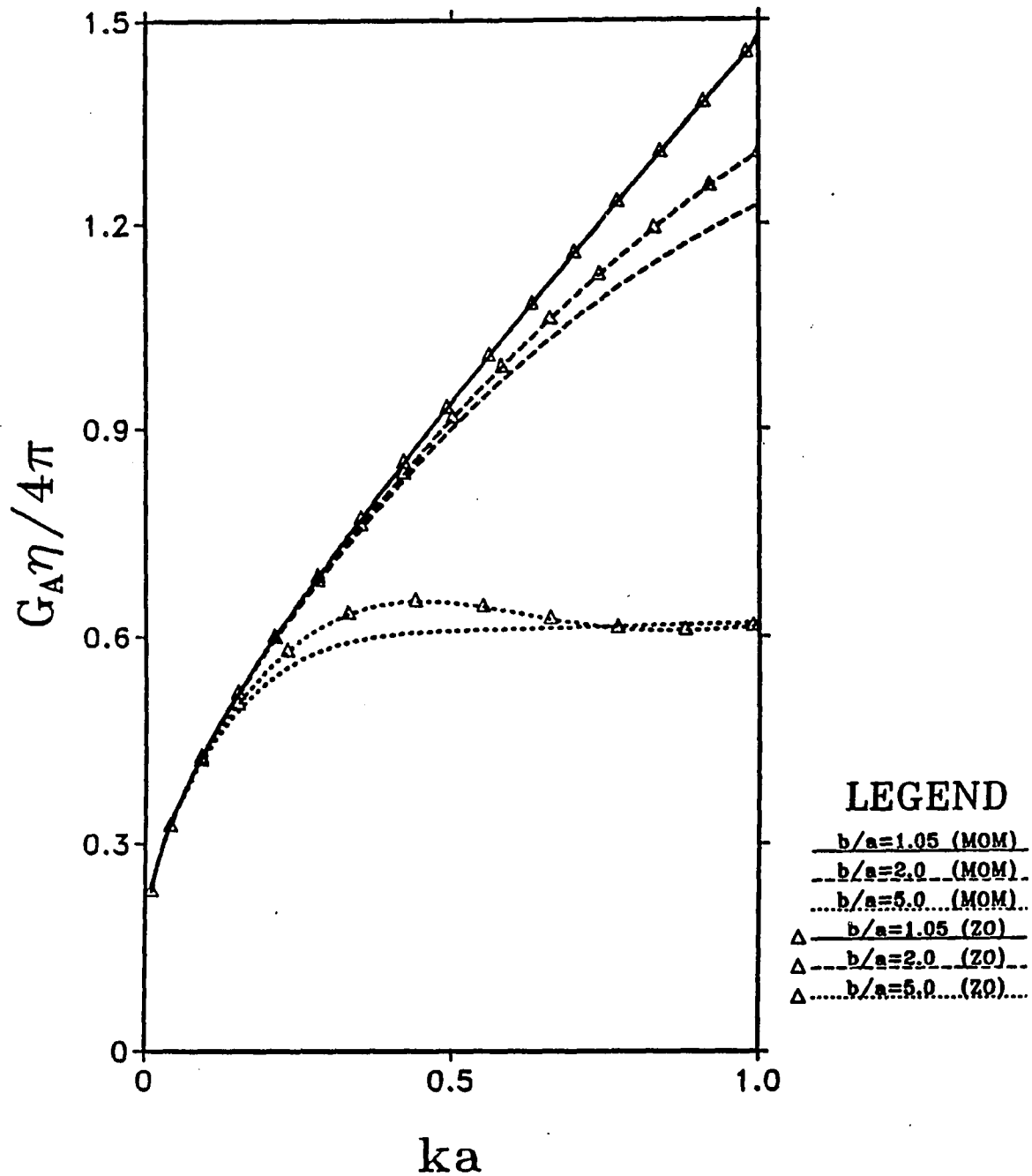


Figure 3-7 Diagram comparing the ZO solution to the MOM solution for the normalized conductance as a function of ka .

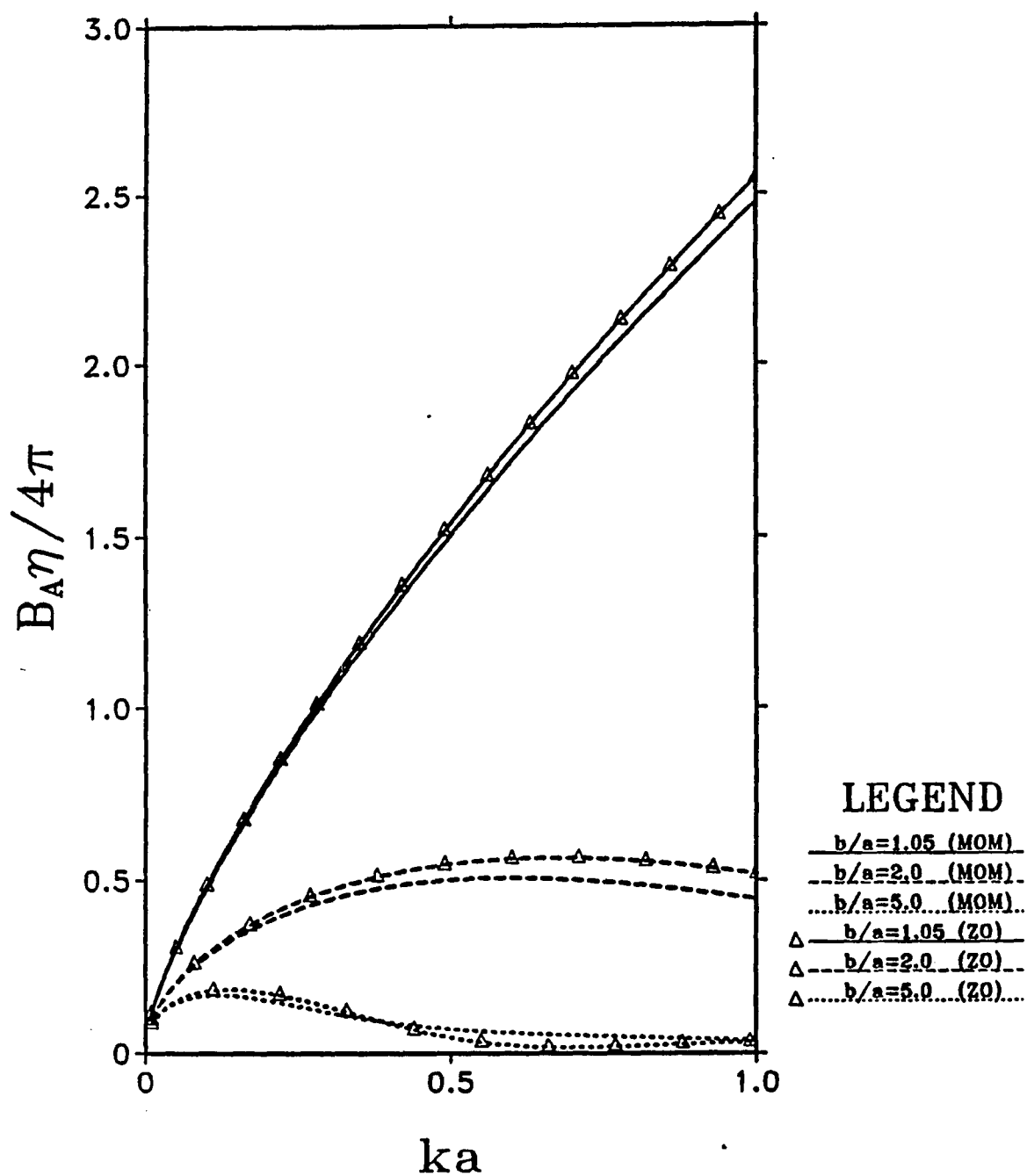


Figure 3-8 Diagram comparing the ZO solution to the MOM solution for the normalized susceptance as a function of ka .

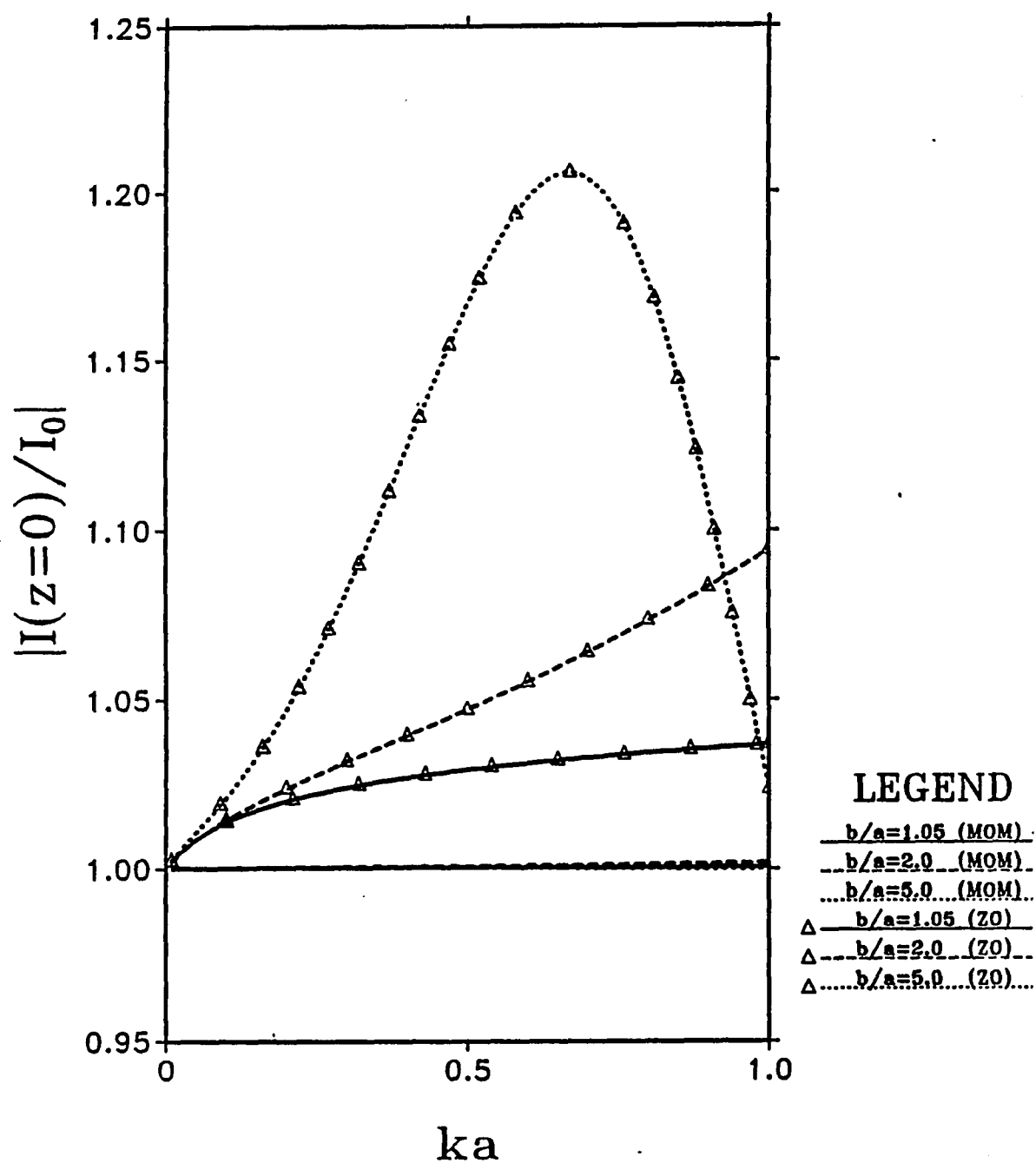


Figure 3-9 Diagram comparing the ZO solution to the MOM solution for the magnitude of the normalized current at $z/a = 0$.

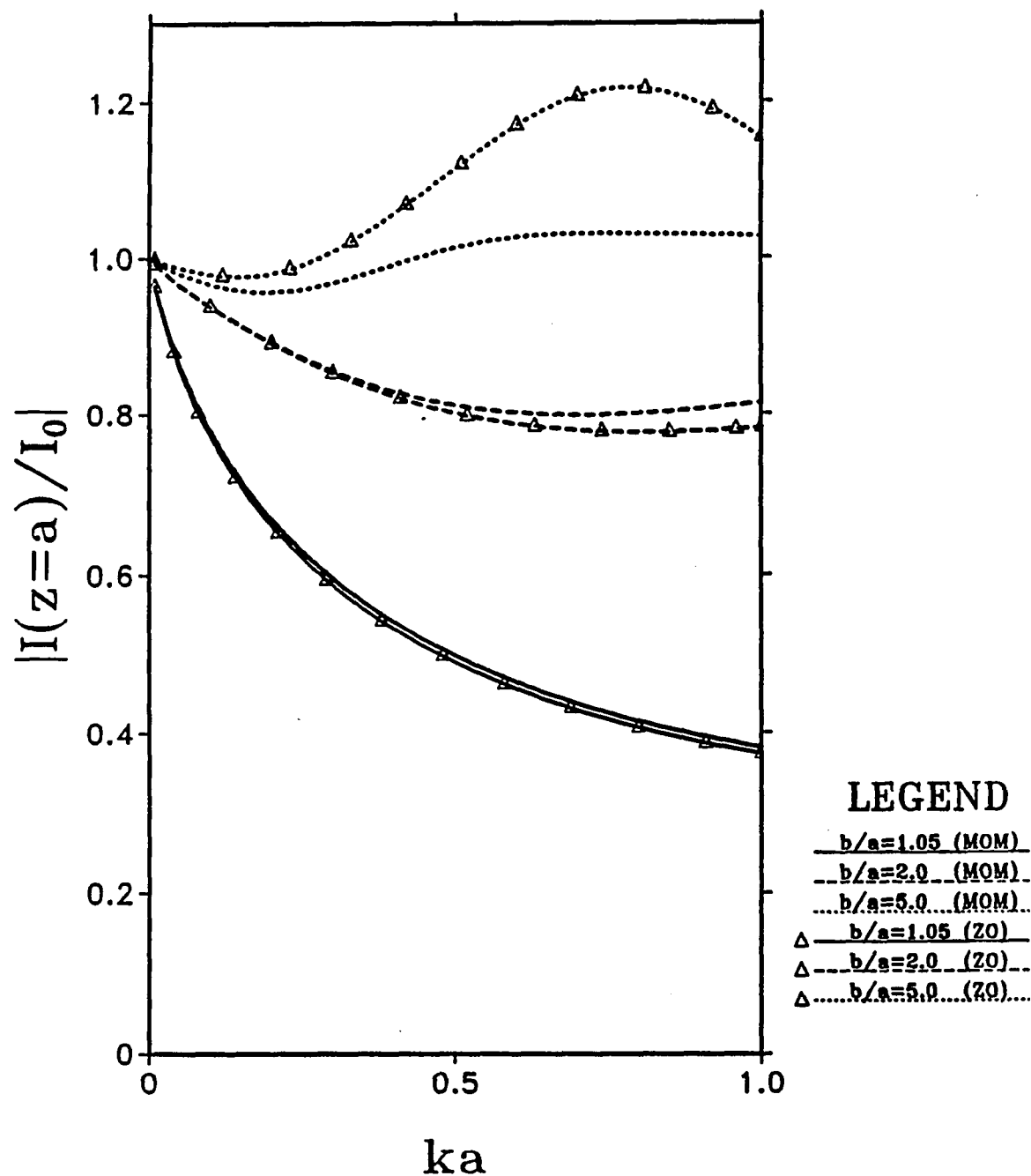


Figure 3-10 Diagram comparing the ZO solution to the MOM solution for the magnitude of the normalized current at $z/a = 1$.

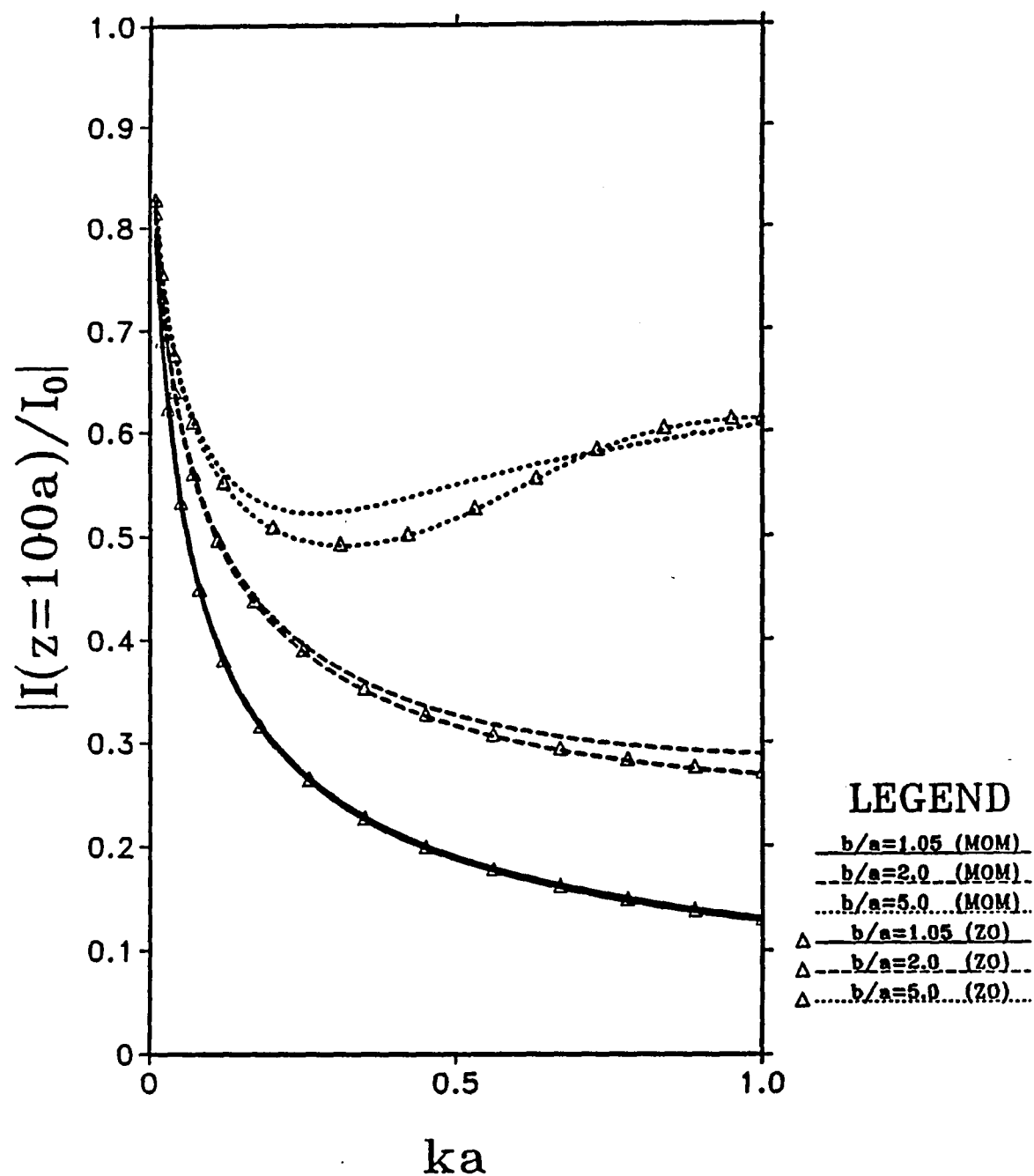


Figure 3-11 Diagram comparing the ZO solution to the MOM solution for the magnitude of the normalized current at $z/a = 100$.

because of the numerical difficulties associated with large values of kz . The currents are normalized by the factor $|I_0|$, and the same three apertures which we used in the admittance plot are considered. We again see the trend whereby the difference between the two solutions increase as the electrical aperture size increases. In Figure 3-9, we consider the current at the aperture. This case is especially interesting in that we know the exact solution at that point. The MOM results for the three aperture sizes show almost no error while the ZO results show large deviations from the exact answer. This further reinforces our confidence in the validity of the MOM solution.

Overall, the agreement between the two methods is very good for the frequency range and aperture sizes considered. The numerical results support the claim that the ZO approximation is valid for aperture sizes smaller than $1/10$ of a wavelength. Also, for aperture sizes up to a half a wavelength the solution using the ZO approximation is well within an order of magnitude of the solution using the MOM approximation. We are now able to obtain accurate results using the ZO approximation within its range of validity without the computational time required by the method of moments.

To insure the accuracy of our solutions, we now present results which are determined exclusively from the MOM approximation. Figures 3-12 and 3-13 present results for the admittance with an expanded set of aperture sizes from the previous admittance plots. Let us consider the conductance first. From the plot (3-12), we observe that the conductance increases as ka increases. We also note that the conductance decreases as the ratio b/a increases. We can justify these observations

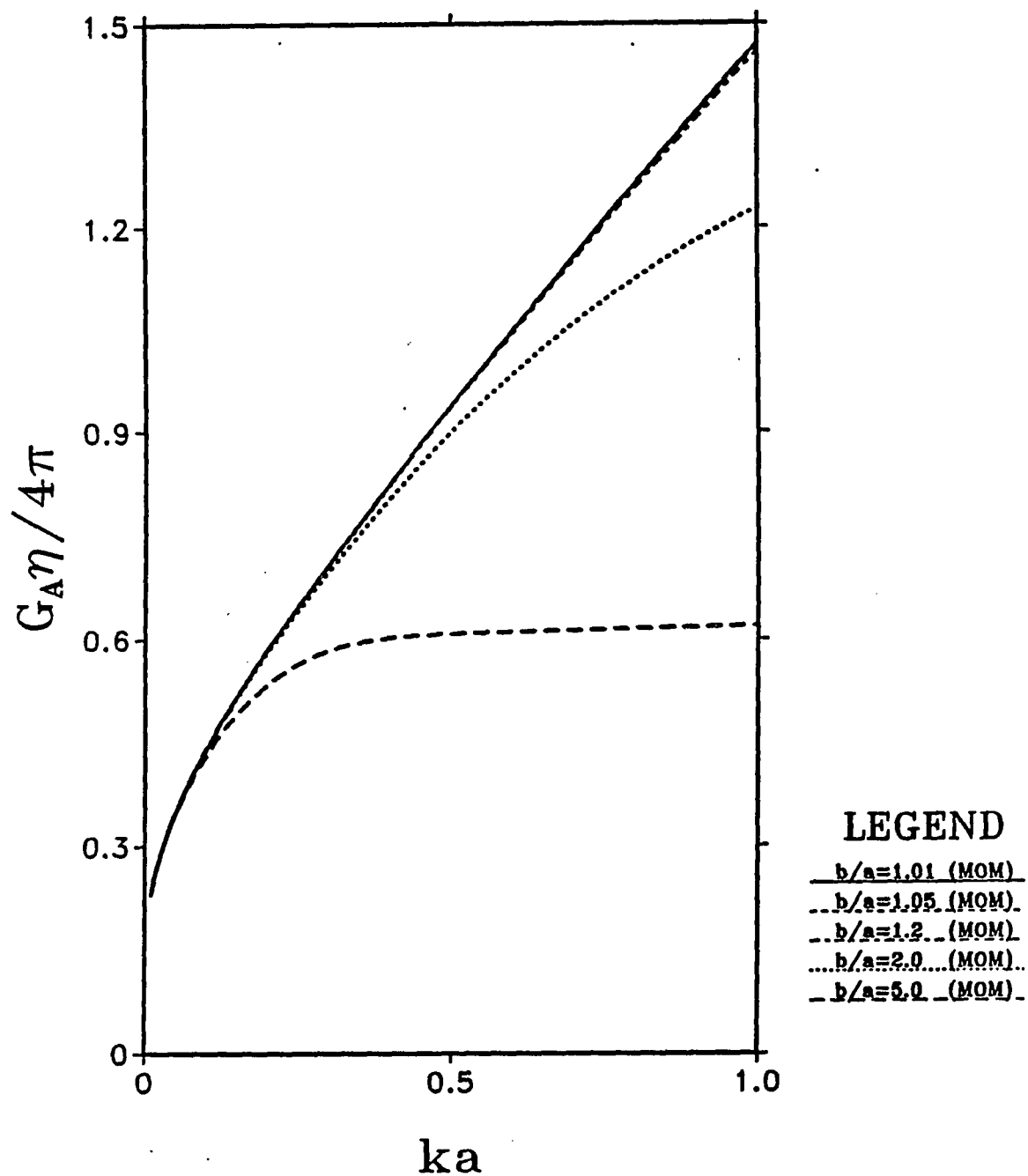


Figure 3-12 The MOM solution of the normalized conductance for five aperture sizes.

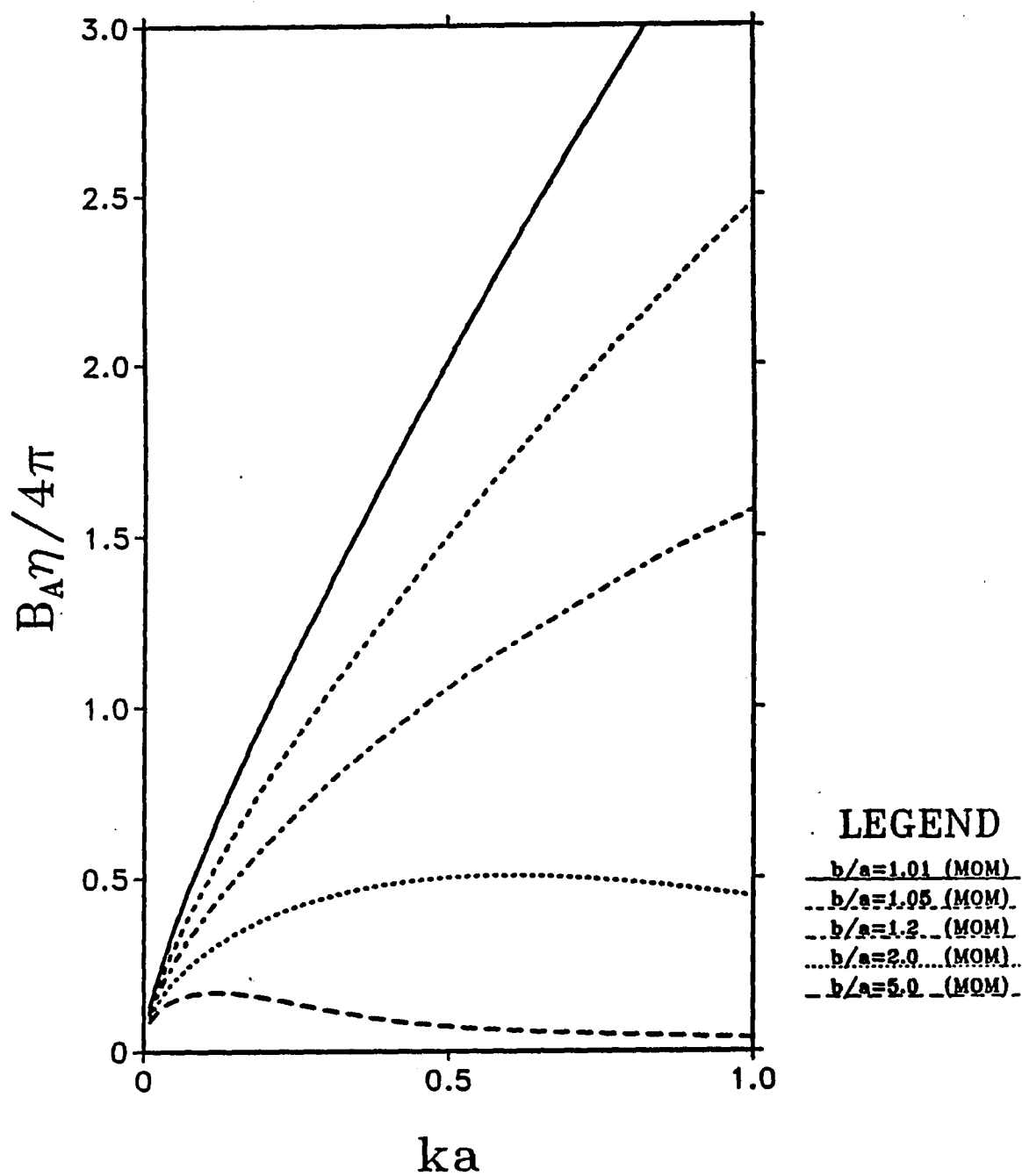


Figure 3-13 The MOM solution of the normalized susceptance for five aperture sizes.

by considering the physical effect of the screen upon the *TEM* mode propagating down the wire. In the absence of the screen, the idealized current source M_ϕ generates only the *TEM* mode which does not radiate any energy from the wire. With the screen in place, mode conversion results in the radiation of energy. The conductance is a measure of the amount of energy radiated from the wire. As the conductance increases, the radiated energy increases. The resulting modal behavior cannot be considered *TEM* anymore, but rather must be thought of as quasi-*TEM* since most of the modal content of the field is close to *TEM*. For large aperture sizes, the quasi-*TEM* behavior dominates since there is very little mode conversion. This can be seen by looking at the conductance curve for $b/a = 5$ where the conductance is significantly less than for the case of $b/a \leq 1.2$. As the aperture size decreases, the quasi-*TEM* behavior is less dominant due to greater mode conversion into the radiating modes. This results in greater radiation losses along the wire, hence a larger conductance. The frequency dependence of the conductance can also be explained by the fact that greater mode conversion occurs at higher frequencies. It is interesting to note that for larger values of b/a , the *slope* of the conductance curves decreases with frequency, and in the case of $b/a = 5$, the conductance curve actually levels out. This indicates that for very large aperture sizes, the conductance is independent of frequency. This is due to the fact that for large aperture sizes the modal behavior is nearly *TEM*.

The susceptance is dependent upon the capacitive coupling which occurs between the wire and the screen. As the aperture size increases, one would expect the capacitive coupling to decrease. This is shown by our curves (Figure 3-13) where we see that the susceptance values vary inversely with the aperture size. By

consulting basic circuit theory we would expect the susceptance to increase linearly with frequency for a fixed aperture size since

$$B_A = \omega C_A \quad (3 - 33)$$

where C_A is the capacitance between the wire and the screen. The susceptance curves do increase as a function of frequency, but they are not linear. This is due to the fact that the aperture capacitance is not the only contributor to the susceptance. It just happens to be the major one. It would be impossible to account for all the parasitic capacitances and inductances. We will therefore think of the susceptance as a frequency dependent capacitive element without quantifying the element's exact value.

Let us now consider the current on the wire. We expand upon the number of curves in the previous current plots from three to five to present more aperture sizes. Figures 3-14 through 3-16 show plots of the magnitude of the current normalized by $|J_0|$ as a function of ka . Three observation points, located at $z = a$, $5a$, and $100a$, are chosen on the wire. Notice that at a fixed frequency the current decreases as the aperture size decreases. This is due to two separate factors. The first factor is that as the aperture radius decreases there is more mode conversion away from quasi-*TEM* which results in greater radiation loss. This, in turn, attenuates the current as it propagates down the wire. The second factor is that the capacitive coupling between the wire and the screen increases as the aperture size decreases. This causes a larger reflection of the incident current upon the screen which decreases the current which penetrates the screen. The current also slowly decreases as frequency increases, thereby allowing lower frequency waves to penetrate the screen more easily.

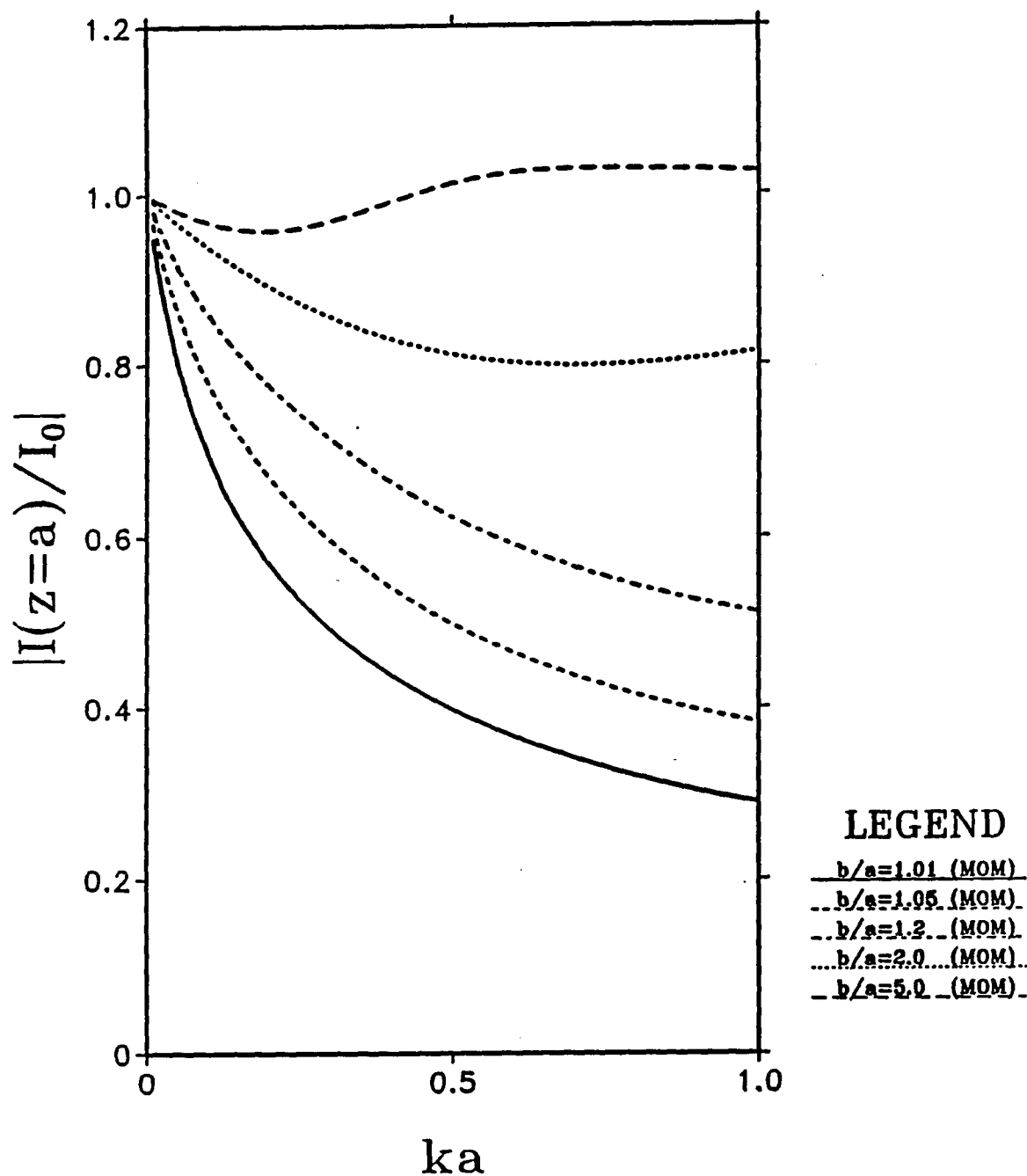


Figure 3-14 The MOM solution of the magnitude of the normalized current at $z/a = 1$ as a function of ka for five aperture sizes.

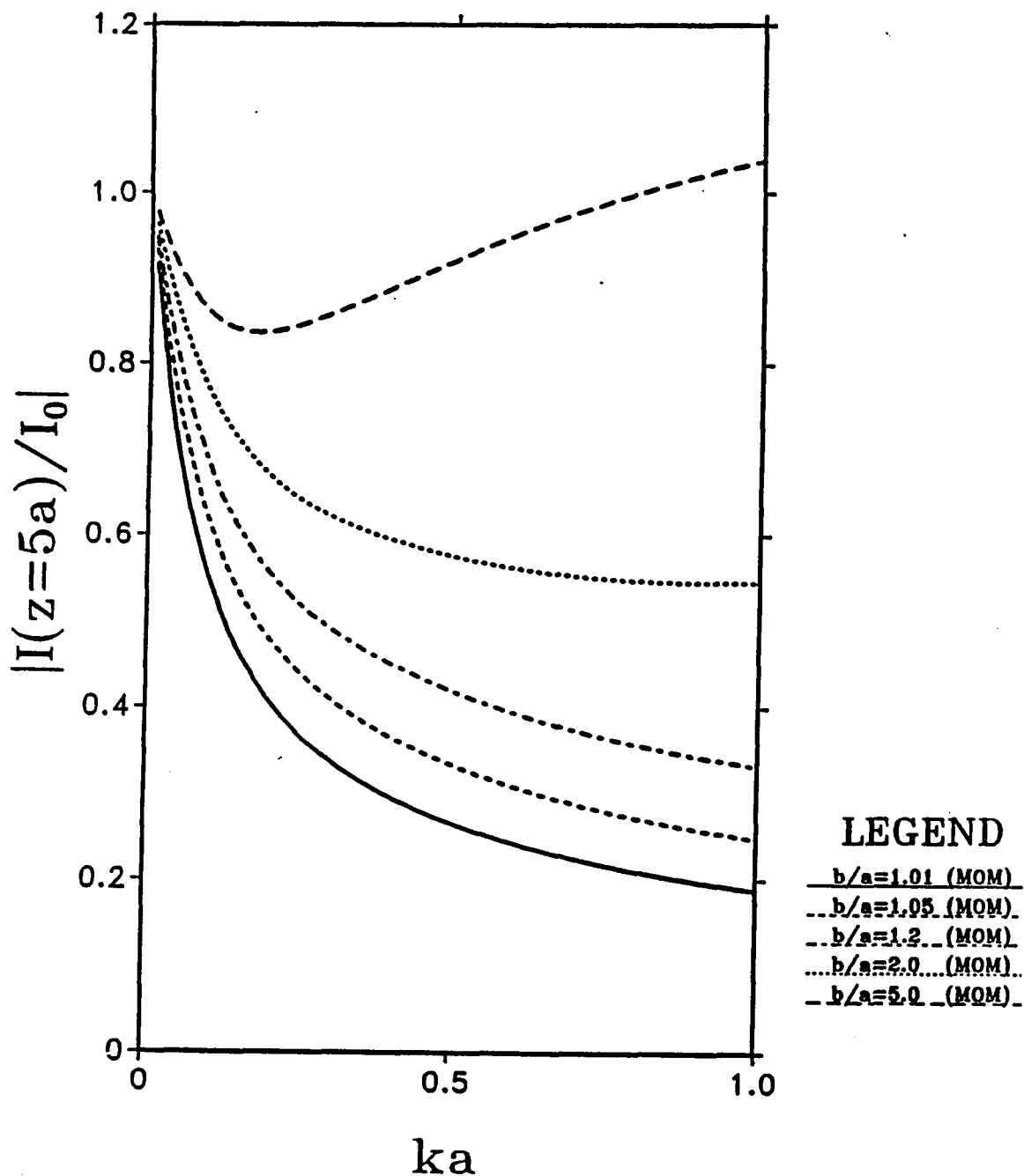


Figure 3-15 The MOM solution of the magnitude of the normalized current at $z/a = 5$ as a function of ka for five aperture sizes.

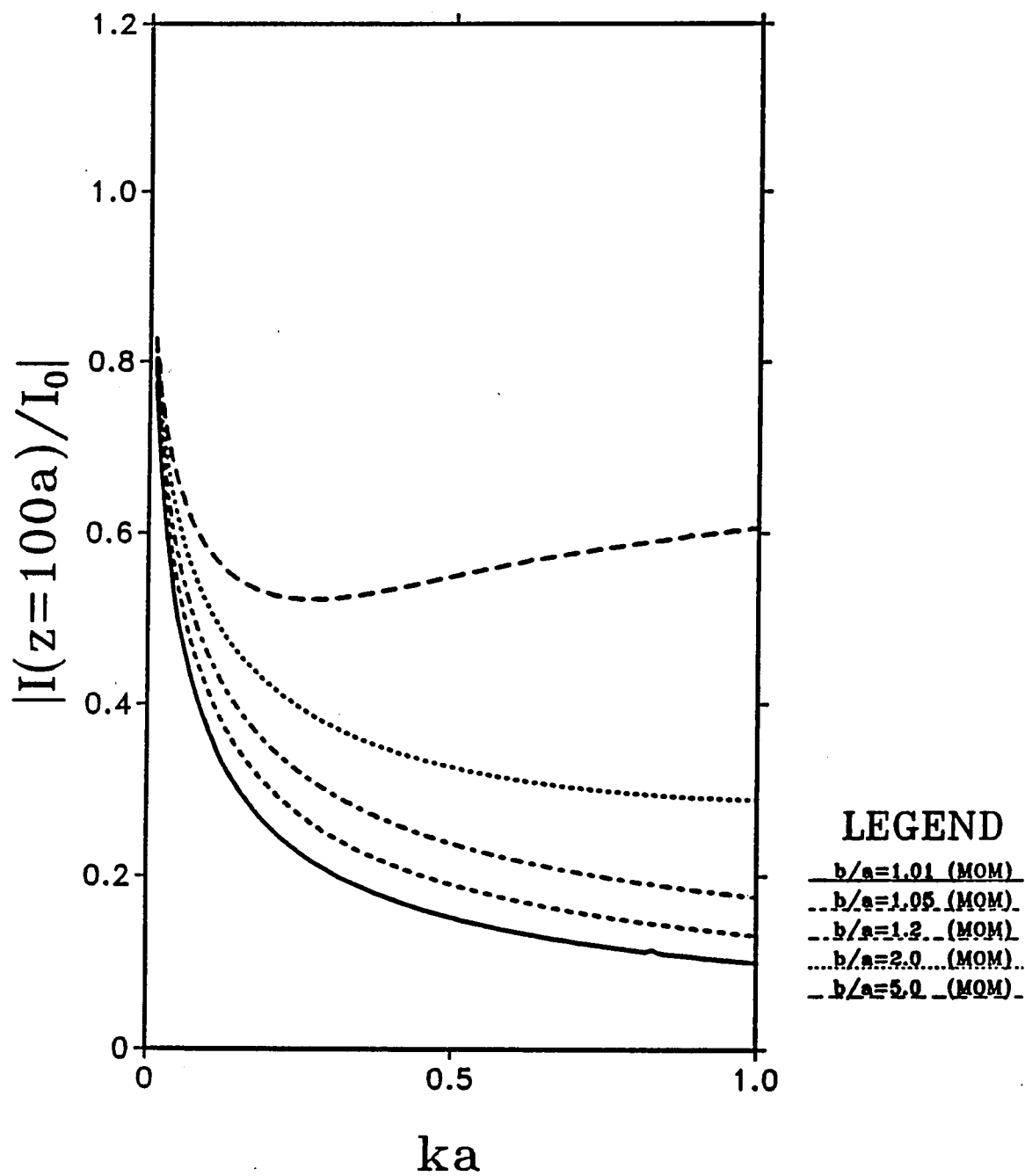


Figure 3-16 the MOM solution of the magnitude of the normalized current at $z/a = 100$ as a function of ka for five aperture sizes.

It is interesting to note that the decrease in current with frequency is monotonic in all cases except $b/a = 5$. This phenomenon is related to the electrical size of the aperture. For $k(b-a) \approx 2.0$ or higher, an enhancement in the current occurs a short distance down the wire. As $k(b-a)$ increase, the enhancement increases. A better picture of this can be seen in Figures 3-17 through 3-19. In these figures, the magnitude of the current normalized by $|I_0|$ is plotted as a function of z/a for four values of ka and three aperture sizes. For values of $k(b-a) < 2.0$, the current decreases monotonically as the observation point moves down the wire. This is expected since energy is radiated from the wire as the current propagates down the wire. On the other hand, we see that there is an initial enhancement in the current for larger values of $k(b-a)$. It is suspected that the resonance of the aperture causes this current enhancement since current enhancement occurs as the frequency approaches resonance.

We observe from Figures 3-17 through 3-19 that the current drops off significantly faster as the size of the aperture decreases. This agrees with our notion about greater mode conversion for smaller apertures. Unfortunately, even for small apertures the current decays very slowly as it propagates down the wire. This indicates that the behavior of the current is still quasi-TEM, and it further illustrates the ineffectiveness of the screen in stopping current penetration on the wire.

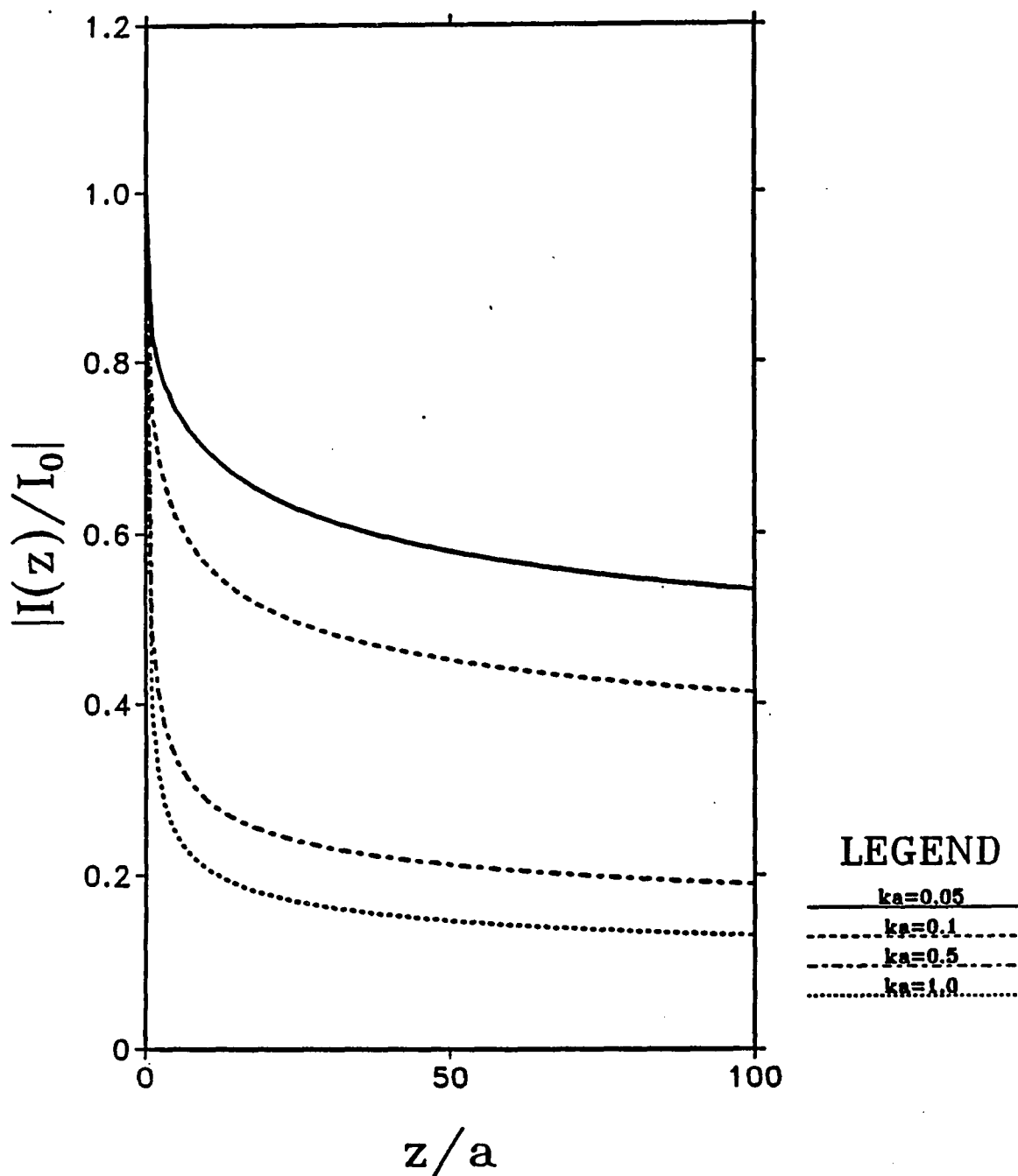


Figure 3-17 The MOM solution of the magnitude of the normalized current as a function of z/a for $b/a = 1.05$ at four values of ka .

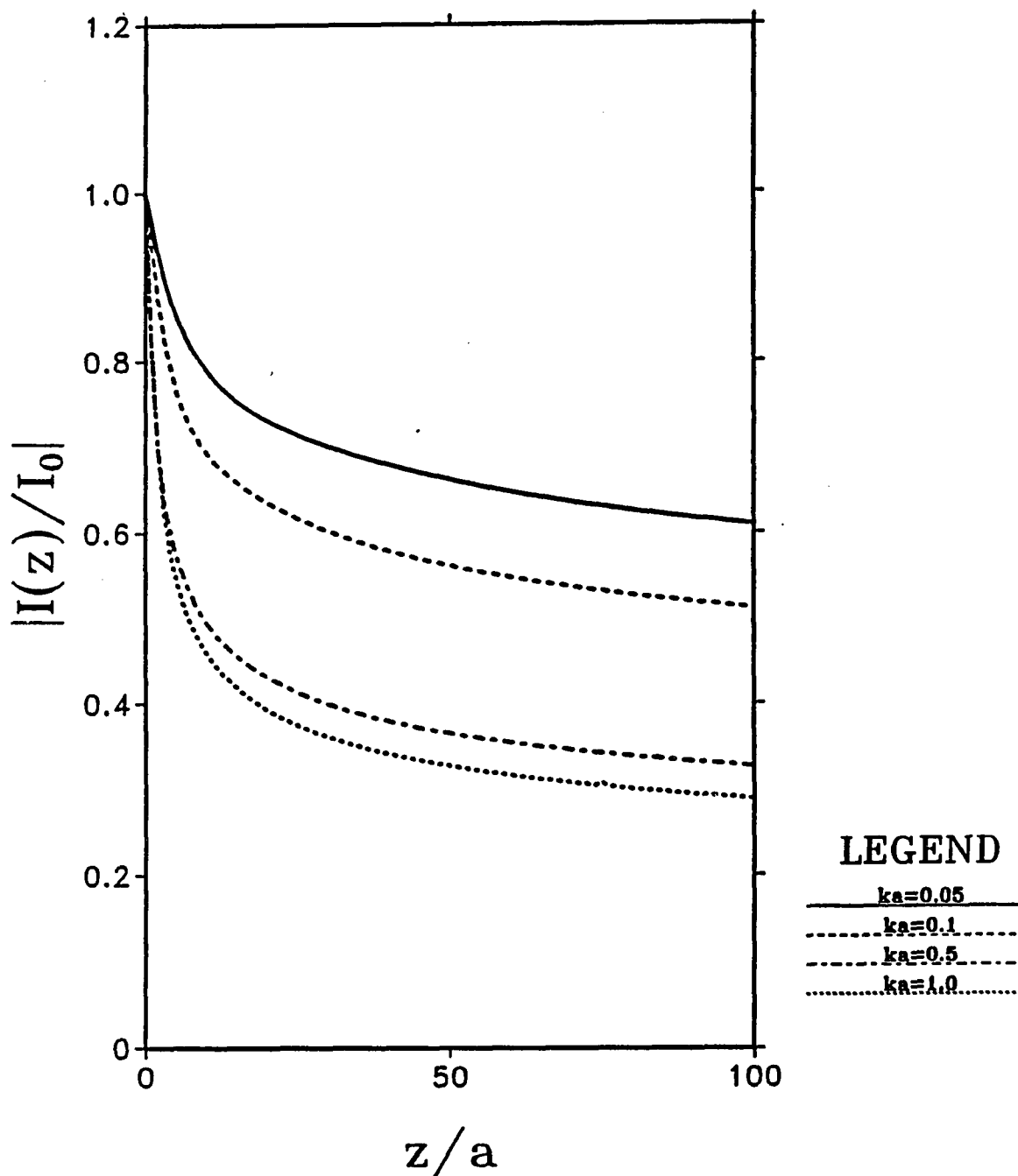


Figure 3-18 The MOM solution of the magnitude of the normalized current as a function of z/a for $b/a = 2$ at four values of ka .

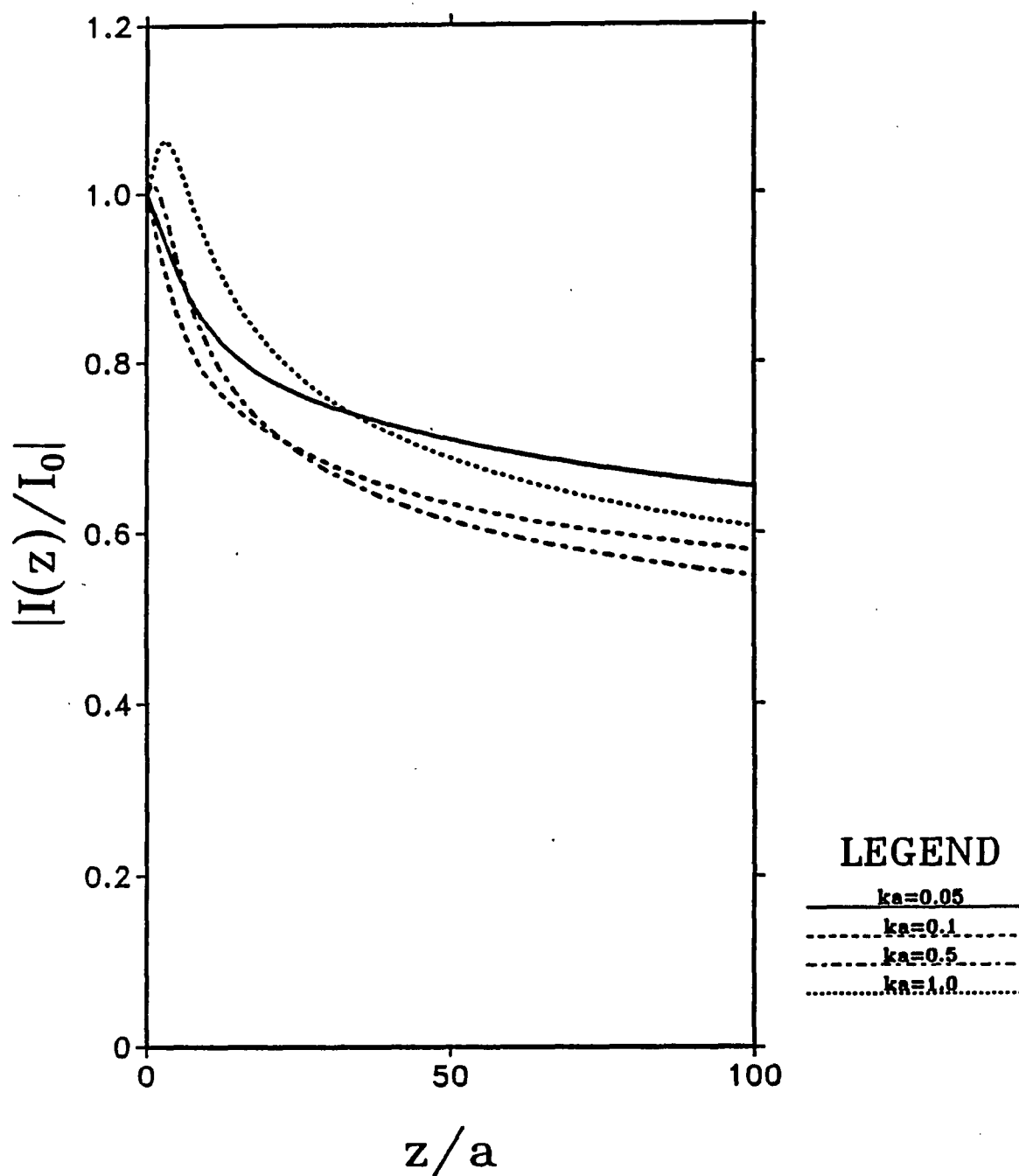


Figure 3-19 The MOM solution of the magnitude of the normalized current as a function of z/a for $b/a = 5$ at four values of ka .

3.5 Transient Analysis

Let us consider the problem of current penetration into Region 2 due to a transient pulse from Region 1. This requires that we obtain a solution for the current in the time domain. Since we already have a means of solving for the current in the frequency domain, We use the inverse Fourier transform to calculate the time domain current from the frequency domain data. We first obtain expressions for both the current and the transient pulse in the frequency domain. We next multiply the current and input pulse spectra and take the inverse Fourier transform to obtain our time domain solution. We use an inverse fast Fourier transform (IFFT) routine from a signal processing package called SIG (Lager and Azevedo, 1985).

3.5.1 Transient Pulse

The transient pulse that we have chosen is the double exponential pulse. The time domain expression for this pulse is given by

$$f(t) = A_0(e^{-\alpha t} - e^{-\beta t})u(t) \quad (3 - 34)$$

where $u(t)$ is the unit step function and A_0 is a normalization constant whose value is such that the maximum of $f(t)$ is 1. The expression for A_0 is

$$A_0 = \frac{1}{e^{-\alpha t_0} - e^{-\beta t_0}} \quad (3 - 35)$$

where $t_0 = \ln(\beta/\alpha)/(\beta - \alpha)$. We now take the Fourier transform of $f(t)$ to get its frequency spectrum,

$$F(f) = A_0 \left[\frac{1}{\alpha + i2\pi f} - \frac{1}{\beta + i2\pi f} \right] \quad (3 - 36)$$

The values of α and β determine the shape and frequency spectrum of the transient pulse. We will consider two cases. In the first case (Figure 3-20), we choose $\alpha = 1 \times 10^7$ and $\beta = 1 \times 10^8$. This gives us a pulse whose frequency spectrum drops approximately 50 dB as the frequency goes from DC to 100 MHz. For the second case (Figure 3-21), we choose $\alpha = 2 \times 10^9$ and $\beta = 3 \times 10^9$. In this case the frequency spectrum drops 50 dB over a frequency range of 7 GHz. Because the frequency content for this case is much higher relative to the previous case, we refer to this pulse as the high frequency pulse and the previous case as the low frequency pulse. Also, we note that the rise and fall times of the pulse decrease as the values of α and β increase, respectively.

The IFFT routine that we use requires that the frequency spectrum of the input signal be nonzero over a finite range of frequencies. We must therefore truncate the frequency spectrum of the pulse at a finite frequency point. Because of this truncation, errors result in our time domain solution. To obtain an indication of the amount of error which occurs due to the truncation, we truncate the frequency spectrum of the input signal and perform an inverse Fourier transform on it to obtain a time domain solution. For the low frequency pulse we truncate the spectrum at $f = 255$ MHz. Similarly, we truncate the spectrum at $f = 8.0$ GHz for the high frequency pulse. The time domain solutions are given in Figure 3-22. The errors are unnoticeable on the plots. Thus, we expect any errors in the time domain current solution to be small.

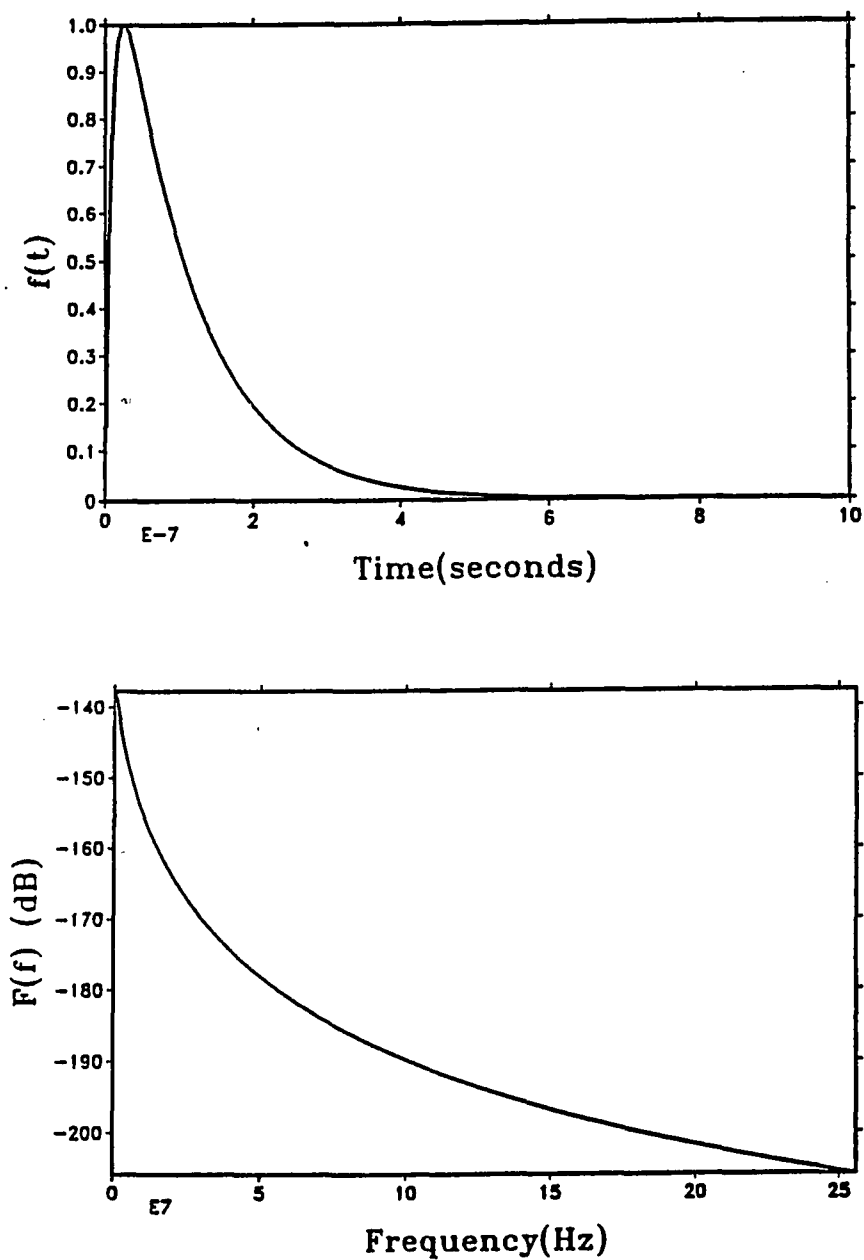


Figure 3-20 Plot of the low frequency, double exponential pulse ($\alpha = 1 \times 10^7$, $\beta = 1 \times 10^8$) in both the time and frequency domain.

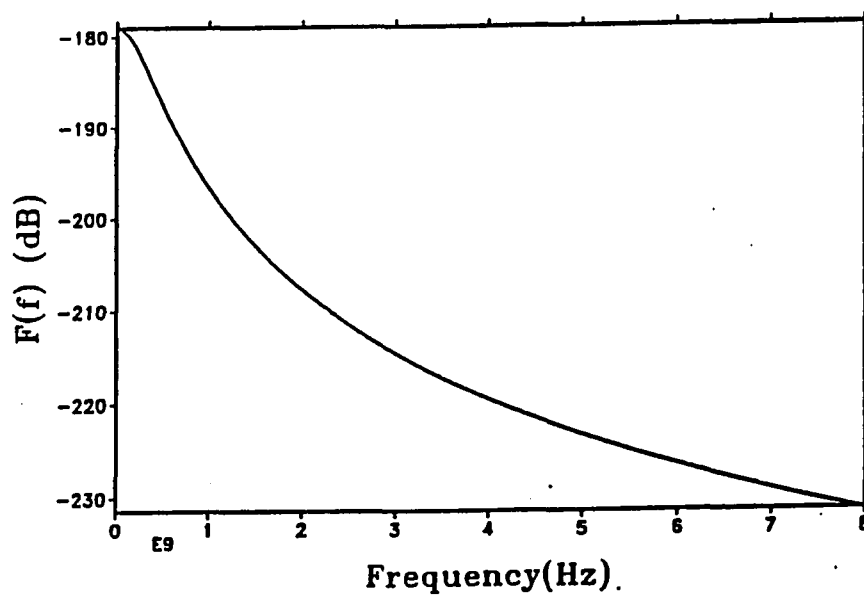
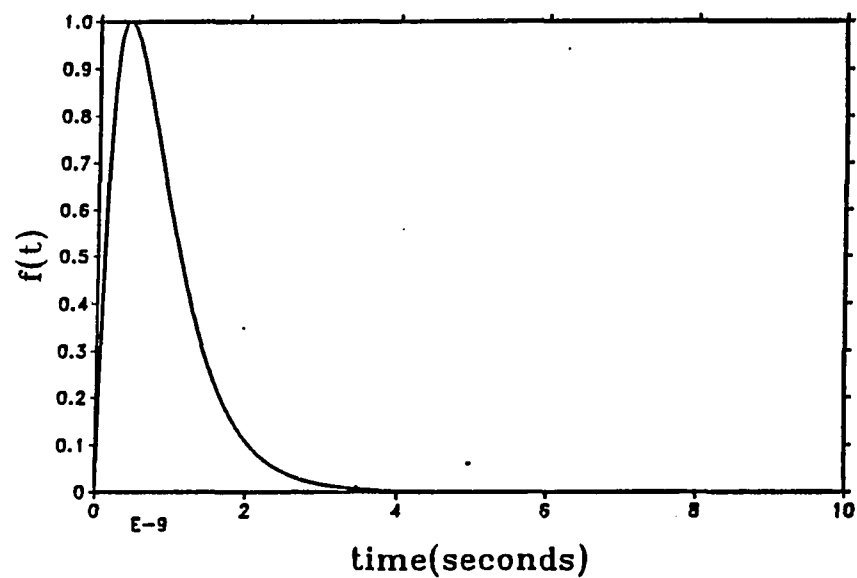


Figure 3-21 Plot of the high frequency, double exponential pulse ($\alpha = 2 \times 10^9$, $\beta = 3 \times 10^9$) plotted in both the time and frequency domain.

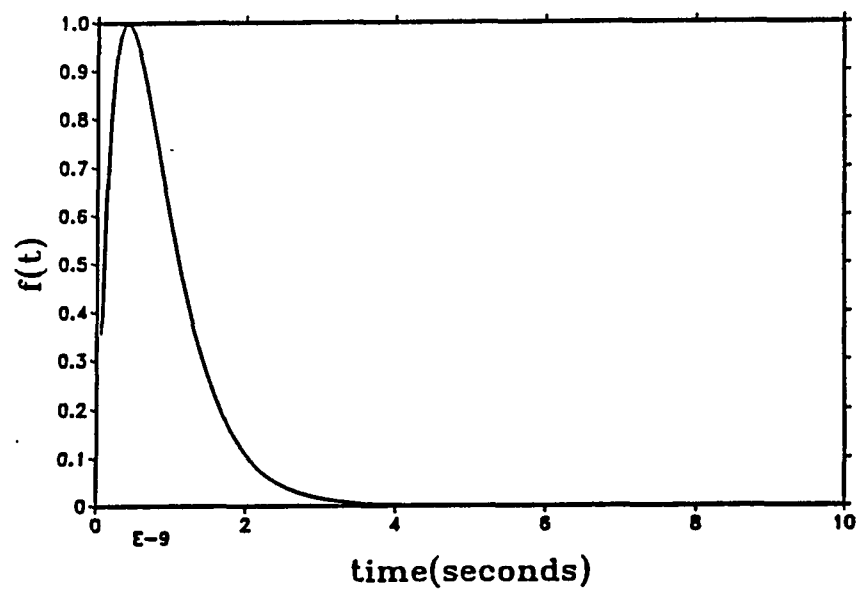
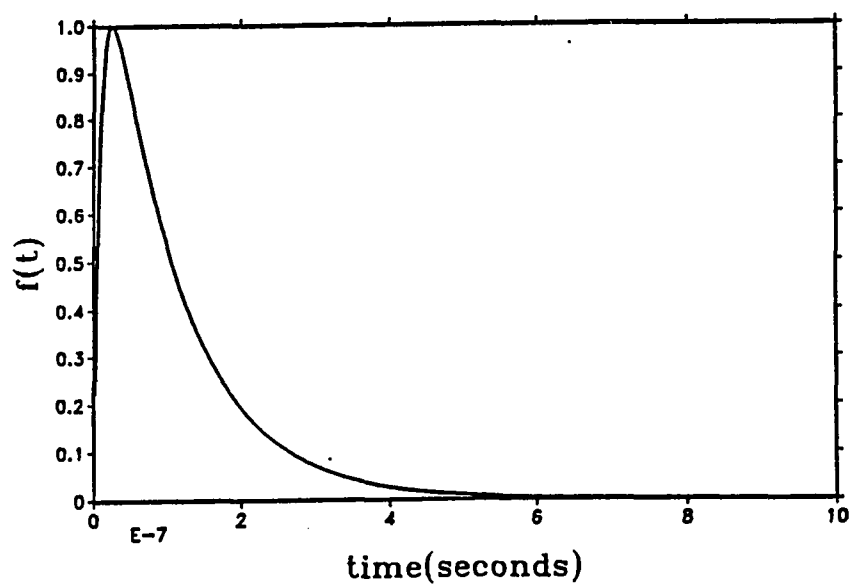


Figure 3-22 Plot of the time domain solution for the low and high frequency pulse with their frequency spectrums truncated at 255 Mhz and 8 Ghz, respectively.

3.5.2 Transient Current Response

Now that we have the frequency spectrum for the transient pulse, we need to also compute the frequency spectrum for the current. Since the frequency spectrum of the pulse is truncated at a certain frequency, it is only necessary to calculate the current up to that frequency. Using the expression for the current given in (3-31), we compute the current at four places on the wire for the low frequency pulse and at three places on the wire for the high frequency pulse. Three aperture sizes are considered for both cases. To obtain our time domain solution, we must divide the frequency spectrum into a number of equally spaced intervals. The IFFT routine requires that the frequency points which demarcate the intervals must be a power of two. For the low frequency pulse, we consider frequencies ranging from DC to 255 MHz using 255 frequency intervals.

The resulting time domain response to the low frequency pulse is shown in Figures 3-23 through 3-25. The four curves on each plots represent observation points from $z = 0.1$ m to $z = 100$ m. The time dependence has been adjusted such that the point $t = 0$ corresponds to the incident pulse being at the aperture ($z = 0$). It is interesting to note that the size of the aperture has almost no effect on the pulse. This is due to the quasi-*TEM* behavior of the current at low frequencies. In the previous section the frequency domain results show the current decaying very slowly as it propagates down the wire. The time domain plots bear this out. Even at a distance of 100 meters from the aperture, the pulse amplitude is still at 80% of its initial value. Another possible effect of the screen is to distort the shape of the incoming transient pulse. For the case of the low frequency pulse, the distortion is

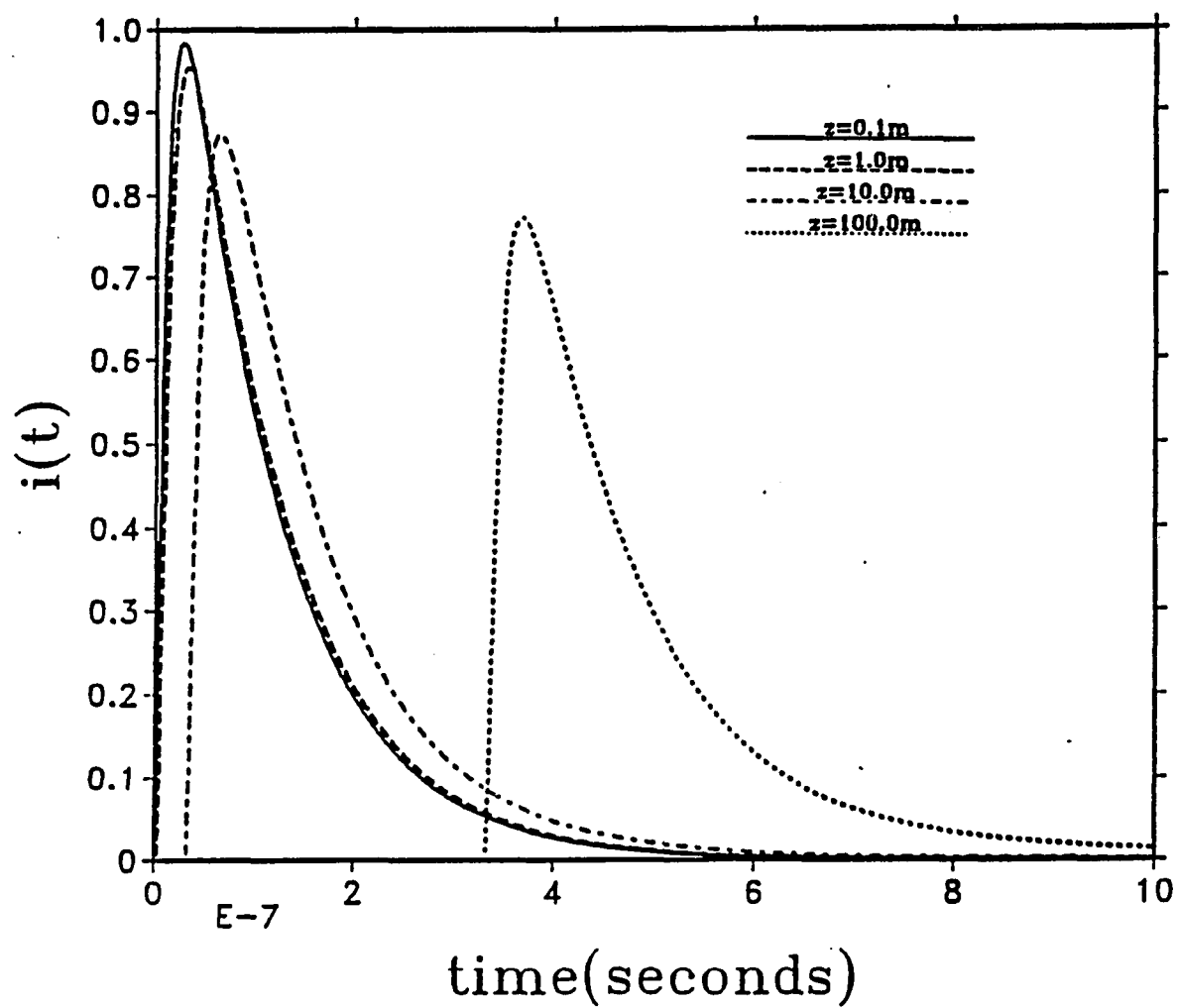


Figure 3-23 Time domain results due to the low frequency pulse with $b/a = 1.01$.

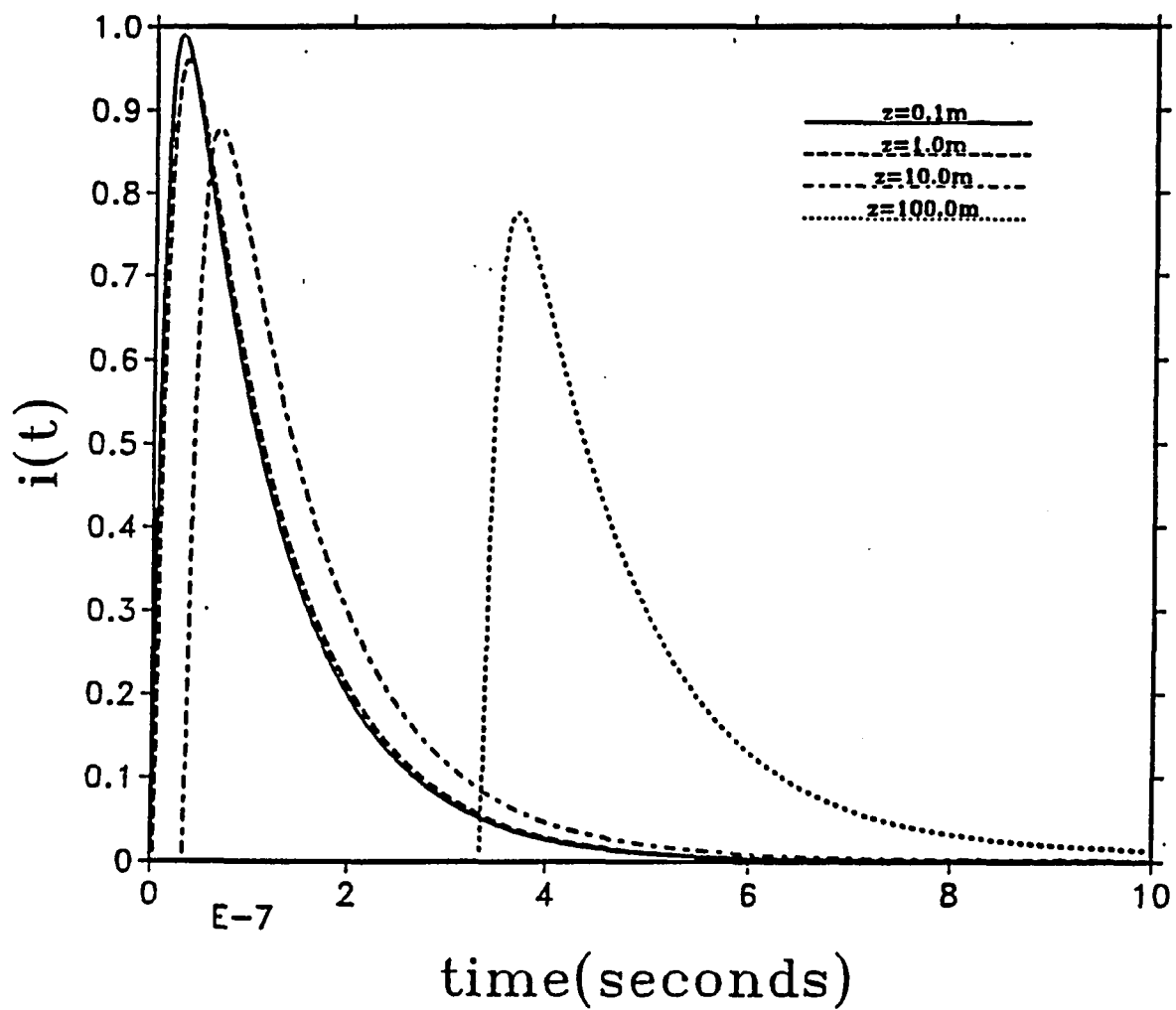


Figure 3-24 Time domain results due to the low frequency pulse with $b/a = 2$.

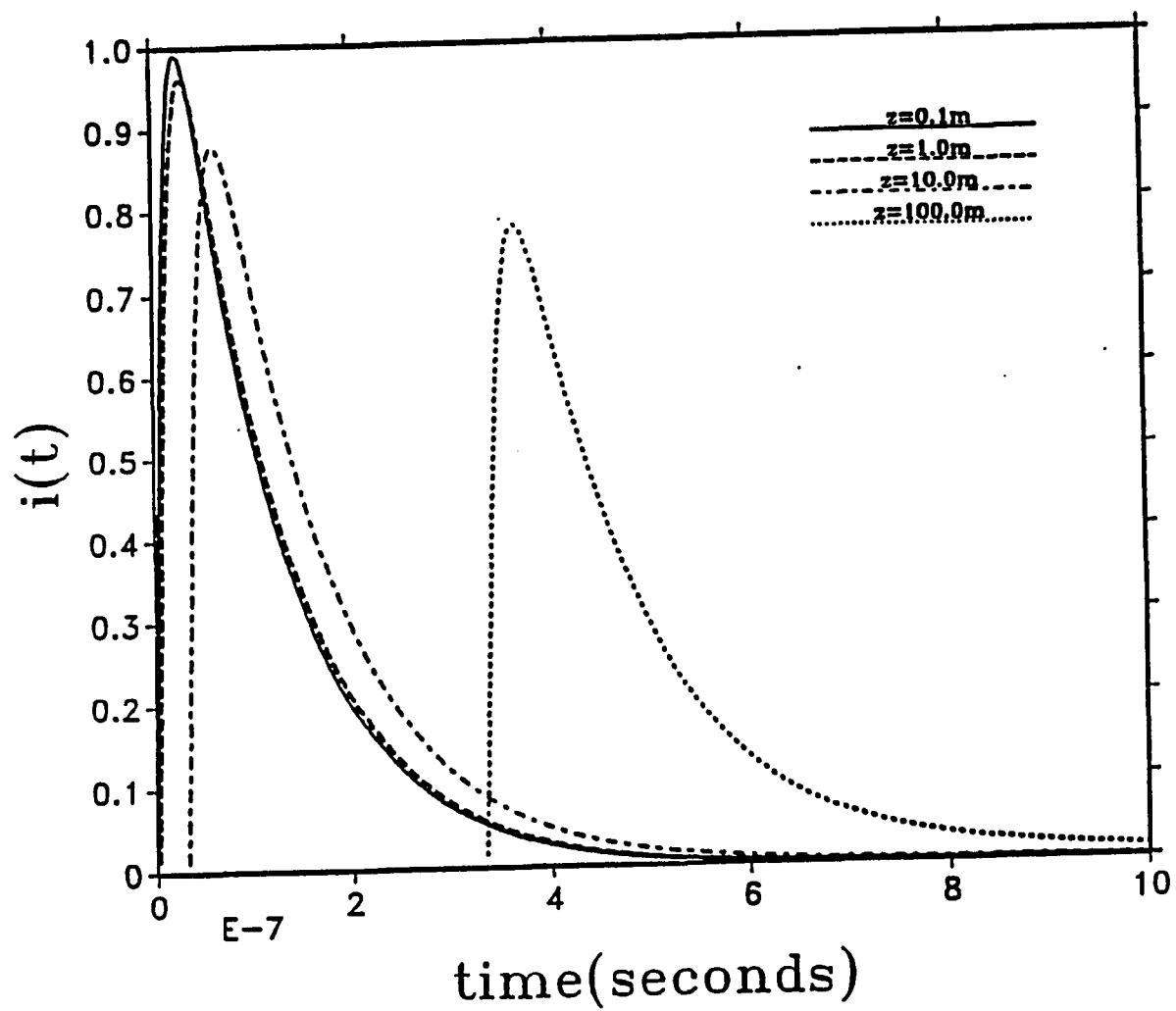


Figure 3-25 Time domain results due to the low frequency pulse with $b/a = 5$.

negligible. There is no noticeable change in either the rise or fall times for any of the curves.

For the high frequency pulse, we consider frequencies ranging from DC to 8 GHz for 255 frequency intervals. The inclusion of the higher frequencies means that current attenuation associated with it should cause a significant decay in the input pulse amplitude. The time domain solutions (Figures 3-26 through 3-28) show this to be true. As the current propagates down the wire, there is a much greater drop-off in the amplitude of the pulse as compared to the low frequency case. Since same numerical problems which occur in (3-18) are present here, we are limited in the size of kz which we can handle. We must therefore consider observation points which are closer to the aperture than in the low frequency case. These point are located at $z = 0.01, 0.1$, and 1.0 meters. We also see that the aperture size has a substantial effect on the amount of current which is attenuated. For example, the peak amplitude of the current just 1 cm from the aperture is only 70% of its initial value for $b/a = 1.01$, whereas it is still 95% of its initial value for $b/a = 5.0$.

Unlike the low frequency case the screen causes a distortion of the transient pulse. This is expected since the high frequency content in the pulse is attenuated at a different rate than the low frequency content. The rise and fall times of the pulse is dependent upon the size of the aperture. As the aperture gets smaller the pulse shape begins spreading out. Table 3-1 provides values of the rise and fall times at various positions on the wire for aperture sizes of $b/a = 1.01$ and 5.0 .

If we examine Figure (3-28), we see that there are tiny ripples on the trailing end on each of the curves. These tiny ripples are caused by the truncation of the input pulse frequency spectrum at $f = 8$ GHz. We can smooth the curves by

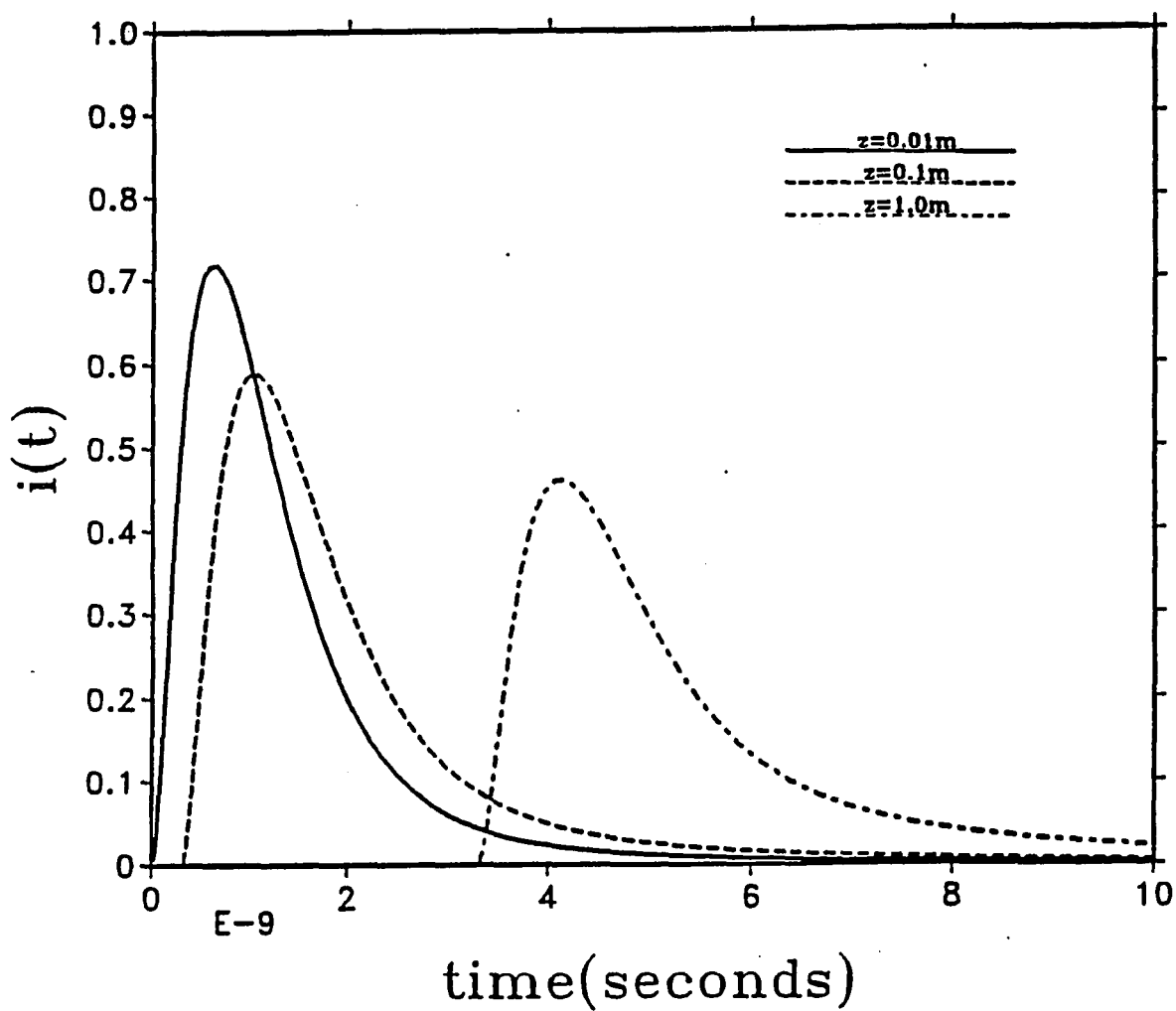


Figure 3-26 Time domain results due to the high frequency pulse with $b/a = 1.01$.

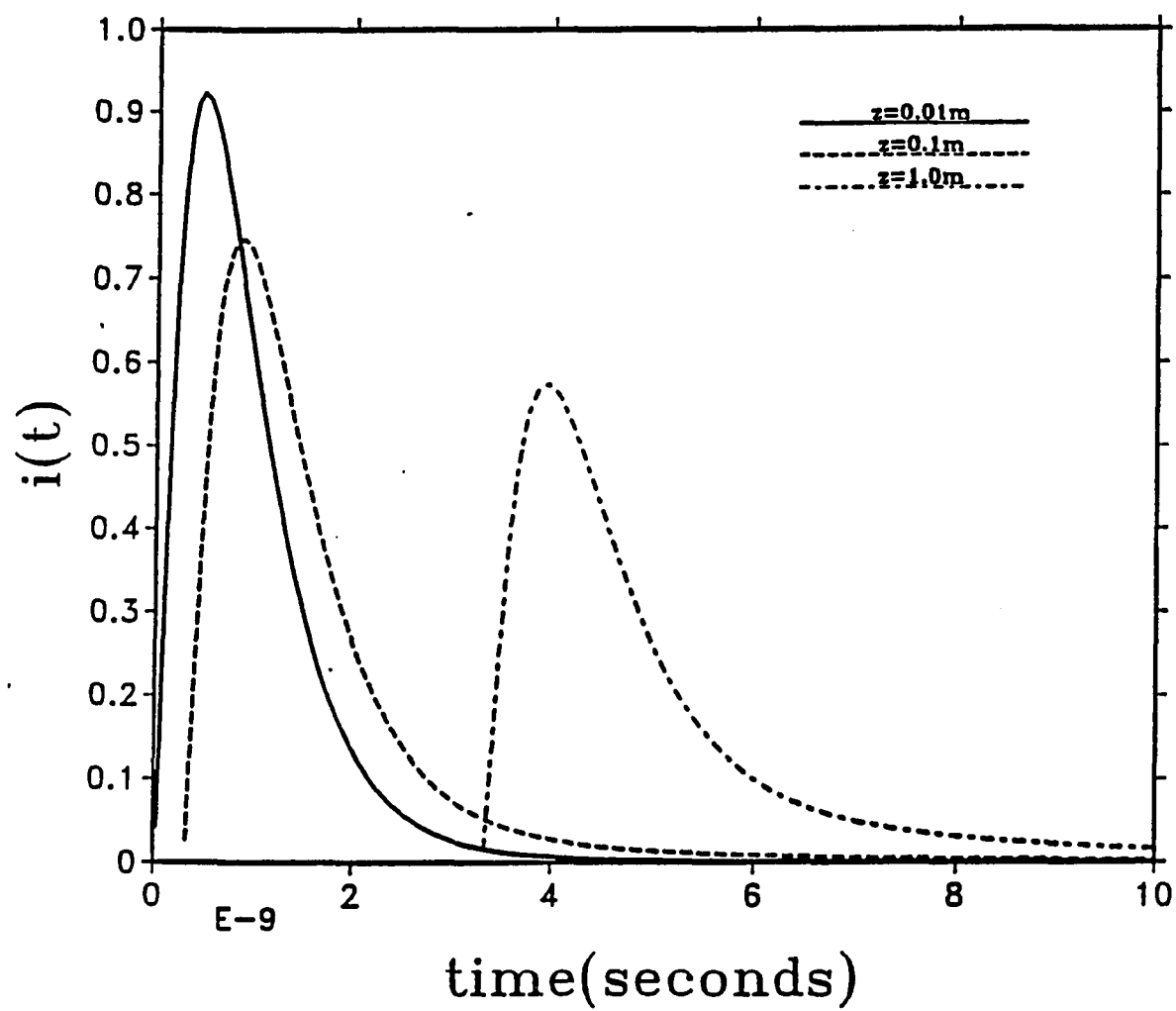


Figure 3-27 Time domain results due to the high frequency pulse with $b/a = 2$.

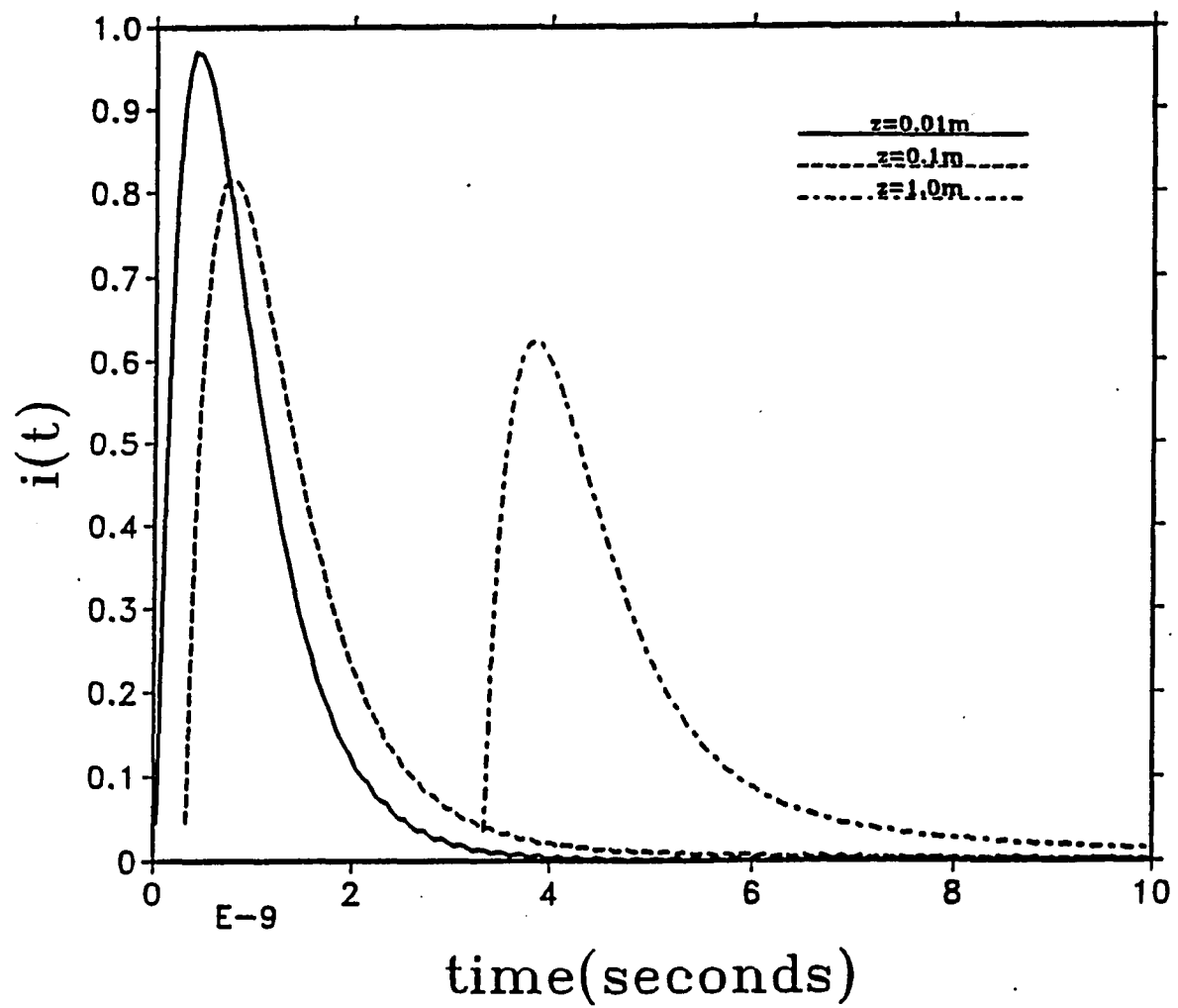


Figure 3-28 Time domain results due to the high frequency pulse with $b/a = 5$.

Table 3-1 Rise and fall times of transient pulse as a function of aperture size and position on the wire for the high frequency pulse.

	Rise Time(ns)		Falltime(ns)	
z(m)	b/a=1.01	b/a=5.0	b/a=1.01	b/a=5.0
0.0	0.233	0.233	1.42	1.42
0.01	0.364	0.239	1.92	1.475
0.1	0.400	0.267	2.26	1.74
1.0	0.437	0.293	3.32	2.16

truncating the curves further out in frequency, but this requires more computation time. For our interests it is adequate to recognize this aberration and realize its cause.

CHAPTER 4

ELECTRIC FIELD

In many situations a good understanding of the field pattern within a region of interest is essential to the understanding of the overall problem. Hence, we devote this chapter to obtaining contours for the electric field. We begin by formulating expressions for the two existing components of the electric field, E_ρ and E_z . The solution of the integrals in these expressions requires a significant amount of numerical computation. We next consider the far field case where we look at the field distribution far from the aperture in both z and ρ . This allows us to evaluate the integrals analytically. Consequently, we can obtain contour plots using both the original electric field expressions and the far-field approximation.

4.1 Formulation of Electric Field Equations

In the previous chapter we were able to compute a solution for the aperture field by MOM. We now use this result in (2-16) to get the following expression for the magnetic field in Region 2:

$$H_{\phi 2} = -\frac{k}{\eta} \sum_{j=1}^N \alpha_j \int_0^\infty \frac{B(k\rho\gamma)[A(kU_j\gamma) - A(kV_j\gamma)]}{(1-\gamma^2)^{\frac{1}{2}} H_0^{(1)}(ka\gamma) H_0^{(2)}(ka\gamma)} e^{-ikz(1-\gamma^2)^{\frac{1}{2}}} d\gamma \quad (4-1)$$

We formulate expressions for the electric field in terms of (4-1) by using (2-3) and (2-4). Interchanging the derivatives and integrals, we obtain

$$E_\rho(\rho, z) = -k \sum_{j=1}^N \alpha_j \int_0^\infty \frac{B(k\rho\gamma)[A(kU_j\gamma) - A(kV_j\gamma)]}{H_0^{(1)}(ka\gamma) H_0^{(2)}(ka\gamma)} e^{-ikz(1-\gamma^2)^{\frac{1}{2}}} d\gamma \quad (4-2)$$

$$E_z(\rho, z) = ik \sum_{j=1}^N \alpha_j \int_0^\infty \frac{A(k\rho\gamma)[A(kU_j\gamma) - A(kV_j\gamma)]}{(1-\gamma^2)^{\frac{1}{2}} H_0^{(1)}(ka\gamma) H_0^{(2)}(ka\gamma)} e^{-ikz(1-\gamma^2)^{\frac{1}{2}}} \gamma d\gamma (4-3)$$

The electric field, like the current, cannot be evaluated analytically. We must therefore use the techniques from Appendix B to put (4-2) and (4-3) into a form which permits easy numerical computations. The modified expressions for the electric field are written as

$$\begin{aligned} E_\rho = & -k \sum_{j=1}^N \alpha_j \left\{ \int_0^\delta \left\{ \frac{B(k\rho\gamma)[A(kU_j\gamma) - A(kV_j\gamma)]}{H_0^{(1)}(ka\gamma) H_0^{(2)}(ka\gamma)} e^{-ikz(1-\gamma^2)^{\frac{1}{2}}} \right. \right. \\ & + \frac{\ln(\frac{U_j}{V_j}) e^{-ikz}}{k\rho\gamma[\frac{\pi^2}{4} + (\ln(\frac{ka\gamma}{2}) + \Gamma)^2]} \Big\} d\gamma \\ & - \frac{\ln(\frac{U_j}{V_j})}{k\rho} \left\{ 1 + \frac{2}{\pi} \arctan \left[\frac{2}{\pi} (\ln(\frac{ka}{2}) + \Gamma) \right] \right\} e^{-ikz} \\ & + \int_1^\infty \left\{ \frac{B(k\rho\gamma)[A(kU_j\gamma) - A(kV_j\gamma)]}{H_0^{(1)}(ka\gamma) H_0^{(2)}(ka\gamma)} e^{-ikz(1-\gamma^2)^{\frac{1}{2}}} \right. \\ & + \frac{2 \cos k\gamma(\rho - a)}{\pi\gamma\sqrt{k\rho}} \left[\frac{\sin k\gamma(U_j - a)}{\sqrt{kU_j}} - \frac{\sin k\gamma(V_j - a)}{\sqrt{kV_j}} \right] e^{-kz\gamma} \Big\} d\gamma + \frac{1}{2\pi\sqrt{k\rho}} \Phi_3 \Big\} \\ & + \int_{\arcsin(\delta)}^{\frac{\pi}{2}} \frac{B(k\rho \sin \theta)[A(kU_j \sin \theta) - A(kV_j \sin \theta)]}{H_0^{(1)}(ka \sin \theta) H_0^{(2)}(ka \sin \theta)} e^{-ikz \cos \theta} \cos \theta d\theta \quad (4-4) \end{aligned}$$

where

$$\begin{aligned}\Phi_3 = & \frac{1}{\sqrt{kU_j}} \left[E_1(kz - ik(U_j - \rho)) - E_1(kz + ik(U_j - \rho)) \right. \\ & + E_1(kz - ik(U_j + \rho - 2a)) - E_1(kz + ik(U_j + \rho - 2a)) \left. \right] \\ & - \frac{1}{\sqrt{kV_j}} \left[E_1(kz - ik(V_j - \rho)) - E_1(kz + ik(V_j - \rho)) \right. \\ & + E_1(kz - ik(V_j + \rho - 2a)) - E_1(kz + ik(V_j + \rho - 2a)) \left. \right]\end{aligned}$$

and

$$\begin{aligned}E_z = & ik \sum_{j=1}^N \alpha_j \left\{ \int_0^{\frac{\pi}{2}} \frac{A(k\rho \sin \theta) [A(kU_j \sin \theta) - A(kV_j \sin \theta)]}{H_0^{(1)}(ka \sin \theta) H_0^{(2)}(ka \sin \theta)} e^{-ikz \cos \theta} \sin \theta d\theta \right. \\ & + i \int_2^\infty \left\{ \frac{A(k\rho \gamma) [A(kU_j \gamma) - A(kV_j \gamma)]}{(\gamma^2 - 1)^{\frac{1}{2}} H_0^{(1)}(ka \gamma) H_0^{(2)}(ka \gamma)} e^{-kz(\gamma^2 - 1)^{\frac{1}{2}}} \gamma \right. \\ & - \frac{2 \sin k\gamma(\rho - a)}{\pi \gamma \sqrt{k\rho}} \left[\frac{\sin k\gamma(U_j - a)}{\sqrt{kU_j}} - \frac{\sin k\gamma(V_j - a)}{\sqrt{kV_j}} \right] e^{-kz\gamma} \left. \right\} d\gamma + \frac{i}{2\pi \sqrt{k\rho}} \Phi_4 \\ & + i \int_0^{\frac{\pi}{2}} \frac{A(k\rho \sec \theta) [A(kU_j \sec \theta) - A(kV_j \sec \theta)]}{\cos^2 \theta H_0^{(1)}(ka \sec \theta) H_0^{(2)}(ka \sec \theta)} e^{-kz \tan \theta} d\theta \left. \right\} \quad (4-5)\end{aligned}$$

where

$$\begin{aligned}\Phi_4 = & \frac{1}{\sqrt{kU_j}} \left[E_1(2kz - i2k(U_j - \rho)) + E_1(2kz + i2k(U_j - \rho)) \right. \\ & - E_1(2kz - i2k(U_j + \rho - 2a)) - E_1(2kz + i2k(U_j + \rho - 2a)) \left. \right] \\ & - \frac{1}{\sqrt{kV_j}} \left[E_1(2kz - i2k(V_j - a)) + E_1(2kz + i2k(V_j - \rho)) \right. \\ & - E_1(2kz - i2k(V_j + \rho - 2a)) - E_1(2kz + i2k(V_j + \rho - 2a)) \left. \right]\end{aligned}$$

These expressions are further complicated by the fact that both ρ and z are allowed to vary. In the evaluation of the current, numerical difficulties arise due to the oscillations in the $e^{-ikz(1-\gamma^2)^{\frac{1}{2}}}$ term. This limits the size of kz for which we compute the current. For the field expressions these oscillations are still present. In addition, there are oscillations resulting from the term $B(k\rho\gamma)$. Thus, we are numerically limited by the size of both $k\rho$ and kz .

4.2 Far-Field Approximation

Our inability to calculate the fields for large values of either kz and $k\rho$ can be relieved by the far-field approximation. In the special case where both kz and $k\rho$ are large, we can obtain approximate expressions for both E_ρ and E_z . This far-field approximation utilizes the method of stationary phase.

Consider the far field approximation for E_ρ . In order to facilitate its derivation we manipulate (4-2) into the following form:

$$E_\rho(\rho, z) = \frac{ik}{2} \sum_{j=1}^N \alpha_j \int_0^\infty \left[\frac{H_1^{(2)}(k\rho\gamma)}{H_0^{(2)}(ka\gamma)} - \frac{H_1^{(1)}(k\rho\gamma)}{H_0^{(1)}(ka\gamma)} \right] \cdot [A(kU_j\gamma) - A(kV_j\gamma)] e^{-ikz(1-\gamma^2)^{\frac{1}{2}}} d\gamma \quad (4-6)$$

Since there is a singularity in the integrand at $\gamma = 0$, we separate our integral into two parts; one where the integral goes from 0 to δ and one where it goes from δ to ∞ where δ is small. Let us first consider the integral from 0 to δ . Because δ is small, we take the small argument approximation for the integrand and evaluate

the integral to get

$$\int_0^\delta \sum_{j=1}^N \alpha_j \frac{\ln(\frac{U_j}{V_j}) e^{-ikz}}{\rho \gamma \ln^2 \gamma} d\gamma = - \sum_{j=1}^N \alpha_j \frac{\ln(\frac{U_j}{V_j})}{\rho \ln \delta} \quad (4-7)$$

For δ small, its contribution to the overall integral vanishes.

Let us now consider the integral from δ to ∞ . Since ρ is large, we approximate the relevant Hankel functions by their leading asymptotic term. A change of variable ($\gamma = \cos \theta$) leads to

$$E_\rho \simeq \frac{ik}{\sqrt{2\pi k \rho}} \sum_{j=1}^N \alpha_j \int_{-i\infty}^{\arccos \delta} \frac{\sin \theta}{\sqrt{\cos \theta}} \left[\frac{e^{-i(k\rho \cos \theta - \frac{3\pi}{4})}}{H_0^{(2)}(ka \cos \theta)} - \frac{e^{i(k\rho \cos \theta - \frac{3\pi}{4})}}{H_0^{(1)}(ka \cos \theta)} \right] \\ \cdot [A(kU_j \cos \theta) - A(kV_j \cos \theta)] e^{-ikz \sin \theta} d\theta \quad (4-7)$$

where the path of integration is shown in Figure 4-1. Note that the path of integration approached $\pi/2$ since δ is small.

We now (Figure 4-2) let

$$\rho = R \cos \psi \quad (4-8)$$

$$z = R \sin \psi \quad (4-9)$$

where $0 < \psi < \pi/2$. Substitution of (4-8) and (4-9) into (4-7) gives

$$E_\rho(R, \psi) \simeq \frac{ik}{\sqrt{2\pi k R \cos \psi}} \sum_{j=1}^N \alpha_j \int_{-i\infty}^{\arccos \delta} \frac{\sin \theta}{\sqrt{\cos \theta}} \left[\frac{e^{-i\frac{3\pi}{4}} e^{-ikR \cos(\theta-\psi)}}{H_0^{(2)}(ka \cos \theta)} - \frac{e^{i\frac{3\pi}{4}} e^{ikR \cos(\theta+\psi)}}{H_0^{(1)}(ka \cos \theta)} \right] \\ \cdot [A(kU_j \cos \theta) - A(kV_j \cos \theta)] d\theta \quad (4-10)$$

In the first term in (4-10) the point of stationary phase occurs at $\theta = \psi$. In the second term there is no point of stationary phase for the values of θ and ψ

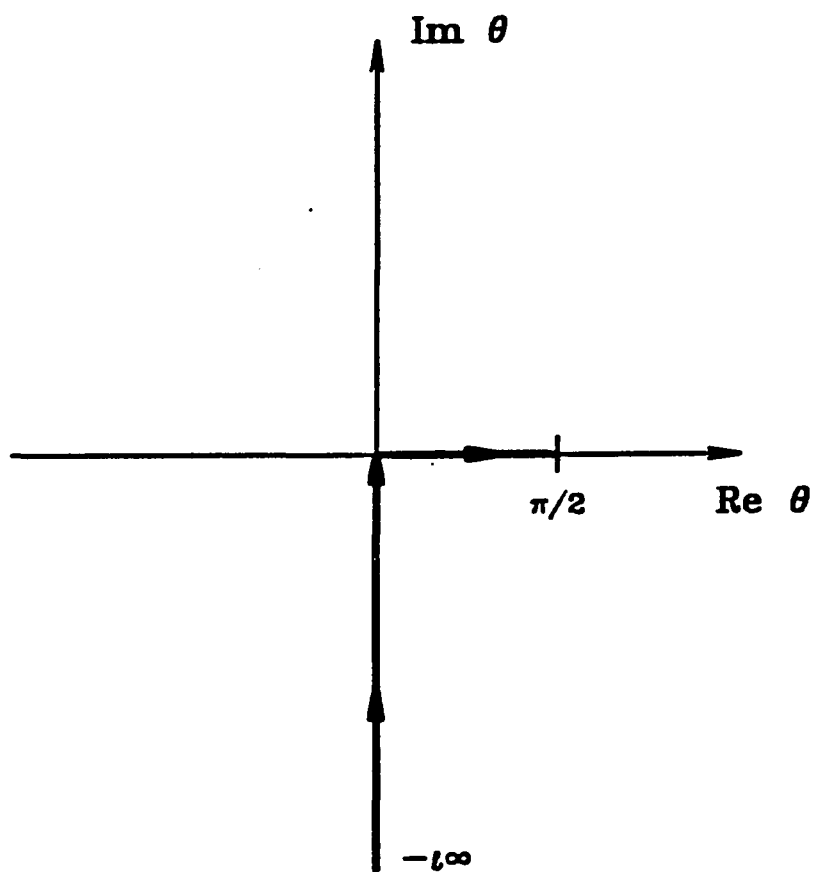


Figure 4-1 Complex integration path in the θ plane for the far field approximation.

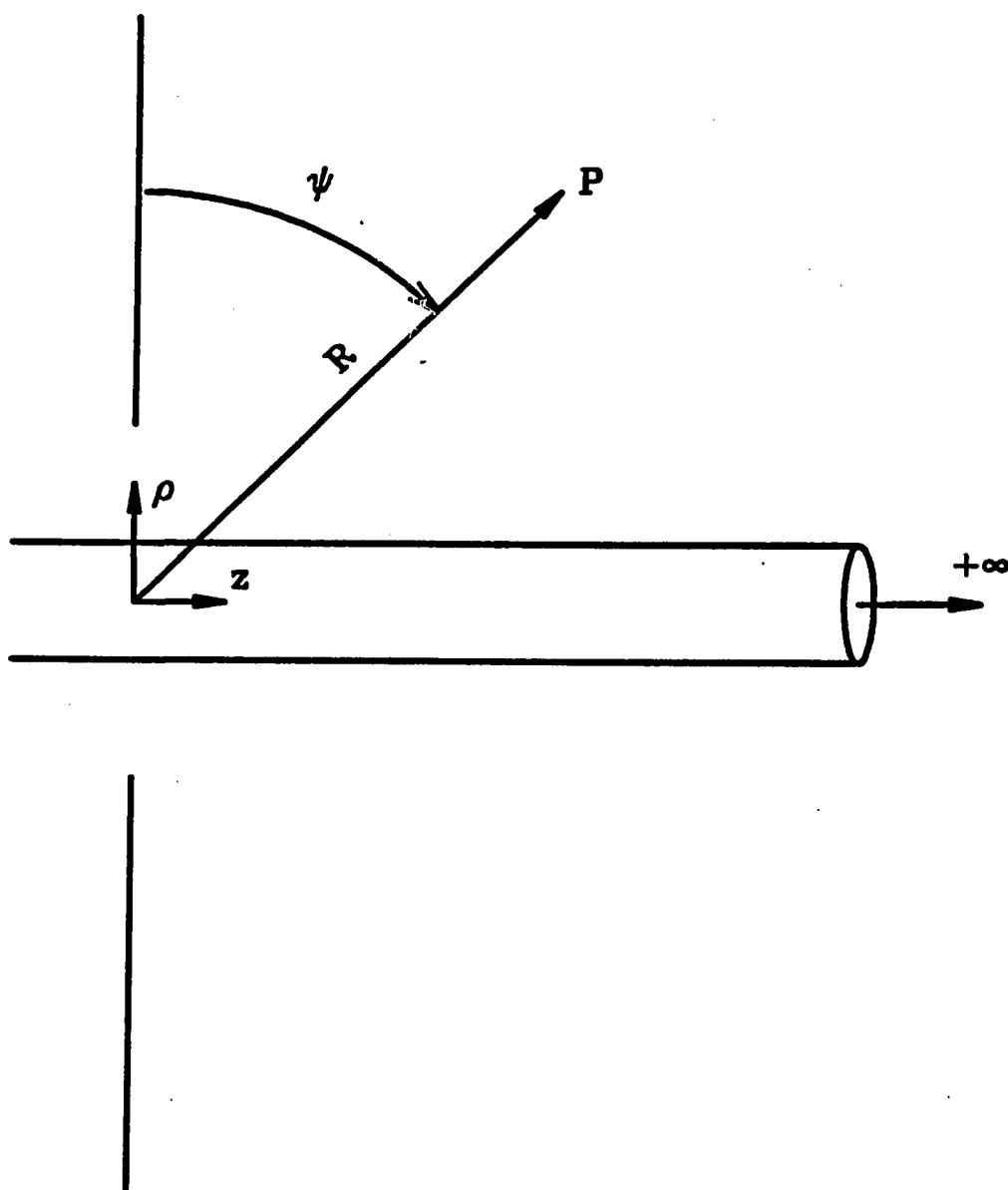


Figure 4-2 Redefined coordinate system used in the far field approximation ($\rho, z \rightarrow R, \psi$).

considered; therefore, the contribution of the second term to the overall integral is negligible compared to the first term. Also, the contribution from the interval $(-i\infty, 0)$ is negligible for R large because of the decaying exponential term which appears when θ is imaginary. Because our integral has finite limits, we must consider the contribution at the end points. The contribution at $-i\infty$ is negligible since the integrand decays exponentially at $\theta \rightarrow -i\infty$. The contribution at $\gamma = \arccos \delta$ is small because our integral does not encompass the singularity at $\pi/2$. Following Bender and Orszag (1978), we let $t = \theta - \psi$ and expand $\cos t$ around the point $t = 0$ to get $\cos t \simeq 1 - t^2/2$. As a first order approximation, we replace θ by ψ in the other terms in the integrand. The result is

$$E_\rho(R, \psi) \simeq \frac{ike^{-i\frac{3\pi}{4}} \tan \psi}{\sqrt{2\pi k R} H_0^{(2)}(ka \cos \psi)} \sum_{j=1}^N \alpha_j [A(kU_j \cos \psi) - A(kV_j \cos \psi)] \\ \cdot e^{-ikR} \int_{-\psi}^{\arccos \delta - \psi} e^{ikR \frac{t^2}{2}} dt \quad (4-11)$$

Because almost all the contribution to the remaining integral is near $t = 0$, we can extend the interval of integration to $(-\infty, \infty)$ without causing too much error as long as R is large. The resulting integral can be evaluated analytically, and the final result for E_ρ is

$$E_\rho(R, \psi) \simeq \frac{\tan \psi e^{-ikR}}{R H_0^{(2)}(ka \cos \psi)} \sum_{j=1}^N \alpha_j [A(kU_j \cos \psi) - A(kV_j \cos \psi)] \quad (4-12)$$

Following the exact steps which we used to derive E_ρ , we can obtain a similar expression for E_z which we write as

$$E_z(R, \psi) = \frac{ie^{-ikR}}{R H_0^{(2)}(ka \cos \psi)} \sum_{j=1}^N \alpha_j [A(kU_j \cos \psi) - A(kV_j \cos \psi)] \quad (4-13)$$

4.3 Results and Analysis

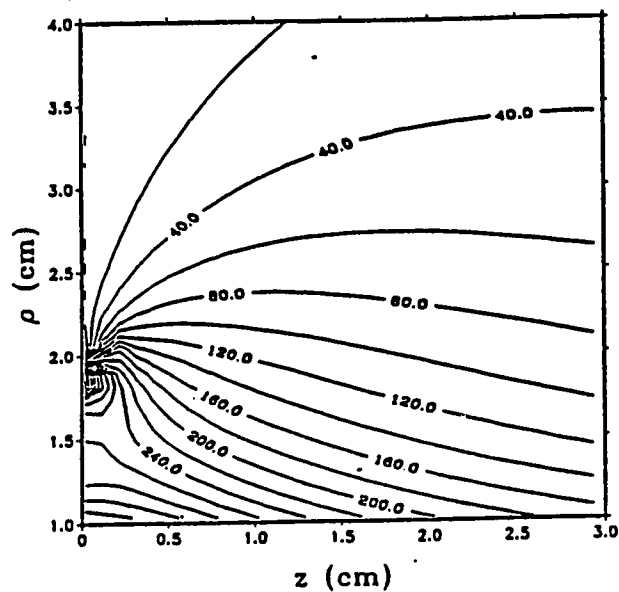
Accurate results for the electric fields close to the aperture can be computed from (4-4) and (4-5). A good means of illustrating this is by way of contour plots (Figures 4-3 and 4-4). In an attempt to avoid a profusion of plots we consider only the case where the wire radius is 1 cm and the aperture radius is 2 cm. The plots examines the square region which is delimited by the points $z = 0$ cm and 3 cm and $\rho = 1$ cm and 4 cm. The two frequencies that are considered are $f = 10$ MHz and 100 MHz.

For the region around the aperture, we are interested in the behavior of the fields at the edge of the screen and its effect upon the field pattern near it. To aid us in this discussion, let us consider a very small localized region around the edge of the screen. The region must be small enough so that the circular curvature of the aperture is small. This allows us to approximate the screen edge by a straight knife edge. A diagram of this is shown in Figure 4-5 where we have redefined the coordinate system such that the origin is located at the edge. In Figure 4-5, r is the distance from the aperture to the point of interest Q , and τ is the angle formed by the screen and Q . Since our original geometry was ϕ -symmetric, we assume that the fields do not vary along the knife edge. Jackson (1975) provides a static analysis of the edge singularity as a function of τ . His expressions for the electric field at a knife edge are

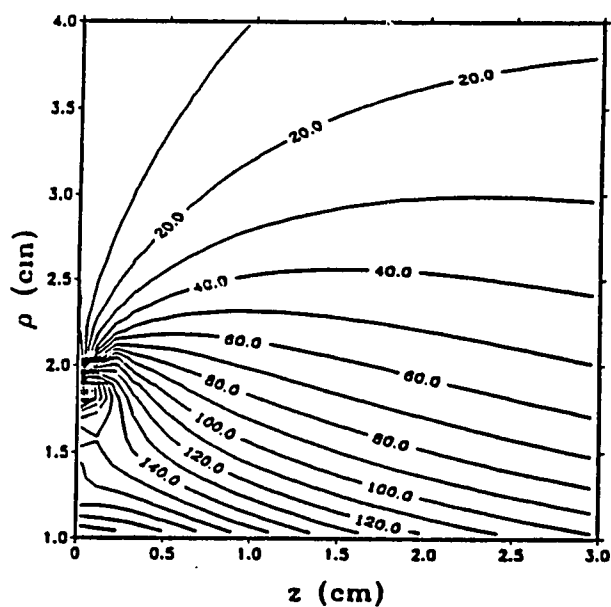
$$E_r(r, \tau) \simeq -\frac{a_1}{2r^{\frac{1}{2}}} \sin \frac{\tau}{2} \quad (4-14)$$

$$E_\tau(r, \tau) \simeq -\frac{a_1}{2r^{\frac{1}{2}}} \cos \frac{\tau}{2} \quad (4-15)$$

where $a_1 \neq 0$ is a constant.

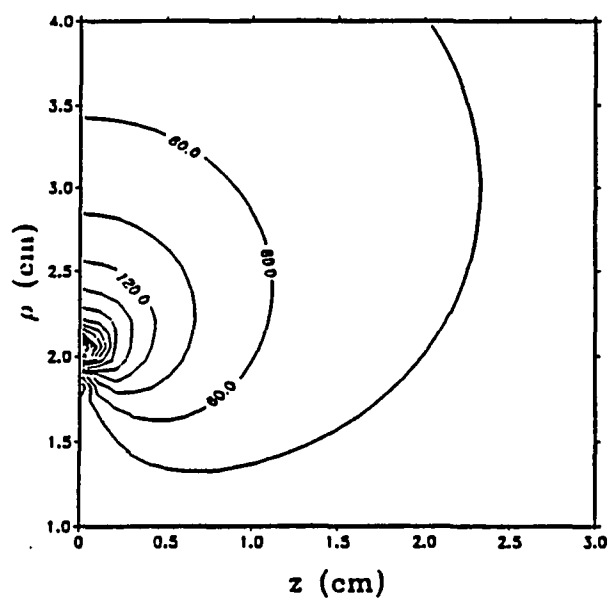


$f = 10 \text{ Mhz}$

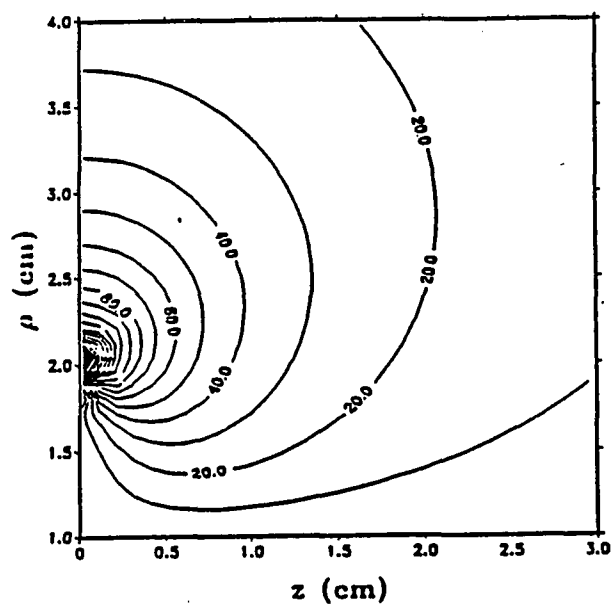


$f = 100 \text{ Mhz}$

Figure 4-3 Contour plot of $|E_\rho/I_0|$ near the aperture with $b/a = 2$, $f = 10$ and 100 Mhz.



$f = 10$ Mhz



$f = 100$ Mhz

Figure 4-4 Contour plot of $|E_z/I_0|$ near the aperture with $b/a = 2$, $f = 10$ and 100 Mhz.

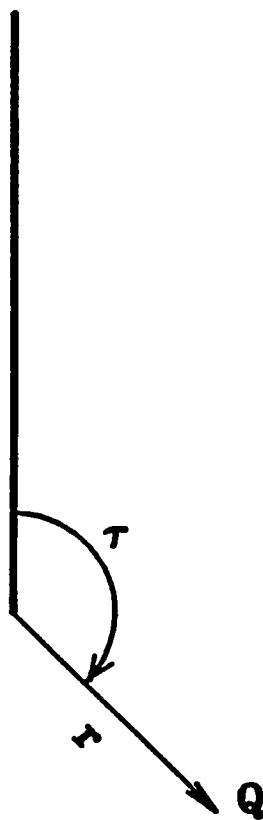


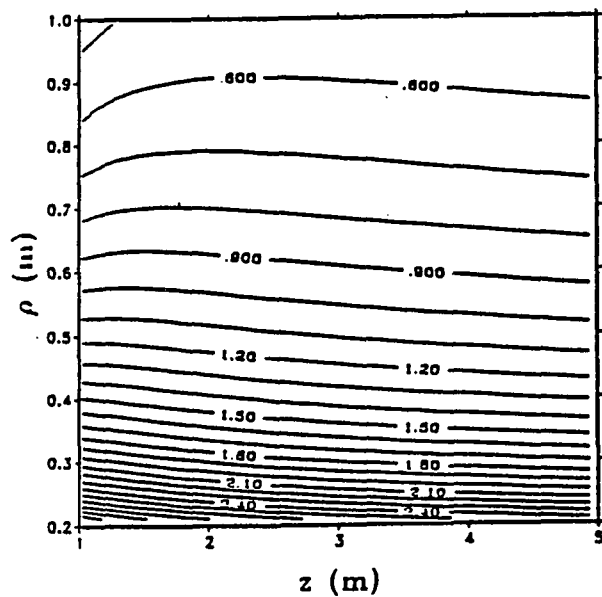
Figure 4-5 Diagram of the geometry localized to the screen edge where the coordinate system is redefined from $\rho, z \rightarrow r, \tau$.

Returning to our contour plots, we can compare our results to the static solutions, (4-14) and (4-15). Because of the different coordinate systems the components of the electric field E_ρ and E_z are in general a combination of E_r and E_τ . For $0 < \tau < \pi$, we expect the field singularity near the edge to dominate since both the $\cos(\tau/2)$ and the $\sin(\tau/2)$ are nonzero. From the contour plots we see that there is a concentration of field lines at the edge of the screen signifying the edge singularity. This corroborates our results. We need to also consider the cases where $\tau = 0$ and π . We can equate the field components in one coordinate system directly to a field components in the other system for these two cases. For the first case, we consider the situation where $\tau = \pi$. In this instance $E_\rho = -E_r$ and $E_z = -E_\tau$. Although there is no way to compare their exact values, we can compare their behavior. We consider E_ρ first. From the contour plots it is evident that the field singularity is still present in the aperture. A more careful study of these plots shows that the field values are higher in the aperture than anywhere else. This indicates that the singularity is strongest here. Likewise, the field component E_r reaches its highest value at $\tau = \pi$ because the term $\sin(\tau/2)$ is at a maximum there. For E_z we see that the field value in the aperture is very close to 0 even near the edge. This result is mimicked by the static field. Although there is an $r^{\frac{1}{2}}$ singularity in the field equation, the cosine term, which goes to 0 as $\tau \rightarrow \pi$, dominates.

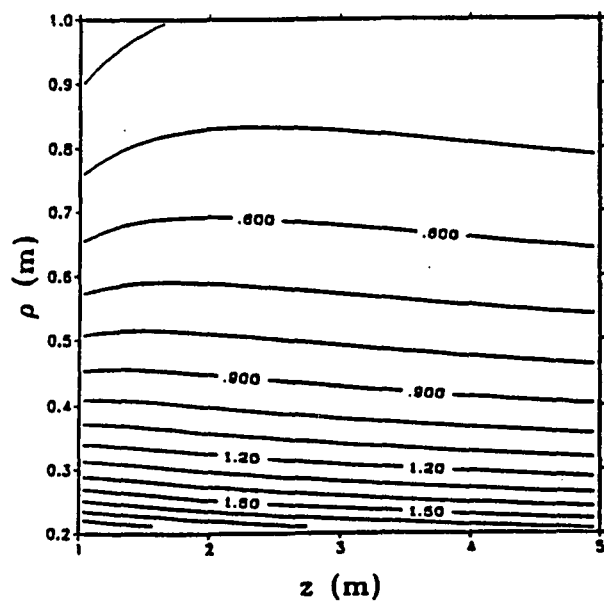
For the case where $\tau = 0$, we can equate E_ρ and E_z to E_r and E_τ , respectively. Since the tangential electric field must vanish on a perfect conductor, E_ρ must be zero on the screen. Both the contour plot and the static field results bear this out. On the other hand, there is a strong singularity present in the contour plot for E_z as we approach the edge from above. From the static field equations we notice that $\cos(\tau/2)$ is at a maximum which means that E_z is at maximum for the

static case. This further supports our numerical results for the electric field near the aperture.

Because the influence of the edge singularity is very localized, the field contours begin to take on an entirely different characteristic after only moving a small distance from the aperture. A better picture of this can be seen by looking at contour plots away from the aperture and expanding the region under consideration. Since our plots are away from the aperture, we can obtain contour plots by using the far field approximations from (4-12) and (4-13) as well as the general expressions from (4-4) and (4-5). We can then compare the plots to determine exactly how accurate the far field approximations actually are. For E_z we consider a region which is bounded by $z = 1$ m and 5 m and $\rho = 0.01$ m and 4.0 m. Since the field concentration for E_ρ is so close to the wire, we consider a region which is smaller and farther from the wire than the region for E_z so that the contour plot is more readable. The region that we choose has the same boundary as E_z in the z direction, but we only consider ρ going from 0.2 m to 1.0 m. The magnitude of the electric fields which we compute from both the general expressions and the far-field approximation are given in Figures 4-6 through 4-9. These plots are normalized by I_0 . For E_z the results are better than expected. Even for values of ρ which are fairly small, the two results are almost the same. Only when we look very close to the wire do the two results significantly diverge. This is also true for E_ρ although not to the same extent as for E_z . E_ρ is more sensitive to the errors near the wire which result from making the far field approximation. Overall, the far field approximation is accurate for large values of ρ and z while at the same time requiring only a minute fraction of the computational time needed to evaluate the general expression.

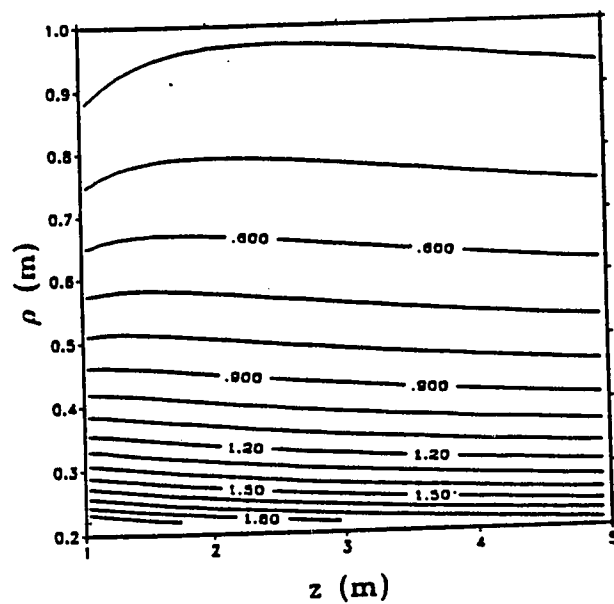


General Expression

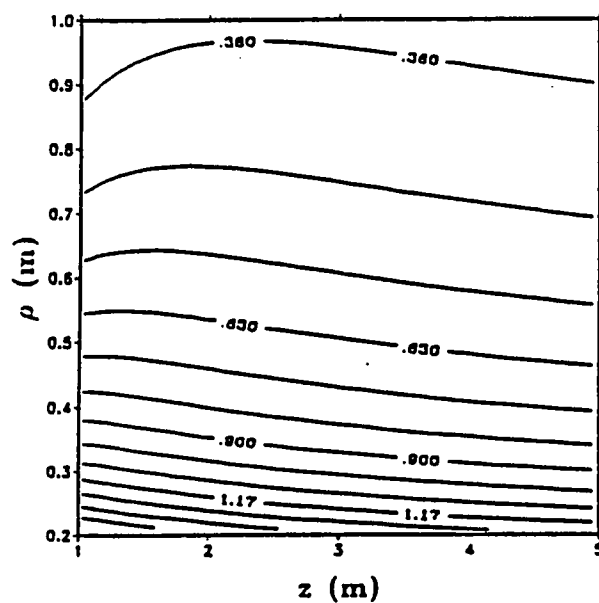


Far-field Approximation

Figure 4-6 Contour plot of $|E_\rho/I_0|$ far from the aperture with $b/a = 2$, $f = 10$ Mhz.

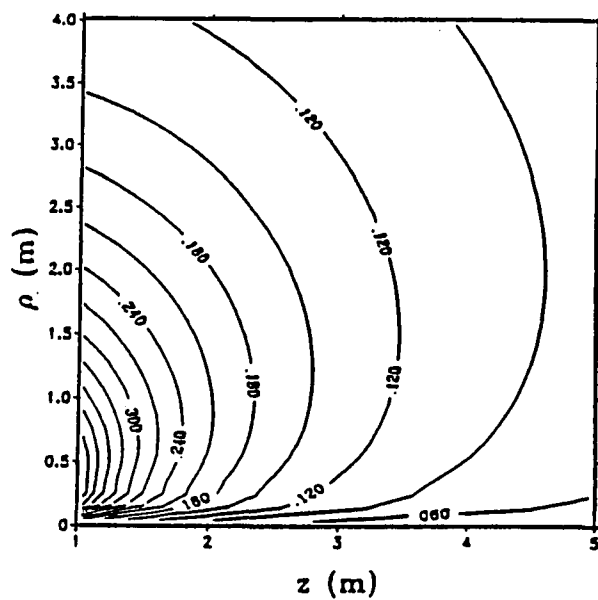


General Expression

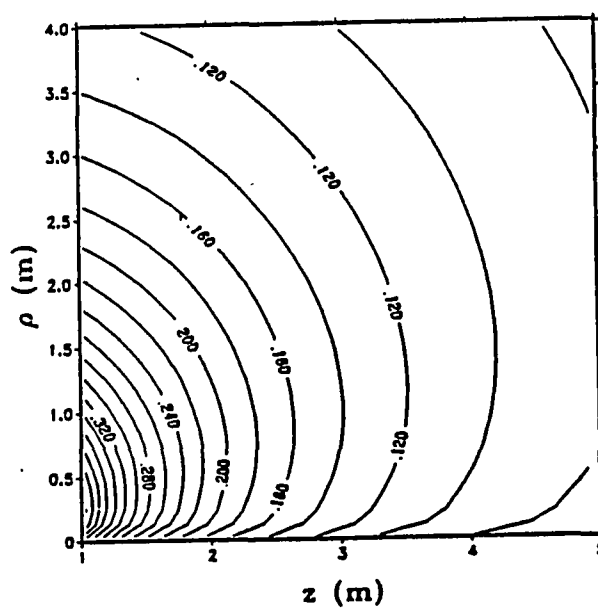


Far-field Approximation

Figure 4-7 Contour plot of $|E_\rho/I_0|$ far from the aperture with $b/a = 2$, $f = 100$ Mhz.

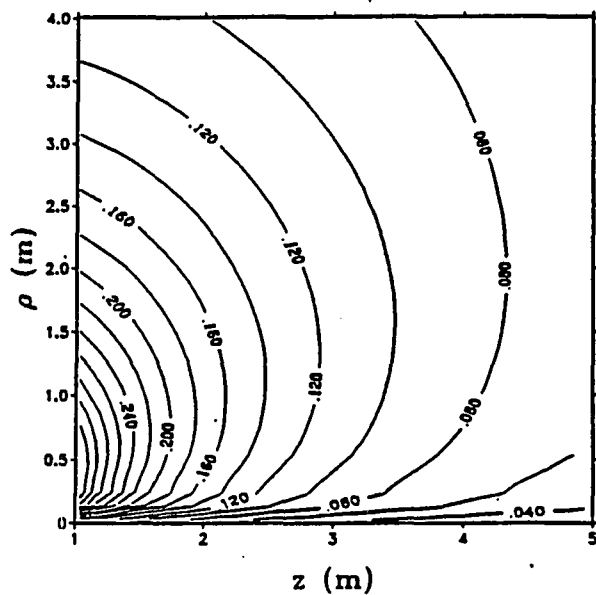


General Expression

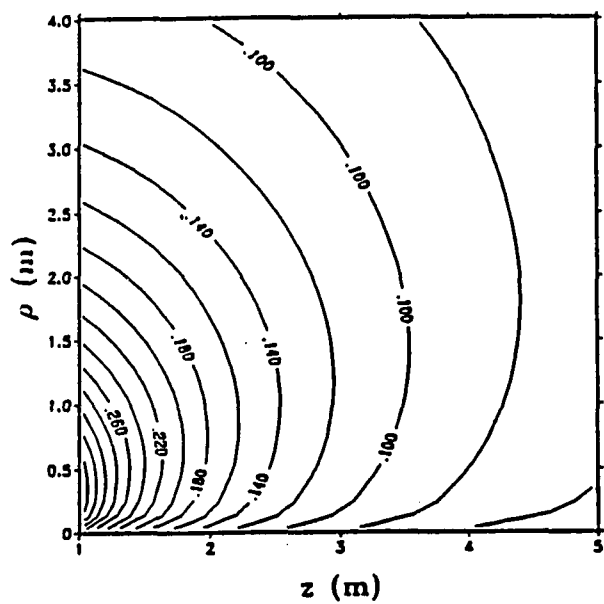


Far-field Approximation

Figure 4-8 Contour plot of $|E_x/I_0|$ far from the aperture with $b/a = 2$, $f = 10$ Mhz.



General Expression



Far-field Approximation

Figure 4-9 Contour plot of $|E_z/I_0|$ far from the aperture with $b/a = 2$, $f = 100$ Mhz.

The circular shape of the contour curves for E_z are very similar to that which is generated by a ring source. This comes as no surprise since we expect a small aperture to look like a ring source at a distance far from the aperture. The contour plots for E_ρ shows the field falling off with increasing ρ . This dropoff is proportional to $1/\rho$, which is indicative of a quasi-*TEM* behavior.

CHAPTER 5

CONCLUSIONS AND RECOMMENDATIONS

In this thesis we have provided a thorough discussion of the problem of electromagnetic penetration through an aperture with a wire passing through the aperture center. We began by formulating expressions for the fields in the situation where the source excites only the TM_z modes. Because the source in our problem is not physically realizable, we performed an analysis on an approximate source which had the same characteristics as our idealized source. We showed that the modal behavior of the approximate source is quasi- TEM and that the electric field behavior near the wire was the same as that which results from an idealized source. In addition, with the aid of the field expressions we were able to derive expressions for the admittance and the current on the wire. We then proposed an equivalent circuit model which agrees with the admittance and the current expressions. We showed that the admittance was composed of a conductance term and a susceptance term. The conductance represented radiation loss while the susceptance represented the capacitive coupling between the wire and the screen. In order to obtain numerical solutions for the circuit and field quantities, an integral equation for the electric field at the aperture was constructed. Because the integral equation was not solvable analytically, we approximated the aperture field in two different ways. The first approximation that we considered was the ZO approximation where we used only the first term in the series expansion for the field. This approximation had the advantage in that it required very little computational time to obtain a solution.

Unfortunately, the results were not accurate for an aperture radius larger than half a wavelength.

The second approximation that we made was the MOM approximation. For this case the aperture field was represented by a series of nonuniform pulse functions. A matrix equation was then formed by using delta functions as our weighting functions. This gave us more accurate results than the ZO approximation but at the expense of computation time. The need for more computation time was somewhat alleviated by the use of certain numerical techniques to speed up the evaluation of the integrals in each matrix element. Also by using nonuniform pulses as opposed to uniform ones, we were able to obtain accurate solutions with smaller matrix sizes.

The solutions from the ZO and MOM approximations allowed us to calculate solutions for both the admittance and the current. These were plotted as a function of both ka and z/a for various aperture sizes. A comparison of the solutions for the two methods showed that the ZO approximation gave accurate results for aperture sizes less than $1/10$ of a wavelength. The results were also fairly close for apertures up to a half a wavelength. The plotting parameters which we considered were chosen such that it gave a clear indication of the errors resulting from the ZO approximation for a multitude of cases. Thus, we were able to obtain a region of validity for the ZO approximation by referencing the plots. We next provided an analysis of the numerical results. It became evident from the plots that the screen was ineffective in stopping current penetration. We saw that even with very small apertures the current in Region 2 was still significant at low frequencies.

Once we had sufficiently characterized the current in the frequency domain, we proceeded to some transient analysis in the time domain. Assuming a double exponential input pulse, we looked at a case where the rise and fall times of the pulse were fast and a case where they were slow. Results were then obtained by using our frequency domain solutions and an IFFT software package. It was shown that the screen had very little effect upon the input pulse with the slower rise and fall times. This was due to the fact that the frequency content of the pulse was very low which we understood from the frequency domain plots to mean a more *TEM*-like behavior. We observed that even at a distance 100 meters from the aperture the magnitude of the current pulse was considerable. On the other hand, the input pulse with the faster rise and fall times was substantially affected by the screen because of the higher frequency content in the pulse. The current pulse lost about 60% of its initial value over a distance of 1 meter for an aperture size of $b/a = 1.01$. Also the pulse shape began to distort as it propagated down the wire resulting in slower rise and fall times.

We next solved for the electric field in order to obtain contour plots of the fields. Solutions were obtained both by a numerical evaluation of the integral in the field expressions and by a far field approximation which allowed us to write a closed form solution. We studied the singular behavior of the fields near the edge of the screen and compared them to the static solution in order to show their similarities and to be somewhat confident of our solution. We then considered a region away from the aperture so that we could determine the region of validity for the far field approximation. It was found that the far field approximation was fairly accurate as long as the field locations were not too near the wire.

Much of this work can be extended to include variations on the problem. Modifications can be made to account for any imperfections such as a wire or screen with finite conductivity. With some minor changes in the numerical code, we should be able to handle cases where we have a different source. It is also possible to consider cases where the dielectric constant of the medium is not homogeneous. For example, we could fill the aperture with either conductive or dielectric material to improve the shielding properties of the screen. Another possible extension to this work would be to improve the solution for the current. Because of the numerical difficulties associated with evaluating the current far from the aperture, it would be desirable to eventually obtain a closed form solution for the current in much the same manner as we did for the fields. Also, Wait (1988) suggests a variation in the problem whereby we place a dielectric coating on the wire. This results in a single mode being excited on the wire without the requirement of having an ideal source containing infinite energy.

Lastly, since all of the work done here has been analytical, we suggest that some experimental work be done to verify our results. A possible physical source for such an experiment is shown in Figure 2-2. Unfortunately, the aperture size of the coaxial line tends to be small to prevent higher order modes from being generated. This means that the strength of the incident field will be very small. One way to improve this would be to slowly increase the radius of the outer conductor as the coaxial line approaches the screen. Although there is some higher mode conversion, it is hoped that the expansion of the outer conductor occurs at a slow enough rate that this becomes inconsequential. By normalizing the current and fields in Region 2 to the incident current and fields in region 1, we can determine the validity of our analytical and numerical results.

APPENDIX A

DERIVATION OF SPECTRAL EXPANSION

Stakgold (1979) provides a method by which we can derive the spectral expansion associated with a specific Green's function. The Green's function that we are interested in is given by (2-20). We begin by considering the following integral in the complex λ plane for $\rho < \rho'$:

$$\oint g(\rho, \rho') d\lambda = \frac{-\pi i}{2} \oint \frac{H_1^{(2)}(\sqrt{\lambda}\rho')}{H_0^{(2)}(\sqrt{\lambda}a)} [J_1(\sqrt{\lambda}\rho)H_0^{(2)}(\sqrt{\lambda}a) - J_0(\sqrt{\lambda}a)H_1^{(2)}(\sqrt{\lambda}\rho)] d\lambda \quad (A-1)$$

After careful study of (A-1), we see that although there are no poles in the integrand, there is a branch cut in the problem. We choose the branch cut to be on the positive real axis with the contour of integration as that shown in Figure (A-1). The closed contour can be split into several line integrals which are denoted by $C1$ through $C4$, viz:

$$\int_{C1} g d\lambda + \int_{C2} g d\lambda + \int_{C3} g d\lambda + \int_{C4} g d\lambda = 0 \quad (A-2)$$

We now let r and θ go to 0 and R go to ∞ . The line integrals, $C1$ through $C4$, are then evaluated as follows:

$$\int_{C4} g d\lambda = 0 \quad (A-3)$$

$$\int_{C2} g d\lambda = -\frac{2\pi i \delta(\rho - \rho')}{\rho} \quad (A-4)$$

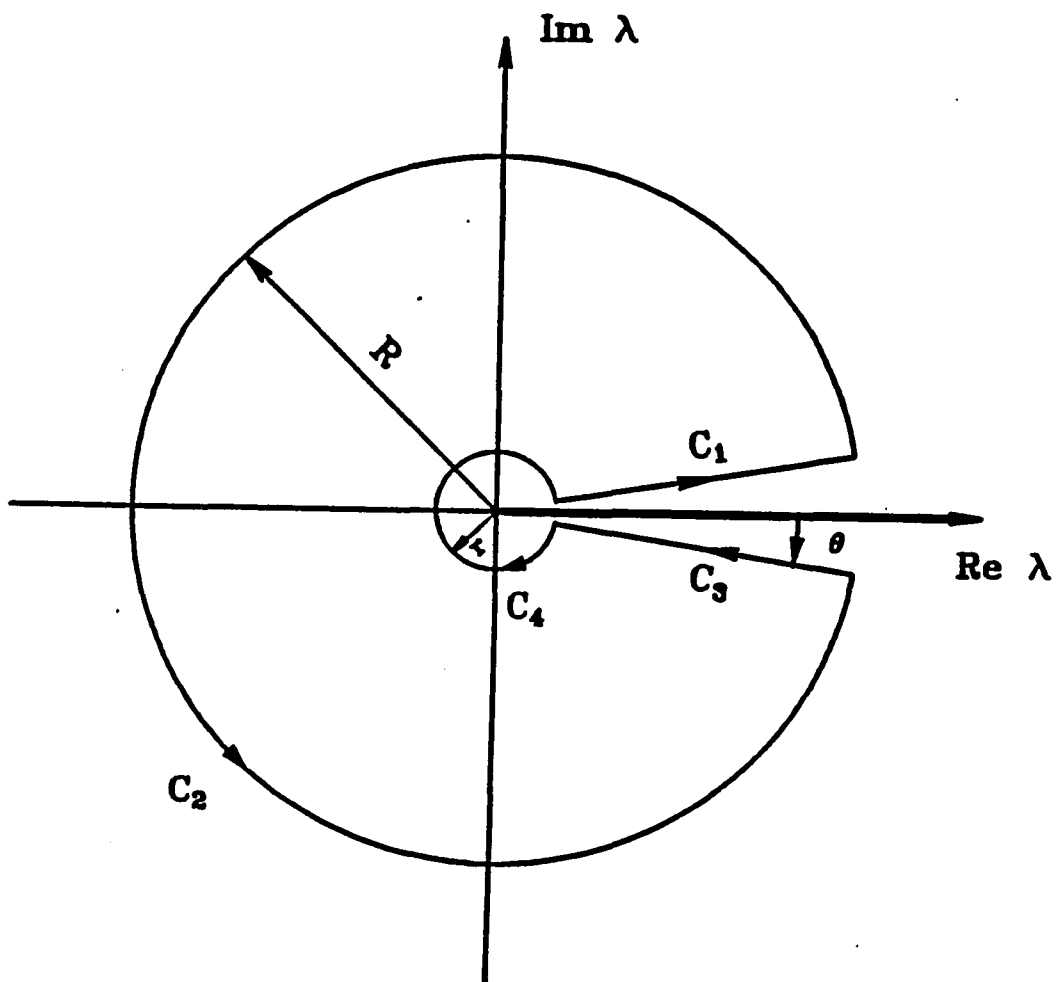


Figure A-1 Contour used in the evaluation of the spectral expansion which is needed to solve the Green's functions.

$$\int_{C_1} g d\lambda + \int_{C_3} g d\lambda = \frac{\pi i}{2} \int_0^\infty \left\{ 2J_1(M^{\frac{1}{2}}\rho)J_1(M^{\frac{1}{2}}\rho') - J_0(M^{\frac{1}{2}}a) \right. \\ \left. \cdot \left[\frac{H_1^{(2)}(M^{\frac{1}{2}}\rho)H_1^{(2)}(M^{\frac{1}{2}}\rho')}{H_0^{(2)}(M^{\frac{1}{2}}a)} + \frac{H_1^{(1)}(M^{\frac{1}{2}}\rho)H_1^{(1)}(M^{\frac{1}{2}}\rho')}{H_0^{(1)}(M^{\frac{1}{2}}a)} \right] \right\} dM (A-5)$$

After some lengthy algebraic manipulations, we can rewrite (A-5) as

$$\int_{C_1} g d\lambda + \int_{C_3} g d\lambda = \frac{\pi i}{2} \int_0^\infty \left\{ 2J_1(M^{\frac{1}{2}}\rho)J_1(M^{\frac{1}{2}}\rho') \right. \\ \left. - \left\{ J_0(M^{\frac{1}{2}}a) \left[\frac{J_1(M^{\frac{1}{2}}\rho)H_1^{(2)}(M^{\frac{1}{2}}\rho')}{H_0^{(2)}(M^{\frac{1}{2}}a)} + \frac{J_1(M^{\frac{1}{2}}\rho')H_1^{(1)}(M^{\frac{1}{2}}\rho)}{H_0^{(1)}(M^{\frac{1}{2}}a)} \right] \right. \right. \\ \left. \left. - \frac{J_0^2(M^{\frac{1}{2}}a)H_1^{(2)}(M^{\frac{1}{2}}\rho')H_1^{(1)}(M^{\frac{1}{2}}\rho)}{H_0^{(2)}(M^{\frac{1}{2}}a)H_0^{(1)}(M^{\frac{1}{2}}a)} \right\} \sum_{n=0}^\infty \frac{1}{2^n} \right\} dM \quad (A-6)$$

where the geometric series term in (A-6) is equal to 2. We then make a variable substitution of $\xi = M^{\frac{1}{2}}$ and factor (A-6) to get

$$\int_{C_1} g d\lambda + \int_{C_3} g d\lambda = 2\pi i \int_0^\infty \frac{B(\xi\rho)B(\xi\rho')}{H_0^{(1)}(\xi a)H_0^{(2)}(\xi a)} \xi d\xi \quad (A-7)$$

where $B(\xi\rho) = J_1(\xi\rho)Y_0(\xi a) - J_0(\xi a)Y_1(\xi\rho)$. If we substitute (A-3), (A-4), and (A-7) into (A-2), we obtain the following spectral expansion in ρ :

$$\frac{\delta(\rho - \rho')}{\rho} = \int_0^\infty \frac{B(\xi\rho)B(\xi\rho')}{H_0^{(1)}(\xi a)H_0^{(2)}(\xi a)} \xi d\xi \quad (A-8)$$

The spectral expansion in (A-8) allows us to formulate a special transform pair,

$$g(\rho) = \int_a^\infty g(\rho') \frac{\delta(\rho - \rho')}{\rho'} \rho' d\rho' \\ = \int_0^\infty \frac{G(\xi)B(\xi\rho)}{H_0^{(1)}(\xi a)H_0^{(2)}(\xi a)} \xi d\xi \quad (A-9)$$

and

$$G(\xi') = \int_a^\infty g(\rho') B(\xi' \rho') \rho' d\rho' \quad (A-10)$$

From this transform pair, we can obtain a spectral expansion for $\delta(\xi - \xi')/\xi$. By substituting (A-9) into (A-10) where we change $\rho \rightarrow \rho'$, we can write

$$G(\xi') = \int_0^\infty G(\xi) \int_a^\infty \frac{B(\xi \rho') B(\xi' \rho')}{H_0^{(1)}(\xi a) H_0^{(2)}(\xi a)} \rho' d\rho' \xi d\xi \quad (A-11)$$

This leads us to conclude that

$$\frac{\delta(\xi - \xi')}{\xi} = \int_a^\infty \frac{B(\xi \rho') B(\xi' \rho')}{H_0^{(1)}(\xi a) H_0^{(2)}(\xi a)} \rho' d\rho' \quad (A-12)$$

By recognizing the fact that

$$\frac{\delta(\xi - \xi')}{\xi} = \frac{\delta(\xi - \xi')}{\xi'} \quad (A-13)$$

we obtain

$$\delta(\xi - \xi') = \int_a^\infty \frac{B(\xi \rho') B(\xi' \rho')}{H_0^{(1)}(\xi a) H_0^{(2)}(\xi a)} \xi' \rho' d\rho' \quad (A-14)$$

Next, we consider the case where $\xi' = 0$. (A-14) then simplifies to

$$\delta(\xi) = \frac{2}{\pi H_0^{(1)}(\xi a) H_0^{(2)}(\xi a)} \int_a^\infty B(\xi \rho') d\rho' \quad (A-15)$$

where we are aided by the identity,

$$\lim_{\xi' \rightarrow 0} \xi' \rho' B(\xi' \rho') = \frac{2}{\pi} \quad (A-16)$$

APPENDIX B

NUMERICAL INTEGRATION TECHNIQUES

The speed of our numerical computations relies on both the hardware and software available. For hardware, we rely exclusively on the VAX 11/750 computer to perform all of our numerical tasks. It was found that single precision accuracy gave good results for our floating point calculations. The method by which we evaluate the Bessel functions in the integrals throughout the thesis is of primary importance to our overall computational efficiency. The Bessel function routines that are used in our numerical integration routines come from the SLATEC software package provided by Sandia National Laboratories. The routines have proven to be both efficient and accurate out to the precision of the computer.

There are numerous integrals throughout this thesis which must be evaluated numerically. Fortunately, the integrands in almost all of the integrals behave very similarly. We can therefore apply many of the same integration techniques to the different integrals. In order to prevent repetitive writing, an example in which we explain many of the integration techniques used in this thesis will be applied to one of the integrals. The integral on which we have chosen to demonstrate our techniques is given in (3-13). We begin by attempting to isolate the singularities in the integrand. To this end it is convenient to split the integral into four separate pieces:

$$\begin{aligned} \int_0^{\infty} K(\gamma) d\gamma &= \int_0^{\delta} K(\gamma) d\gamma + \int_{\delta}^1 K(\gamma) d\gamma + \int_1^2 K(\gamma) d\gamma + \int_2^{\infty} K(\gamma) d\gamma \\ &= I_1 + I_2 + I_3 + I_4 \end{aligned} \quad (B-1)$$

where $K(\gamma)$ is the integrand in F and δ is a number less than 1 and bounded by $\delta ka < 1$. The value of δ is chosen to allow for the best numerical convergence in I_1 . We can now consider each piece separately.

In I_1 , the singular behavior of $K(\gamma)$ at $\gamma = 0$ can be extracted and then dealt with analytically. However, great care must be taken in extracting this singularity. Initially, if we look at the small argument approximation of $K(\gamma)$, we obtain

$$K(\gamma) \approx \frac{\ln^2(\frac{b}{a})}{\gamma \ln(ka)} \quad (B-2)$$

Unfortunately, there are numerical inaccuracies in the Bessel function routines used for our calculations due to the limitations of a digital computer. These inaccuracies result in major errors in the evaluation of the integral. Thus, a more accurate small argument approximation must be found. After studying the integral, we find that the inaccuracies associated with the denominator of the integrand are the cause of the problem. A higher order approximation for the Bessel functions in the denominator gives

$$K(\gamma) \approx \frac{\ln^2(\frac{b}{a})}{\gamma [\frac{\pi^2}{4} (\ln(\frac{ka}{2}) + \Gamma)^2]} \quad (B-3)$$

Hence, the resultant integral becomes

$$I_1 = \int_0^\delta \left[\frac{A^2(kb\gamma)}{\gamma(1-\gamma^2)^{\frac{1}{2}} H_0^{(1)}(ka\gamma) H_0^{(2)}(ka\gamma)} - \frac{\ln^2(\frac{b}{a})}{\gamma [\frac{\pi^2}{4} (\ln(\frac{ka}{2}) + \Gamma)^2]} \right] d\gamma + R_1 \quad (B-4)$$

where Γ is Euler's constant and R_1 is the integral of the extracted singularity and is evaluated to be

$$R_1 = \ln^2(\frac{b}{a}) \left\{ 1 + \frac{2}{\pi} \arctan \left[\frac{2}{\pi} (\ln(\frac{ka\delta}{2}) + \Gamma) \right] \right\} \quad (B-5)$$

Standard integration techniques can now be utilized to calculate I_1 . For our case, we have chosen to use a combination of Simpson's rule and Newton's 3/8th's rule.

Real axis integration methods (Johnson and Dudley, 1985) can be used to remove the singularity at $\gamma = 1$ and allow for easy numerical evaluation of I_2 and I_3 . This involves a change of variable in both I_2 and I_3 with $\gamma = \sin \theta$ and $\gamma = \sec \theta$, respectively. This gives

$$I_2 = \int_{\arcsin(\delta)}^{\frac{\pi}{2}} \frac{A^2(kb \sin \theta)}{\sin \theta H_0^{(1)}(ka \sin \theta) H_0^{(2)}(ka \sin \theta)} d\theta \quad (B-6)$$

$$I_3 = i \int_0^{\frac{\pi}{3}} \frac{A^2(kb \sec \theta)}{H_0^{(1)}(ka \sec \theta) H_0^{(2)}(ka \sec \theta)} d\theta \quad (B-7)$$

Integrals I_2 and I_3 are now in a form where we can use standard methods to evaluate them.

Lastly, let us consider I_4 . Out of the four pieces, this integral is the most time-consuming one to evaluate. Since the interval of integration extends to infinity, we must eventually truncate the interval at a finite value. This can only be done if the integrand past a certain point contributes only a negligible amount to the total integral. Therefore, the point of truncation depends upon the rapidity at which the integrand decays to 0 as $\gamma \rightarrow \infty$. In our case, $K(\gamma)$ does not decay very quickly. We can substantially speed up this decay by characterizing the integrand's behavior as $\gamma \rightarrow \infty$ and handling it analytically. We start by obtaining an asymptotic approximation for $K(\gamma)$, which we write as

$$K(\gamma) \sim \frac{2i \sin^2 k(b-a)\gamma}{\pi kb\gamma^3} \quad (B-8)$$

Next, we subtract the approximation from the integrand to improve its rate of decay. Finally, we add the solution of the integral for the asymptotic approximation back into our equation to realize our final result,

$$I_4 = i \int_2^\infty \left\{ \frac{A^2(kb\gamma)}{(\gamma^2 - 1)^{\frac{1}{2}} \gamma H_0^{(1)}(ka\gamma) H_0^{(2)}(ka\gamma)} - \frac{2 \sin^2 k(b-a)\gamma}{\pi kb\gamma^3} \right\} d\gamma + R_2 \quad (B-9)$$

where

$$R_2 = \frac{i(k(b-a))^2}{\pi kb} \left[\frac{\sin^2 2k(b-a)}{(2k(b-a))^2} + \frac{\sin 4k(b-a)}{2k(b-a)} - 2Ci(4k(b-a)) \right] \quad (B-10)$$

The integral I_4 is also complicated by the fact that its integrand is oscillatory. This problem is handled by dividing the integrand into subintervals where the subintervals are defined by the zero crossings in the integrand. We then use our standard integration techniques on each subinterval, separately. Once the contribution of a subinterval to the overall integral falls below a certain specified threshold, the integration process stops.

REFERENCES

- Abramowitz, M. and I.A. Stegun (1972), Handbook of Mathematical Functions, Dover, New York.
- Bender, C.M. and S.A. Orszag (1978), Advanced Mathematical Methods for Scientists and Engineers, McGraw-Hill, New York, pp. 276-280.
- Bethe, H.A. (1944), "Theory of Diffraction by Small Holes," Physics Rev., 66, pp. 163-182.
- Butler, C.M. (1984), "Current Induced on a Conducting Strip Which Resides on the Planar Interface Between Two Semi-Infinite Half-Spaces," IEEE Trans. Antennas Propag., AP 32(3), pp. 226-231.
- Butler, C.M., Y. Rahmat-Samii, and R. Mittra (1978), "Electromagnetic Penetration through Apertures in Conducting Surfaces," IEEE Trans. Antennas Propag., AP 26(1), pp. 82-93.
- Casey, K.F. (1987), "Electromagnetic Characterization of Line Penetrations," JAYCOR Report for Defense Nuclear Agency, Contract No. 001-85-C-0131.
- Chen, L. (1970), "On Cavity Excitation Through Small Apertures," Interaction Note 45, Air Force Weapons Laboratory, Albuquerque, NM.
- Dudley, D.G. (1985), "Error Minimization and Convergence in Numerical Methods," Electromagnetics, 5, pp. 88-97.
- Felsen, L.B. and N. Marcuvitz (1973), Radiation and Scattering of Waves, Prentice-Hall, Englewood Cliffs, pp. 323-328.
- Harrington, R.F. (1968), Field Computation by Moment Method, Macmillan, New York, pp. 1-21.
- Jackson, J.D. (1975), Classical Electrodynamics, Wiley, New York, pp. 75-78.
- Johnson, W.A. and D.G. Dudley (1983), "Real Axis Integration of Sommerfeld Integrals: Source and Observation Points in Air," Radio Sci., 18(2), pp. 175-186.
- Lager, D. and S. Azevedo (1985), "A General-Purpose Signal Processing Program," Lawrence Livermore National Laboratory Report, UCRL-19912-Rev. 1.
- Marcuvitz, N. (1951), Waveguide Handbook, McGraw-Hill, New York, pp. 13-16.
- Meixner, J. (1972), "The Behavior of Electromagnetic Fields at Edges," IEEE Trans. Antennas Propagat., AP 20(4), pp. 442-446.

- Rahmat-Samii, Y. and Mittra, R. (1977), "Electromagnetic Coupling through Small Apertures in a Conducting Screen," IEEE Trans. Antennas Propagat., AP 25(2), pp. 180-187.
- Rayleigh, Lord (1987), "On the Incidence of Aerial and Electric Waves on Small Obstacles in the Form of Ellipsoids or Elliptic Cylinders, on the Passage of Electric Waves Through a Circular Aperture in a Conducting Screen," Phil. Mag., 44, p. 28.
- Schelkunoff, S.A. (1943), Electromagnetic Waves, Nostrand, New York, pp. 188-241.
- Stakgold, I. (1979), Green's Functions and Boundary Value Problems, Wiley, New York, pp. 411-466.
- Stratton, J.A. (1941), Electromagnetic Theory, McGraw-Hill, New York, pp. 485-486.
- Taylor, C.D., (1973), "Electromagnetic Pulse Penetration Through Small Apertures," IEEE Trans. Electromag. Comp., EMC 15(1), pp. 17-23.
- Todd, J. (1954), "Evaluation of the Exponential Integral for Large Complex Arguments," J. Research of Nat. Bureau of Standards, 52(6), pp. 313-317.
- Wait, J.R. and D.A. Hill (1979), "Theory of Transmission of Electromagnetic Waves Along a Drill Rod in Conducting Rock," IEEE Trans. Geo. Electronics, GE 17(2), pp. 21-24.
- Wait, J.R. (1985), Electromagnetic Wave Theory, Harper and Row, New York, pp. 250-254.
- Wait, J.R. (1988), personal communication.
- Williams, J.T. (1987), "Electromagnetic Scattering from and Natural Resonances of the Circular Strip," Ph.D. Dissertation, University of Arizona.
- Williamson, A.G. (1985), "Radial-line/Coaxial Line Junctions: Analysis and Equivalent Circuits," Int. J. Electronics, 58, pp. 91-104.
- Zhang, S. and D.G. Dudley (1987), "Scattering by a Radial Line Joined to a Coaxial Waveguide," J. of Electromagnetic Waves and App., 1(4), pp. 299-321.